Fakultät für Physik der Technischen Universität München
Lehrstuhl für Experimentalphysik E18

Measurement of the electron-antineutrino angular correlation coefficient a in neutron beta decay with the spectrometer aSPECT

Gerd Petzoldt

Vollständiger Abdruck der von der Fakultät für Physik der Technischen Universität München zur Erlangung des akademischen Grades eines

Doktors der Naturwissenschaften

genehmigten Dissertation.

Vorsitzender:		Univ.-Prof. Dr. A. J. Buras
Prüfer der Dissertation:	1.	Univ.-Prof. Dr. O. Zimmer
	2.	Univ.-Prof. Dr. K. Schreckenbach

Die Dissertation wurde am 29.08.2007 bei der Technischen Universität München eingereicht und duch die Fakultät für Physik am 12.09.2007 angenommen.

Contents

1 Introduction

As its name implies, particle physics focuses on the study of elementary particles and their interactions and in particular on the structure and strength of those interactions. The Standard Model of particle physics classifies the known elementary particles into two major groups consisting of three families each and it describes three of the four known fundamental forces: The electromagnetic, the strong, and the weak interaction (see table 1.1).

Particle type	Generation			Takes part in interaction		
	First	Second	Third	Electromagnetic	Strong	Weak
Leptons	e	μ	τ	yes	no	yes
	ν_e	ν_μ	ν_τ	no	no	yes
Quarks	u	c	t	yes	yes	yes
	d	s	b	yes	yes	yes

Table 1.1: Fundamental forces and particles

All of the fundamental forces are mediated by the exchange of gauge bosons. The electromagnetic interaction is mediated by photons and experienced by all charged particles. It is the force that is most apparent in every-day life apart from gravity. The strong interaction is mediated by gluons and experienced by both quarks and gluons. In turn, all composite particles containing quarks are also subject to the strong interaction. The most prominent effect of the strong interaction is consequently the existence of atomic nuclei and their structure.

The mediators of the weak interaction are the Z and $W^\pm$ bosons, and it is more universal than the strong interaction, since both leptons and quarks

are affected by it. Its most obvious effect is that of nuclear β decay. It is the only interaction that is capable of changing the flavour of a particle.

Of the four fundamental forces, the weak interaction is the second weakest and second most universal force, in both cases after gravity. In contrast to the other interactions, there are no known bound states of the weak interaction. Table 1.2 shows the strengths and ranges of the four fundamental forces.

Interaction	Strength	Range
Strong (quark level)	$\alpha_s \approx 1$	confined
Strong (nuclear)	$\frac{g_\pi^2}{4\pi} \approx 14$	$\approx m_\pi^{-1} \approx 1.5\,\mathrm{fm}$
Electromagnetic	$\alpha = 1/137.036$	∞
Weak	$G_F = 1.16639 \cdot 10^{-5}\ \mathrm{GeV}^{-2}$	$\approx M_\mathrm{W}^{-1} \approx 10^{-3}\,\mathrm{fm}$
Gravity	$G_N = M_\mathrm{Pl}^{-2} = 9.786 \cdot 10^{-20}\ \mathrm{GeV}^{-2}$	∞

Table 1.2: Fundamental forces and their strengths

Precision measurements of Standard Model parameters are of great interest due to the importance that they have not only in particle physics, but also in other fields such as cosmology. For the weak interaction, the detailed study of decay processes is the best source of information, and in particular, the decay of the free neutron

$$n \to p + e^- + \bar{\nu}_\mathrm{e} \tag{1.1}$$

is of great interest as it is free of any modification by nuclear (and hence strong) effects. In addition, there is a large number of observables present in this process which can be used to determine the same parameters in a number of different ways.

In addition to the lifetime of the neutron, these observables include the momenta and energies of the decay products as well as the angular correlations between the particles' momenta and their spins. The differential decay rate for the process containing the angular correlations can be ex-

pressed as (see section 2.1.4)

$$dW(\mathbf{p}_\mathrm{e}\mathbf{p}_{\overline{\nu}}) \propto 1 + b\frac{m_\mathrm{e}}{E_\mathrm{e}} + a\frac{\mathbf{p}_\mathrm{e}\cdot\mathbf{p}_{\overline{\nu}}}{E_\mathrm{e}E_{\overline{\nu}}} + \frac{\mathbf{P}_\mathrm{n}}{P_\mathrm{n}}\cdot\left(A\frac{\mathbf{p}_\mathrm{e}}{E_\mathrm{e}} + B\frac{\mathbf{p}_{\overline{\nu}}}{E_{\overline{\nu}}} + D\frac{\mathbf{p}_\mathrm{e}\times\mathbf{p}_{\overline{\nu}}}{E_\mathrm{e}E_{\overline{\nu}}} + \ldots\right) \tag{1.2}$$

where m_e is the mass of the electron, E_e, E_ν are the energies of electron and neutrino respectively, and $\mathbf{p}_\mathrm{e}$ and $\mathbf{p}_{\overline{\nu}}$ their momenta, while $\mathbf{P}_\mathrm{n}$ is the polarization vector of the neutron.

The coefficients a and A, which describe the angular correlations between the momenta of the electron and the anti-neutrino, and between the polarization of the neutron and the electron's momentum respectively, depend on λ, the ratio of the the weak axialvector and vector coupling constants in the Standard Model, as follows:

$$a = \frac{1-|\lambda|^2}{1+3|\lambda|^2}, \tag{1.3}$$

$$A = -2\frac{|\lambda|^2 + \mathrm{Re}(\lambda)}{1+3|\lambda|^2}. \tag{1.4}$$

Together with a second parameter, e.g. the life time of the neutron τ_n, it is possible to determine both free parameters of the free neutron decay, λ and the upper left element of the CKM matrix V_ud. The most precisely known coefficient is at this time the beta asymmetry A [Abe02]. The spectrometer *a*SPECT was designed to achieve a similar precision for the electron-antineutrino correlation coefficient a by measuring the integral proton recoil spectrum to provide an independent check of the value of λ [Zim00].

It has been shown [Nac68] that the proton recoil spectrum from neutron decay w_p can be written as

$$w_p(T) \propto g_1(T) + a g_2(T) \tag{1.5}$$

where T is the kinetic energy of the proton and $g_1(T)$ and $g_2(T)$ are functions solely depending on T and the masses of the participating particle. Figure 1.1 shows the effect of a non-zero value of a on the proton recoil spectrum. Positive values of a will shift it towards higher energies, negative values to lower energies. Physically, the influence of the angle between

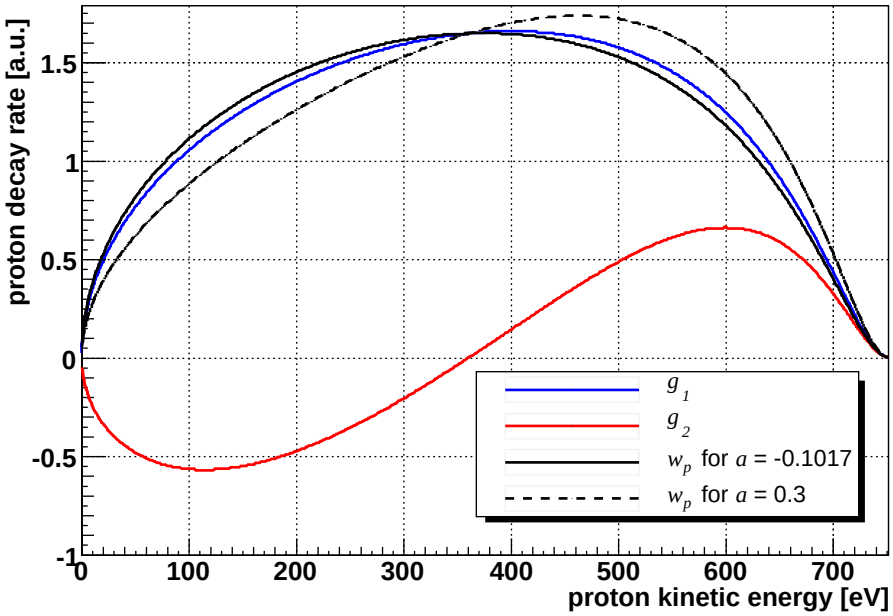

Figure 1.1: The functions $g_1(T)$, $g_2(T)$, and the proton decay rate $w_p(T)$.

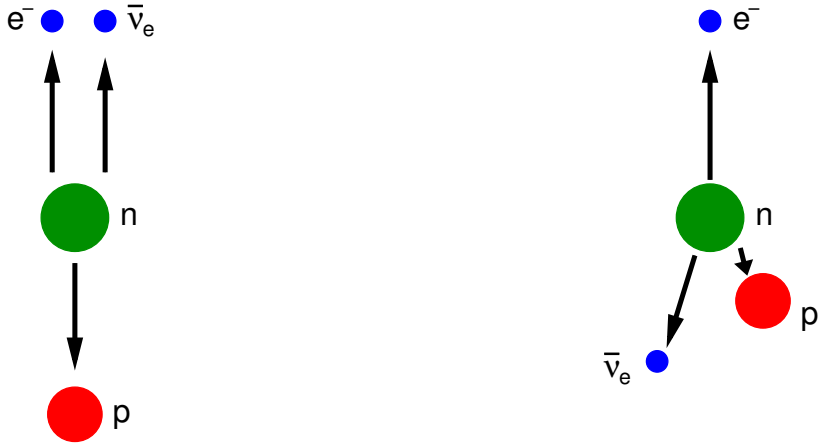

Figure 1.2: The influence of electron and anti-neutrino angular correlation on proton recoil: In the case depicted on the left, the proton recoil is large, in the case depicted on the right, it is small.

electron and anti-neutrino momenta becomes clear when considering the cases depicted in Fig. 1.2.

In the case that the momenta of electron and anti-neutrino are parallel to each other ($a = 1$), the proton recoil will be maximal. In case of anti-parallel emission, the recoil will be small. As such, measuring the shape of the proton recoil spectrum allows a determination of a.

2 Neutron decay

The reaction for the decay of the free neutron was given in (1.1). In the following, the phenomenology and theory of free neutron decay will be further discussed.

Specifically, section 2.1 will focus on the classical theory of the beta decay and derive the Hamiltonian and observables of the process, section 2.2 will give an overview of the neutron decay in the context of the Standard Model and section 2.3 will focus on the kinematics of the decay.

2.1 Classical Theory

2.1.1 Selection rules

Nuclear[1] beta decays can be classified broadly into two categories: *Allowed* decays, in which there is no transfer of angular momentum to the lepton and *forbidden* decays, in which the lepton carries away angular momentum. This terminology already indicates that decays with a transfer of angular momentum are strongly suppressed.

The reason for this is that a transition with lepton angular momentum l corresponds to a multipole expansion of the lepton wave function in terms of the quantity Rq, with R being the nuclear radius and q being the momentum transfer. A typical value would be $(qR)^l \approx (0.05)^l$ [Gro89, p. 51]. The square of this value is indicative of the suppression of forbidden transitions compared to allowed ones.

If one assumes the neutron to be pointlike (a good approximation in the case of the neutron decay), then there can be no angular momentum transfer to the leptons. Because of this, only allowed transitions will be considered in the following. Since there is no change of the angular momentum of the nucleus in allowed decays, the parity of the initial and final

[1] References to the nucleus in this section always apply to the neutron as well.

states will be the same: $\Delta\pi = 0$. Depending on the spins states of the leptons $\boldsymbol{\sigma}_\mathrm{e}$ and $\boldsymbol{\sigma}_{\overline{\nu}}$ coupling to total spin $\mathbf{S}$, there are two possible final states:

- The spins couple to $S = 0$ (singlet state). This transition is called Fermi-decay.
- The spins couple to $S = 1$ (triplet state). This transition is called Gamow-Teller-decay.

This results in the following selection rules for the spin $\mathbf{I}$ of the daughter nucleus:

$$\Delta I \equiv I_\mathrm{f} - I_\mathrm{i} = 0 \quad \text{for Fermi-decays} \tag{2.1}$$

$$\Delta I = 1 \text{ or } 0 \quad \text{for Gamov-Teller-decays (but not } (I_\mathrm{i} = 0) \rightarrow (I_\mathrm{f} = 0)) \tag{2.2}$$

Obviously, the spin of the nucleus doesn't change in a Fermi-decay. In a Gamov-Teller-decay, the spin of the nucleus changes if the spins of electron and anti-neutrino combine to either $S_\mathrm{z} = +1$ or $S_\mathrm{z} = -1$. By observing decays which fulfil only one of these selection rules, it is possible to study one of the corresponding transitions exclusively. In the case of the free neutron, both decay modes are possible.

2.1.2 The Hamiltonian of neutron decay

In analogy to the electro-magnetic four-current density

$$j_\mu^{em}(x) = -\overline{\psi}_\mathrm{e}(x)\gamma^\mu\psi_\mathrm{e}(x) \tag{2.3}$$

with the spinor ψ_e and the Dirac matrices $\gamma^\mu = (\gamma^0, \gamma^1, \gamma^2, \gamma^3)$

$$\gamma^0 = \begin{pmatrix} \mathbf{I} & 0 \\ 0 & -\mathbf{I} \end{pmatrix}, \quad \vec{\gamma} = \begin{pmatrix} 0 & \vec{\boldsymbol{\sigma}} \\ -\vec{\boldsymbol{\sigma}} & 0 \end{pmatrix}, \quad \gamma^5 = i\gamma^0\gamma^1\gamma^2\gamma^3$$

Fermi [Fer34] constructed Lorentz-invariant hadronic and leptonic current densities

$$V_\mu(x) = \overline{\psi}_\mathrm{p}(x)\gamma_\mu\psi_\mathrm{n}(x) \tag{2.4}$$
$$l^\dagger_\mu(x) = \overline{\psi}_\mathrm{e}(x)\gamma_\mu\psi_\nu(x) \tag{2.5}$$

Here, the spinors ψ_i denote the destruction operator for the corresponding particles, i.e. ψ signifies an ingoing particle or an outgoing anti-particle, while $\overline{\psi}$ signifies an outgoing particle or an ingoing anti-particle. He further assumed the interaction between the current densities to be pointlike, as shown in Fig. 2.1. Introducing the coupling constant G_β, the Hamiltonian of the beta decay then becomes

$$H_\beta(x) = \frac{G_\beta}{\sqrt{2}}\left(V^\mu(x)l^\dagger_\mu(x) + l^\mu(x)V^\dagger_\mu(x)\right) \tag{2.6}$$

The first term describes the β^- decay, the second term is the Hermitian conjugate of the first and describes the β^+ decay.

In Fermi's original theory, only vector-vector coupling[2] between the current densities is considered. However, Gamov and Teller showed that this is not the only possible Lorentz-invariant structure [Gam36]. Assuming invariance under Lorentz-, parity-, and time-reversal transformations, the following current densities are possible:

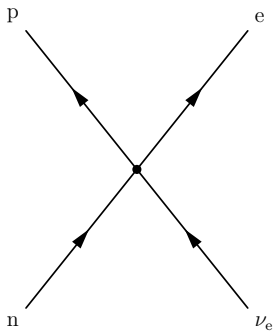

Figure 2.1: Feynman graph of the β^- decay as point-like interaction.

$\overline{\psi}\psi$	Scalar (S)
$\overline{\psi}\gamma_\mu\psi$	Vector (V)
$\overline{\psi}\gamma_\mu\gamma^\nu\psi$	Tensor (T)
$\overline{\psi}\gamma_5\psi$	Pseudoscalar (P)
$\overline{\psi}\gamma_5\gamma_\mu\psi$	Axial-vector (A)

[2] Since $\overline{\psi}\gamma_\mu\psi$ behaves like a polar vector under Lorentz transformations.

In principle, any two of these current densities can be combined to an interaction of the current-current-coupling type. However, since the Hamiltonian has to be either scalar or pseudoscalar, only couplings of the type SS, VV, TT, AA, PS, or VA are possible.

In 1956, Lee and Yang postulated that parity might not be conserved in the weak interaction [Lee56] and gave the most general form of the Hamiltonian of beta decay which can written as [Glü95]

$$H_\beta = \frac{G_W}{\sqrt{2}} \sum_j \Big(L_j (\overline{\psi}_\mathrm{p} \Gamma_j \psi_\mathrm{n})(\overline{\psi}_\mathrm{e} \Gamma_j (1+\gamma_5)\psi_\nu) + R_j (\overline{\psi}_\mathrm{p} \Gamma_j \psi_\mathrm{n})(\overline{\psi}_\mathrm{e} \Gamma_j (1-\gamma_5)\psi_\nu) \Big) + \text{Hermitian conjugate} \quad (2.7)$$

where $j \in [S, V, T, P, A]$ and the operators Γ_j correspond to the current densities given above:

$$\Gamma_S = 1 \qquad \Gamma_V = \gamma_\mu$$
$$\Gamma_T = -i\frac{[\gamma_\mu, \gamma_\nu]}{2\sqrt{2}} \qquad \Gamma_P = \gamma_5$$
$$\Gamma_A = -i\gamma_\mu\gamma_5$$

G_W is an overall weak coupling constant. $(1+\gamma_5)\psi_\nu$ and $(1-\gamma_5)\psi_\nu$ project out the left- and right-handed components of the neutrino wave function, respectively. Accordingly, the first term of the sum corresponds to left-handed currents and the second term to right-handed currents. L_j and R_j are coupling constants which can be experimentally determined[3]. If parity is assumed to be conserved, then $L_j = R_j$ and in the case of time reversal invariance, all constants are real.

From this it follows that an experiment which can show $L_j \neq R_j$ for any j proves parity violation, and an experiment which can show the existence of phase differences between coupling constants is a test for time reversal invariance.

[3] They relate to the coupling constants C_j and C_j' used in [Lee56] as follows: $C_j = \frac{G_W}{\sqrt{2}}(L_j + R_j)$ and $C_j' = \frac{G_W}{\sqrt{2}}(L_j - R_j)$

2.1.3 The V-A theory

So far, experiments have shown that only the left-handed components of vector and axial-vector couplings contribute to the beta decay in measurable quantities. The absence of right-handed currents indicates that parity is *maximally* violated in beta decay.

The remaining coupling constants L_A and L_V have approximately the same absolute value, but opposite signs[4]. This leads to the Hamiltonian of the V-A theory of beta decay

$$\begin{aligned} H_{V-A} &= \frac{G_W}{\sqrt{2}} \sum_{V,A} L_j (\overline{\psi}_\mathrm{p} \Gamma_j \psi_\mathrm{n})(\overline{\psi}_\mathrm{e} \Gamma_j (1+\gamma_5)\psi_\nu) + \text{ h.c.} \\ &= g_V \left(\overline{\psi}_\mathrm{p} \gamma_\mu (1+\lambda\gamma_5)\psi_\mathrm{n}\right) \left(\overline{\psi}_\mathrm{e} \gamma_\mu (1+\gamma_5)\psi_\nu\right) + \text{ h.c.} \end{aligned} \tag{2.8}$$

Here, $g_V = G_W L_V$ and $g_A = G_W L_A$ are the vector and axial-vector coupling constants and

$$\lambda := \frac{g_A}{g_V} = \frac{|g_A|}{|g_V|} e^{i\Phi_{AV}} \tag{2.9}$$

is their ratio. The vector coupling corresponds to Fermi decays, the axial-vector coupling to Gamov-Teller decays.

2.1.4 Observables of neutron decay

The total decay probability can be calculated by using Fermi's Golden Rule

$$W = \frac{2\pi}{\hbar} |\mathcal{M}_\mathrm{fi}|^2 \cdot \rho'_\mathrm{e}(E_\mathrm{e}) \tag{2.10}$$

where $\mathcal{M}_\mathrm{fi}$ is the transition matrix element and $\rho'_\mathrm{e}(E_\mathrm{e})$ a phase space factor, which will be discussed in more detail in section 2.3.1. Using the Hamiltonian (2.7) or (2.8), $\mathcal{M}_\mathrm{fi}$ can be obtained as a function of the coupling constants. In [Jac57], the distribution of electron energy and the directions of electron and anti-neutrino for the decay of an oriented spin 1/2 nucleus[5]

[4] $\lambda := L_A/L_V \in [-1.273, -1.263]$ according to [Glü95].
[5] For nuclei with different spins, there is an additional term.

is calculated to be[6]

$$\frac{\mathrm{d}W}{\mathrm{d}E_\mathrm{e}\mathrm{d}\Omega_\mathrm{e}\mathrm{d}\Omega_{\overline{\nu}}} = \frac{G_W^2}{(2\pi)^4\hbar}\rho'_\mathrm{e}(E_\mathrm{e})\xi\cdot \\ \cdot\left\{1 + a\frac{\mathbf{p}_\mathrm{e}\mathbf{p}_{\overline{\nu}}}{E_\mathrm{e}E_{\overline{\nu}}} + b\frac{m_\mathrm{e}}{E_\mathrm{e}} + \frac{\mathbf{P}_\mathrm{n}}{P_\mathrm{n}}\left(A\frac{\mathbf{p}_\mathrm{e}}{E_\mathrm{e}} + B\frac{\mathbf{p}_{\overline{\nu}}}{E_{\overline{\nu}}} + D\frac{\mathbf{p}_\mathrm{e}\times\mathbf{p}_{\overline{\nu}}}{E_\mathrm{e}E_{\overline{\nu}}}\right)\right\} \quad (2.11)$$

where ξ is [Glü95]

$$\xi = (|L_S|^2+|L_V|^2+|R_S|^2+|R_V|^2)+3(|L_A|^2+|L_T|^2+|R_A|^2+|R_T|^2). \quad (2.12)$$

The two transition modes discussed in section 2.1.1 are recognizable in that structure: Fermi decay is a transition into a singlet state, the Gamov-Teller decay a transition into a triplet state. As such, the first term can be identified as describing the Fermi decay, the second term with the prefactor 3 as describing the Gamov-Teller decay. In the frame of the V-A theory, this simplifies to

$$\xi = |L_V|^2 + 3|L_A|^2 = \frac{|g_V|^2 + 3|g_A|^2}{G_W^2}. \quad (2.13)$$

In the following, the dependence of the correlation coefficients on the coupling constants in the most general case (taken from [Glü95]), their forms in V-A theory (taken from [Abe00] and [Glü95]) and the implications will be shortly discussed. If available, measured values are given as listed in [Yao06].

The Fierz interference term b

In general theory, this term can be expressed as

$$b = \frac{2}{\xi}\mathrm{Re}\Big(L_S L_V^* + R_S R_V^* + 3\big(L_A L_T^* + 3R_A R_T^*\big)\Big). \quad (2.14)$$

Since it contains mixed terms of the scalar/vector and axial-vector/tensor type, it is 0 in the frame of the V-A theory. Therefore, a measurement of b is a test of the validity of that model.

[6] Jackson et al. derive the distributions for two additional cases, which will not be discussed here.

As stated in section 2.1.2, parity conservation would imply $L_j = R_j$ and in case of time reversal invariance, all coupling constants would be real. As such, it can be readily seen from (2.14) that a non-zero value of b would not be parity violating, nor would it violate time reversal invariance. To the author's knowledge, there has not been a direct measurement of b from the decay of the free neutron. In [Glü95], two values are listed which were obtained from nuclear beta decay; both are compatible with $b = 0$.

The electron-antineutrino correlation coefficient a

The angular correlation coefficient a takes the forms

$$a = \frac{1}{\xi}\left(|L_V|^2 - |L_S|^2 + |L_T|^2 - |L_A|^2 + |R_V|^2 - |R_S|^2 + |R_T|^2 - |R_A|^2\right) \tag{2.15}$$

and

$$a = \frac{1 - |\lambda|^2}{1 + 3|\lambda|^2} \tag{2.16}$$

in the general theory and the V-A theory, respectively. A value of $a \neq 0$ does not violate parity or time reversal invariance for the same reasons as given for b.

A measurement of a can give important information about the individual contributions of the different coupling types for a given decay. In the V-A theory, for a pure Fermi decay, a should be 1, for a pure Gamov-Teller decay, it should be $-\frac{1}{3}$. As such, a precise measurement of a can be used to search for scalar and tensor coupling constants $\neq 0$.

From (2.16) it is also apparent that if one considers the V-A theory to be valid, a measurement of a is a possible method of determining the ratio of the vector and axial-vector coupling constants $|\lambda|$.

The current world average is $a = -0.103(4)$.

Experimentally, this correlation is of course not directly accessible due to the difficulty of actually detecting neutrinos. Hence it is necessary to measure some experimentally accessible parameter which is sensitive to a. In addition to the proton spectrum, the shape of which is sensitive to a as has been shown in section 1, two other combinations of parameters offer possible ways to measure a [Byr94]. These are the distribution of decay

events as function of the angle between the electron and the proton, which will be used by the experiment aCORN to detemine a [Wie05], and the momentum spectrum of electrons which are emitted into a given range of angles relative to the proton momentum.

So far, all published values with high accuracy have been obtained by measuring the shape of the proton spectrum ([Dob75], [Str78]).

The electron asymmetry coefficient A and anti-neutrino asymmetry coefficient B

The coefficients A and B depend on the coupling constants as follows:

$$A = \frac{2}{\xi}\mathrm{Re}\big(-|L_A|^2 - L_A L_V^* + |L_T|^2 + L_S L_T^* + |R_A|^2 + R_A R_V^* - |R_T|^2 - R_S R_T^*\big) \quad (2.17)$$

$$B = \frac{2}{\xi}\Big\{\mathrm{Re}\big(|L_A|^2 - L_A L_V^* + |L_T|^2 - L_S L_T^* - |R_A|^2 + R_V R_A^* - |R_T|^2 + R_S R_T^*\big) + \frac{m_\mathrm{e}}{E_\mathrm{e}}\mathrm{Re}\big(-L_S L_A^* - L_V L_T^* + 2L_A L_T^* + R_S R_A^* + R_V R_T^* - 2R_A R_T^*\big)\Big\} \quad (2.18)$$

Using the same arguments as in the previous section, it can readily be seen that non-zero values for either A or B would mean parity violation, but not time invariance violation. The experimental proof that $A \neq 0$ in the decay of ^{60}Co by Wu et al. [Wu57] showed that the weak interaction is parity violating.

In the V-A theory, A and B become

$$A = -2\frac{|\lambda|^2 + \mathrm{Re}(\lambda)}{1 + 3|\lambda|^2} \quad (2.19)$$

$$B = +2\frac{|\lambda|^2 - \mathrm{Re}(\lambda)}{1 + 3\lambda^2} \quad (2.20)$$

and as such offer the possibilities to determine λ. Comparing the values obtained for λ by the measurements of a, A and B is an important test for the consistency of the V-A theory. World averages of the coefficients are $A = -0.1173(13)$ and $B = 0.981(4)$.

The triple correlation coefficient D

The most general dependence of D on the coupling constants is

$$D = \frac{2}{\xi}\mathrm{Im}(L_S L_T^* - L_V L_A^* + R_S R_T^* - R_V R_A^*) \tag{2.21}$$

which in V-A theory translates to

$$D = 2\frac{\mathrm{Im}(\lambda)}{1+3|\lambda|^2}. \tag{2.22}$$

A non-zero value of D would not be parity violating, but it would indicate that time reversal invariance was violated, since otherwise the coupling constants would not contain an imaginary part.

Since a measurement of D is sensitive to the complex part of the coupling constants, it also allows a measurement of the phase shift Φ_{AV} introduced in (2.9).

Reference [Yao06] lists a value of $-0.0004(6)$ for D and $180.06(7)^\circ$ for Φ_{AV}.

The neutron lifetime τ_n

The neutron lifetime τ_n can be obtained by first integrating the differential decay probability (2.11) and then taking the inverse, which yields

$$\tau_\mathrm{n} = \frac{2\pi^3}{m_\mathrm{e}^5 G_W^2 \xi f \bar{f}_\mathrm{b}} \tag{2.23}$$

with the phase space factor

$$f = m_\mathrm{e}^{-5}\int_{m_\mathrm{e}}^{E_{0,\mathrm{e}}} \rho_\mathrm{e}' \mathrm{d}E_\mathrm{e} = 1.636$$

and

$$\bar{f}_\mathrm{b} = 1 + 0.654b.$$

In V-A theory and assuming $b = 0$, this simplifies to

$$\tau_\mathrm{n} = \frac{2\pi^3}{m_\mathrm{e}^5 f}\frac{1}{|g_V|^2 + 3|g_A|^2}. \tag{2.24}$$

This means that the neutron lifetime is the only observable which contains direct information about the coupling constants; all other observables only contain information about their relative strengths.

The current world average is $\tau_n = 885.7(8)$ s[7].

2.2 Neutron decay in the Standard Model

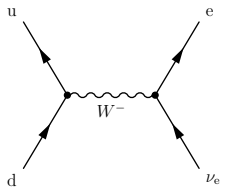

Figure 2.2: Feynman graph of the β^- decay on the quark level.

The Standard Model of particle physics comprises the Quantum chromodynamics (QCD) and the theory of electro-weak interaction as formulated by Salam, Glashow, and Weinberg.

In the Standard Model, only vector and axial-vector components are present in the weak interaction; it follows the V-A theory. However, in contrast to the classical theory described in section 2.1, the interaction is no longer point-like. Neutron and proton are not fundamental particles, but composed out of quarks (see table 1.1). The decay of a neutron (udd) into a proton (uud) is described on a more fundamental level as the transition of a down quark into an up quark, as is depicted in Fig. 2.2.

The weak interaction is mediated by the $W^{\pm}$ and Z^0 exchange bosons. This is taken into account by introducing a propagator term into the transition matrix element, analogous to the photon propagator in QED (see for example [Pov99, p. 139]):

$$\mathcal{M}_{\mathrm{fi}} \propto g \cdot \frac{1}{Q^2 + M_B^2} \cdot g \tag{2.25}$$

where Q is the momentum transfer, g is the weak charge which couples to the exchange boson and M_B is the mass of the exchange boson. In beta decay, Q is usually negligibly small compared to M_B[8], so one can assume the propagator to be constant in very good approximation. For small

[7] The recent result of Serebrov et al. is 6.5 standard deviations from the world average [Ser05] and is not included in this value.

[8] $M_W = 80.406(29)$ GeV [Yao06]

momentum transfers, the boson can only exist in the timeframe given by HEISENBERG's uncertainty relation, for the beta decay as depicted in Fig. 2.2, this means $\tau_W < \hbar/M_W$. If one assumes a maximum speed of c, this corresponds to a range of $\approx 2.5{\cdot}10^{-3}$ fm. As such, the point-like interaction model for the beta decay which was discussed in section 2.1 is included in the Standard Model in the limit of low momentum transfer.

The charged exchange bosons only couple to left-handed fermions and right-handed anti-fermions. As such, parity violation is included in the Standard Model description of the weak interaction.

It is assumed that the weak interaction is universal, i.e. that the weak charge g is the same for all fundamental particles (leptons and quarks). However, it is found that the coupling constant is larger when determined from purely leptonic decays (such as muon decay) than it is when determined from semi-leptonic transitions (such as beta decay). In the Standard Model this discrepancy is explained by the fact that the eigenstates of the quarks in respect to the weak interaction are not their mass eigenstates. Instead, they are a linear combination of the mass eigenstates of the quarks from all three generations with the same charge. This was first postulated by CABIBBO in 1963 [Cab63]. Applying his theory to the quark picture[9], the weak eigenstates of the quarks are correlated to their mass eigenstates by a rotation matrix and the CABIBBO-angle Θ_C:

$$\begin{pmatrix} |d'\rangle \\ |s'\rangle \end{pmatrix} = \begin{pmatrix} \cos\Theta_C & \sin\Theta_C \\ -\sin\Theta_C & \cos\Theta_C \end{pmatrix} \cdot \begin{pmatrix} |d\rangle \\ |s\rangle \end{pmatrix} \tag{2.26}$$

The primed values correspond to the weak eigenstates, the unprimed values to the mass eigenstates of the quarks. It is convention that the eigenstates of the negatively charged quarks are rotated and not those of the positively charge quarks.

To include the third generation of quarks, the rotation matrix was expanded to the CABIBBO-KOBAYASHI-MASKAWA (CKM) matrix [Kob73]:

[9] Quarks were first postulated by GELL-MANN in 1964 [GM64].

$$\begin{pmatrix} |d'\rangle \\ |s'\rangle \\ |b'\rangle \end{pmatrix} = \begin{pmatrix} V_{\mathrm{ud}} & V_{\mathrm{us}} & V_{\mathrm{ub}} \\ V_{\mathrm{cd}} & V_{\mathrm{cs}} & V_{\mathrm{cb}} \\ V_{\mathrm{td}} & V_{\mathrm{ts}} & V_{\mathrm{tb}} \end{pmatrix} \cdot \begin{pmatrix} |d\rangle \\ |s\rangle \\ |b\rangle \end{pmatrix} \tag{2.27}$$

The probability for a transition of a quark $|i\rangle$ to a quark $|f\rangle$ is proportional to the square of the corresponding matrix element $|V_{\mathrm{fi}}|^2$. In the case of beta decay, this is taken into account by an additional factor $|V_{\mathrm{ud}}|$ in the coupling constants:

$$G_V = g_V \cdot V_{\mathrm{ud}}, \qquad G_A = g_A \cdot V_{\mathrm{ud}}. \tag{2.28}$$

Since all the observables listed in section 2.1.4 except for the neutron lifetime only depend on the relative strengths of the coupling constants, they take the same form in the Standard Model as in V-A theory, with the exception of τ_{n}. There, an additional factor $|V_{\mathrm{ud}}|^2$ appears in the denominator.

In the Standard Model, assuming a number of three quark generations, the CKM matrix has to be unitary; under this condition, the allowed ranges for the $|V_{\mathrm{ij}}|$ are, according to Ref. [Yao06]:

$$V_{\mathrm{CKM}} = \begin{pmatrix} [0.9736, 0.97407] & [0.2262, 0.2282] & [0.00387, 0.00405] \\ [0.2261, 0.2281] & [0.97272, 0.9732] & [0.04141, 0.04231] \\ [0.0075, 0.00846] & [0.04083, 0.04173] & [0.999096, 0.999134] \end{pmatrix} \tag{2.29}$$

For the first row, the implied unitarity gives the condition

$$|V_{\mathrm{ud}}|^2 + |V_{\mathrm{us}}|^2 + |V_{\mathrm{ub}}|^2 = 1 \tag{2.30}$$

Hence, by measuring the squares of the matrix elements, the unitarity of the CKM matrix (and as such the validity of the Standard Model) can be tested. Since $|V_{\mathrm{ud}}|^2$ contributes most to the sum (2.30), a high-precision measurement of this value is desirable.

Considering the dependence of the observables of neutron decay on the coupling constants as given in section 2.1.4, it becomes clear that to determine both of the free parameters λ and $|V_{\mathrm{ud}}|$, it is necessary to measure

the lifetime τ_{n} and one more of the given observables.

2.3 Kinematics

The decay of the free neutron is a three-body decay. Since the involved energies are large compared to the rest masses of both the electron and the neutrino, the process has to be treated relativistically for these two particles; in the following, all particles will be treated relativistically using the four-momenta $p_i = (E_i, \mathbf{p}_i)$.
Additionally, the neutrino will be treated as massless[10]. A general three-body decay is depicted in Fig. 2.3.

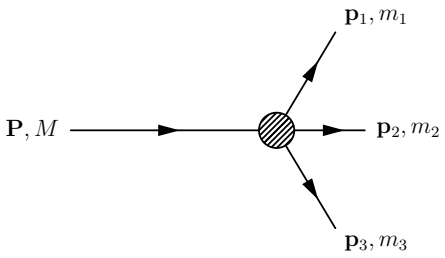

Figure 2.3: A particle with momentum $\mathbf{P}$ and mass M decaying into three daughter particles with momenta p_{i} and masses m_{i} (i = 1,2,3).

If we define the sum of two four-momenta

$$p_{\mathrm{i}} + p_{\mathrm{j}} =: p_{\mathrm{ij}} \quad \text{and} \quad m_{\mathrm{ij}}^2 := p_{\mathrm{ij}}^2$$

then for a given m_{12}, the momentum $|\mathbf{p}_3|$ in the rest frame of the mother particle becomes [Yao06]

$$|\mathbf{p}_3| = \frac{\left[\left(M^2 - (m_{12} + m_3)^2\right)\left(M^2 - (m_{12} - m_3)^2\right]^{\frac{1}{2}}}{2M} \tag{2.31}$$

[10] While the measurement of neutrino oscillations implies $m_\nu \neq 0$, measurements so far only give an upper limit for the neutrino mass, which is negligibly small compared to the other masses involved in the neutron beta decay.

This value is maximal in the case of $m_{\mathrm{ij}} = m_1 + m_2$, which physically means that particles 1 and 2 have the same vector velocity. Thus, using the masses of the particles listed in [Yao06], we can calculate the endpoint energies $E_{0,\mathrm{i}}$ for the daughter particles using the relativistic energy-momentum relation[11]

$$E = \sqrt{m_0^2 + \mathbf{p}^2} \tag{2.32}$$

The values of $E_{0,\mathrm{i}}$ are shown in table 2.1 along with the masses and the maximum kinetic energies of the particles.

Particle	Index i	$m_{0,\mathrm{i}}$ [MeV/c^2]	$E_{0,\mathrm{i}}$ [MeV]	$E_{0,\mathrm{i}} - m_{0,\mathrm{i}}$ [MeV]
Neutron	n	939.56536(8)		
Proton	p	938.27203(8)	938.27278(8)	0.00075(11)
Electron	e	0.510998901(20)	1.29258(11)	0.78158(13)
Anti-neutrino	$\bar{\nu}$	$< 0.000\ 002$	0.78201(11)	0.78201(11)
$m_{\mathrm{n}} - m_{\mathrm{p}} - m_{\mathrm{e}} - m_{\bar{\nu}}$		0.78233(11)		

Table 2.1: Rest masses $m_{0,\mathrm{i}}$, end-point energies $E_{0,\mathrm{i}}$ and maximal kinetic energies of the particles participating in neutron beta decay. The energy values were calculated by using formulas (2.31) and (2.32).

2.3.1 Lepton spectra

The energy distribution of the daughter particles is dependent on the available phase space of the reaction. Neglecting for a moment the kinetic energy of the proton, and purely considering the phase space of the electron and the neutrino, we can calculate the beta spectrum of the electron from the number of states in a given phase space volume $\mathrm{d}^3p_{\mathrm{e}}\mathrm{d}^3p_{\bar{\nu}}$ and using the

[11] With the convention $c = 1$ for convenience.

energy relation $E_\mathrm{e} + E_{\overline{\nu}} = m_\mathrm{n} - m_\mathrm{p} =: E_0$[12] [Pov99, p. 227].

The beta spectrum then becomes

$$\mathrm{d}\rho_\mathrm{e} = \frac{(4\pi)^2}{(2\pi\hbar)^6} E_\mathrm{e} \sqrt{E_\mathrm{e}^2 - m_\mathrm{e}^2} \cdot (E_0 - E_\mathrm{e})^2 \mathrm{d}E_\mathrm{e}. \tag{2.33}$$

Instead of E_0, we will use the more accurate $E_{0,\mathrm{e}}$ in the following calculations.

The Coulomb-interaction between proton and electron leads to a shift of the electron spectrum to slightly lower energies. To take this effect into consideration, the Fermi-function $F(Z, E)$ is introduced, which for non-relativistic electrons in the field of a point-like nucleus is given by [Pov99, p. 279]

$$F(Z, E) = \frac{2\pi\eta}{1 - e^{2\pi\eta}} \quad \text{with} \quad \eta = \pm\frac{Z\alpha}{v_\mathrm{e}} \quad \text{for} \quad \beta^\mp. \tag{2.34}$$

Here, v_e is the velocity of the electron in units of c and α is the fine-structure constant. In the decay of the free neutron ($Z = 1$), $\eta \ll 1$ already for small energies of the electron, and as such $F \approx 1$.

As such, the electron spectrum (2.33) is modified to

$$\begin{aligned} \rho'_\mathrm{e}(E_\mathrm{e}) &:= F(1, E_\mathrm{e})\rho_\mathrm{e}(E_\mathrm{e}) \\ &= \frac{(4\pi)^2}{(2\pi\hbar)^6} F(1, E_\mathrm{e}) E_\mathrm{e} \sqrt{E_\mathrm{e}^2 - m_\mathrm{e}^2} \cdot (E_{0,\mathrm{e}} - E_\mathrm{e})^2. \end{aligned} \tag{2.35}$$

The deviations between (2.33) and (2.35) are small and only important at low electron energies.

Analogous to the electron spectrum (2.33), the neutrino spectrum can be calculated to be

$$\mathrm{d}\rho_{\overline{\nu}} = \frac{(4\pi)^2}{(2\pi\hbar)^6} \sqrt{(E_{0,\bar{\nu}} + m_\mathrm{e} - E_{\overline{\nu}})^2 - m_\mathrm{e}^2} (E_{0,\bar{\nu}} + m_\mathrm{e} - E_{\overline{\nu}}) E_{\overline{\nu}}^2 \mathrm{d}E_{\overline{\nu}} \tag{2.36}$$

The spectra for both electrons and neutrinos are depicted in Fig. 2.4.

2.3.2 Proton spectrum

A relativistic derivation of the proton recoil spectrum can be found in [Nac68][13]. The derivation is similar to that of the electron spectrum de-

[12] Since we neglect the proton recoil, E_0 is obviously slightly larger than the value $E_{0,\mathrm{e}}$ which is given in table 2.1.

[13] In that paper there is however, a sign error in the last line of eq.(4.5) [Hab97].

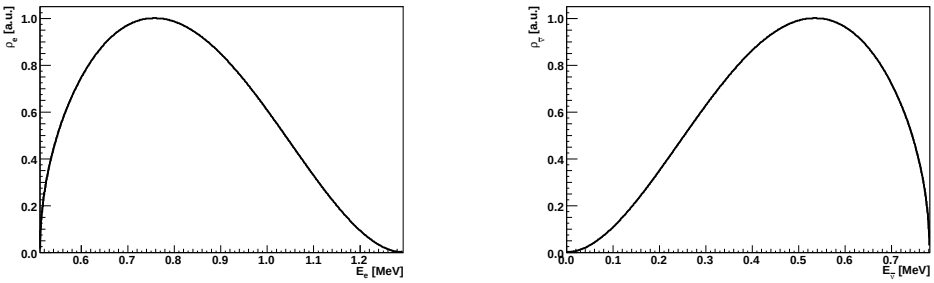

Figure 2.4: The energy spectra of electrons (left) and neutrinos (right) from the decay of the free neutron (with $F(Z, E) = 1$).

scribed in the previous section. Again, the transition probability is a product of a phase space factor, a matrix element factor and a COULOMB-correction factor. Neglecting the latter, the proton spectrum is calculated to be

$$\mathrm{d}w(T) = \frac{\Sigma\Delta^3 G_V^2}{2^4\pi^3(1+2\delta)}\left(\frac{\sigma - x^2}{\sigma}\right)^2\sqrt{1-\sigma}\Bigg\{\left(1+\frac{x^2}{\sigma}-\sigma\right)- \\ -\frac{1}{3}\frac{\sigma-x^2}{\sigma}(1-\sigma)+\lambda^2\left[\left(1+\frac{x^2}{\sigma}+\sigma\right)-\frac{1}{3}\frac{\sigma-x^2}{\sigma}(1-\sigma)\right]\Bigg\}\mathrm{d}T \quad (2.37)$$

with T being the kinetic energy of the proton, λ as introduced in (2.9) and the quantities

$$\Delta = m_\mathrm{n} - m_\mathrm{p}, \qquad \Sigma = m_\mathrm{n} + m_\mathrm{p},$$
$$x = m_\mathrm{e}/\Delta, \qquad \delta = \Delta/\Sigma,$$
$$\sigma = 1 - \frac{2m_\mathrm{n}}{\Delta^2}T.$$

For this work, a more convenient form of the spectrum which contains the correlation coefficients a and b directly is given in 2.3.2. It becomes

$$w_\mathrm{p}(T) = m_\mathrm{n}\frac{G_\mathrm{W}^2\xi}{4\pi^3}\left[W_\mathrm{p}(E_\mathrm{e,max}, T) - (E_\mathrm{e,min}, T)\right] \quad (2.38)$$

$$W_{\mathrm{p}}(E_{\mathrm{e}}, T) = \frac{1}{2}(1+a)E_{\mathrm{e}}^2\big(\Delta - \frac{2}{3}E_{\mathrm{e}}\big) + am_{\mathrm{n}}E_{\mathrm{e}}(T - T_{\max}) + bm_{\mathrm{e}}E_{\mathrm{e}}\big(\Delta - \frac{1}{2}E_{\mathrm{e}}\big) \quad (2.39)$$

with Δ as defined above, the maximum kinetic energy of the protons $T_{\max}$

$$T_{\max} = \frac{\Delta^2 - m_{\mathrm{e}}^2}{2m_{\mathrm{n}}} \quad (2.40)$$

and the E_{e} boundaries for a fixed T value

$$E_{\mathrm{e,min/max}} = \frac{1}{2}\Big[\Delta \mp p + \frac{m_{\mathrm{e}}^2}{\Delta \pm p}\Big] \quad (2.41)$$

where p denotes the proton momentum. Of note is that this spectrum uses the *infinite nucleon mass* (INM) approximation, which assumes $m_{\mathrm{n}} \to \infty$, $m_{\mathrm{p}} \to \infty$ and Δ being equal to the real, finite value. Complete radiative and COULOMB corrections to the spectrum can be found in Ref. [Glü93].

The shape of the spectrum (without radiative and COULOMB corrections) is depicted in Fig. 1.1.

3 The spectrometer aSPECT

The retardation spectrometer *a*SPECT has been designed to measure the observable a of the free neutron decay (see section 2.1.4) with an absolute precision of $\delta a \approx 3 \cdot 10^{-4}$ [Zim00, Glü05]. In the following section, the design of the spectrometer will be discussed.

3.1 Principle of operation

It has been shown in section 1 that the shape of the proton spectrum depends on the value of a. *a*SPECT is a retardation spectrometer, which measures the integral proton spectrum above a certain adjustable energy threshold. A sketch of the spectrometer can be seen in Fig. 3.1.

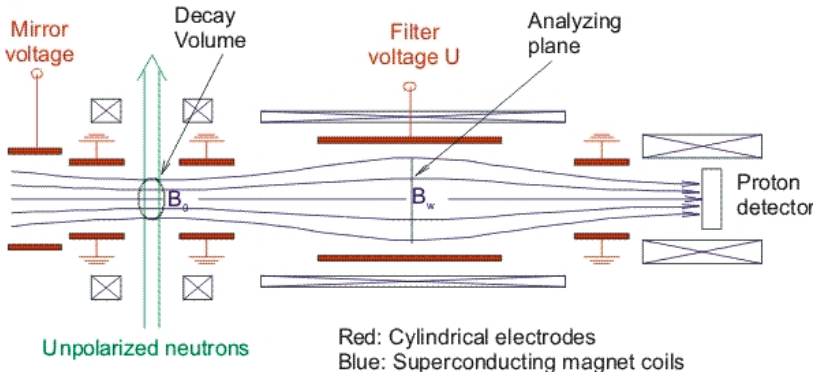

Figure 3.1: Schematic layout of the spectrometer *a*SPECT.

Guiding the protons to the detector and energy selection

A beam of unpolarized neutrons passes through the *decay volume* of the spectrometer, in which a strong magnetic field B_0 is applied. Protons and electrons from a neutron decay event which have an initial momentum component towards the detector, which is mounted on top of the spectrometer, are guided along the magnetic field lines to this detector. Protons which are initially emitted in the opposite direction are reflected towards the decay volume by a mirror voltage electrode which is set to a potential of 1000 V. As such, 4π detection of protons is achieved.

Between the decay volume and the detector, the *analyzing plane* (AP) is situated, consisting of a cylindrical electrode which can be put to a potential U_A. This results in a potential barrier which only protons with kinetic energies higher than $e \cdot U_\mathrm{a}$ can overcome. The effect of the potential barrier can be described by a transmission function, which gives the probability that a proton with a certain kinetic energy passes the analyzing plane. It is necessary to know this function accurately; if the motion of the protons is kept adiabatic[1], the transmission function can be expressed analytically and depends only on U_A and the magnetic field values in the decay volume B_0 and the analyzing plane B_A. A more thorough discussion of the analyzing plane and the transmission function will be done in section 3.3.

The detector itself is put to a high negative potential U_det to accelerate the protons so they can be detected[2].

The inverse magnetic mirror effect

Initially, the momentum vector of the emitted protons is oriented randomly in respect to the magnetic field lines. However, to measure the shape of the proton spectrum accurately, it should be oriented parallel to the magnetic field lines in the region of the analyzing plane. Since the electrostatic potential barrier is only sensitive to the longitudinal part $\mathbf{p}_{||}$ of the proton momentum, the energy selection would not work on the total kinetic energy of the proton, but only on the part $\mathbf{p}_{||}^2/2m_\mathrm{p}$.

[1] I.e. if the change of the magnetic fields is small during one proton orbit.

[2] As is listed in table 2.1, the maximum kinetic energy of protons from neutron decay is ≈ 750 eV.

To align the proton momentum vector along the field lines, the *inverse magnetic mirror effect* or *magnetic adiabatic collimation* is used:

The motion of a charged particle in a spatially slowly changing magnetic field can be split in first approximation into a gyration around a magnetic field line and a linear motion along this field line. If the magnetic field changes slowly enough, the magnetic flux through the particle's orbit (defined by the gyration radius r) remains constant: $Br^2\pi = \text{const.}$ (see e.g. [Jac62, p. 419 ff.]). This can be expressed in several ways involving the particle's gyration radius, its transverse momentum $p_\perp$ and its magnetic momentum, leading to the *adiabatic invariants*

$$Br^2, p_\perp^2/B \quad \text{and} \quad \gamma\mu \tag{3.1}$$

with $\mu \propto \omega_B r^2$ being the magnetic moment of the particle's current loop.

In the following, we consider a particle moving in a magnetic field acting in z direction, but having a gradient, as shown in Fig. 3.2, starting out at a point with field strength B_0 and with initial momentum components $p_{||0}$ parallel and $p_{\perp 0}$ transverse to the magnetic fieldlines. Since total momentum and energy have to be conserved, the relation

$$p_{||}^2 + p_\perp^2 = p_0^2 \tag{3.2}$$

is true for every point along the z axis. Re-writing (3.1) to

$$\frac{p_\perp^2}{B} = \frac{p_{\perp 0}^2}{B_0} \tag{3.3}$$

we find that the parallel component of the particle's momentum is given by

$$p_{||}^2 = p_0^2 - p_{\perp 0}^2 \frac{B}{B_0}. \tag{3.4}$$

With increasing magnetic field, the right-hand side of (3.4) will eventually vanish and the particle will be reflected. This effect can be used to trap charged particles (for example a plasma) in magnetic "bottles" which have strong magnetic fields at the ends and a low magnetic field in the middle.

Conversely, if the particle moves from a region with high magnetic field to a low-field region, $p_{||}$ will increase accordingly. This effect is used in *a*SPECT, and the ratio of the magnetic fields is $\frac{B_0}{B_A} \approx 5$.

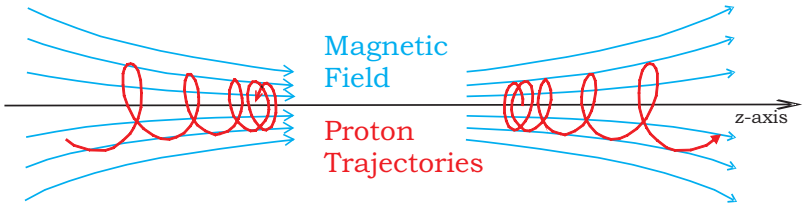

Figure 3.2: Proton trajectories in increasing (left) and decreasing (right) magnetic fields (from [Sim06]).

At the detector, a high magnetic field is applied again, to focus the protons on the comparatively small area. Consequently, there is the need for a negative electrostatic potential at the detector to help the protons overcome the magnetic barrier which is a result of the magnetic gradient between the analyzing plane and the detector.

Detection of protons

Since the actual energy selection is already done in the analyzing plane, the function of the detector is that of a counter. The applied high voltage serves two purposes: To accelerate the protons so that they can be detected, and to give them enough energy to overcome the magnetic barrier caused by the increase in the magnetic field towards the detector region. The events from the detector are both displayed for quick online analysis and written to disk completely for later in-detail offline analysis.

A detailed description of the detector, the electronics and the DAQ software is given in chapter 4.

3.2 The electric and magnetic fields

The electrode and magnet system was designed mainly by our colleagues from Johannes Gutenberg Universität Mainz. A schematic of the system setup can be seen in Fig. 3.3. The fields which are created by this array along the z-axis in the spectrometer are plotted in Fig. 3.4. Both pictures are taken from Ref. [AG05].

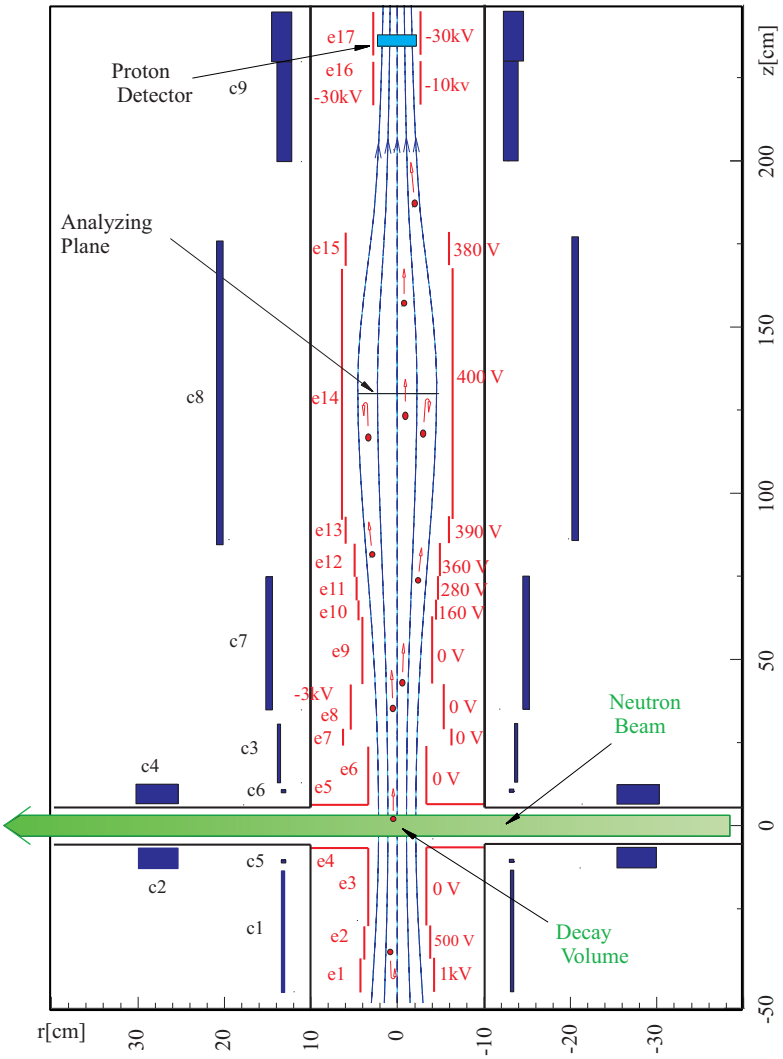

Figure 3.3: Sketch of the electrodes and magnetic coils in *a*SPECT (from [AG05]).

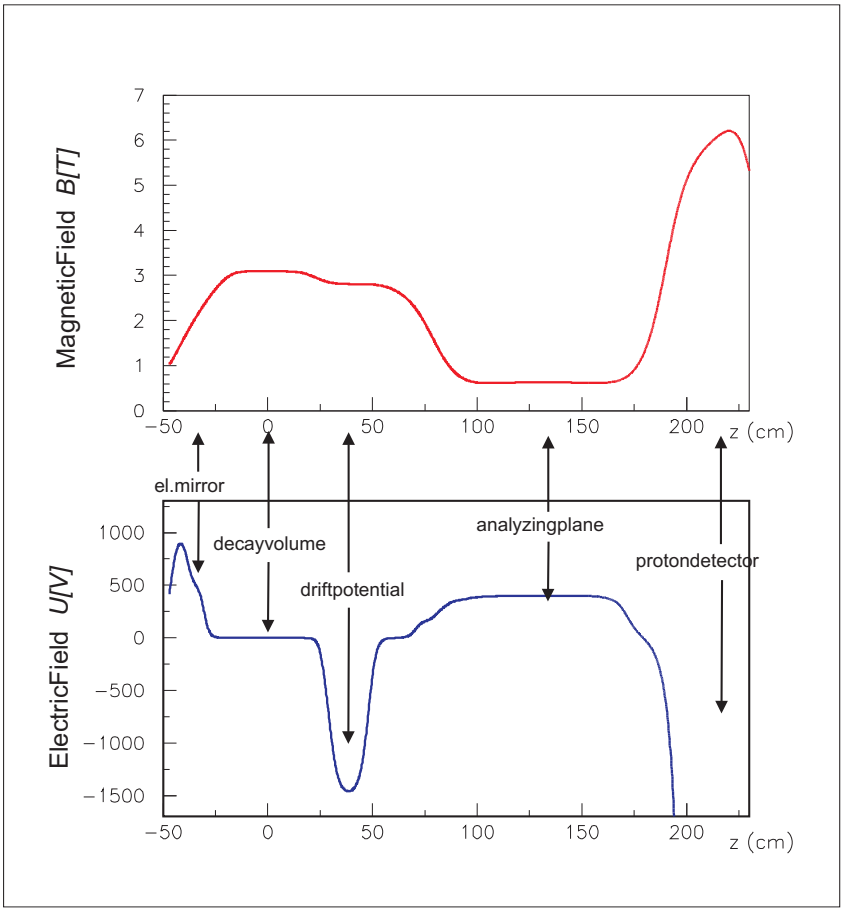

Figure 3.4: The configuration of the electric and magnetic fields along the z-axis of the spectrometer (taken from [AG05]).

The magnetic fields are generated by super-conducting magnetic coils, the electrode array was custom built and is gold plated. A picture of it is displayed in Fig. 3.5. The most important features of the electrode system are the following: The decay volume of the spectrometer is held on ground potential (0 V) by the electrodes e3 - e6; the magnetic field strength in that region is ≈ 3 T. Electrodes e1 and e2 provide the electrostatic mirror which is used to achieve 4 π detection of protons.

The analyzing plane of the spectrometer which acts as the energy filter of the spectrometer is situated in the middle of the cylindrical electrode e14. Protons with kinetic energies lower than $e \cdot U_{\mathrm{AP}}$ are reflected and move back towards the decay volume. A proton can become trapped between the potential barrier and the magnetic mirror and there is a finite probability that such a proton can gain a small amount of kinetic energy by non-adiabatic processes (like collisions with rest gas) to pass through the analyzing plane, if it is stored long enough. To prevent this, the ExB electrode e8 is used. It generates an electrostatic field perpendicular to the magnetic field lines. A charged particle moving in these two fields will drift with uniform velocity

$$\mathbf{v} \propto \frac{\mathbf{E} \times \mathbf{B}}{B^2} \tag{3.5}$$

in a direction normal to both the electric and magnetic field (see [Jac62]). Since the drift direction does not depend on the movement of the particle, protons passing through electrode e8 will be deflected into the same direction each time and hit the spectrometer wall after several oscillations, removing them. The electrode can also be used to control the position of the proton beam on the detector, as can be seen in Fig. 3.6.

The upper ExB drift electrode e16 was designed and built in Munich and serves two purposes. The voltage applied to it helps the protons which pass the analyzing plane to overcome the magnetic mirror produced by the magnetic field, which increases strongly towards the detector. The effect of the electrodes can be seen in Fig. 3.7. Without the electrostatic field of the ExB electrodes, a significant number of protons is reflected by the magnetic mirror effect generated by the increase of the magnetic field in the region between the analyzing plane and the detector. Applying only 1 kV to the electrodes results in an increase of the countrate by a factor of roughly 2. Secondly, it can be used in conjunction with the lower ExB electrode to center the proton beam on the detector.

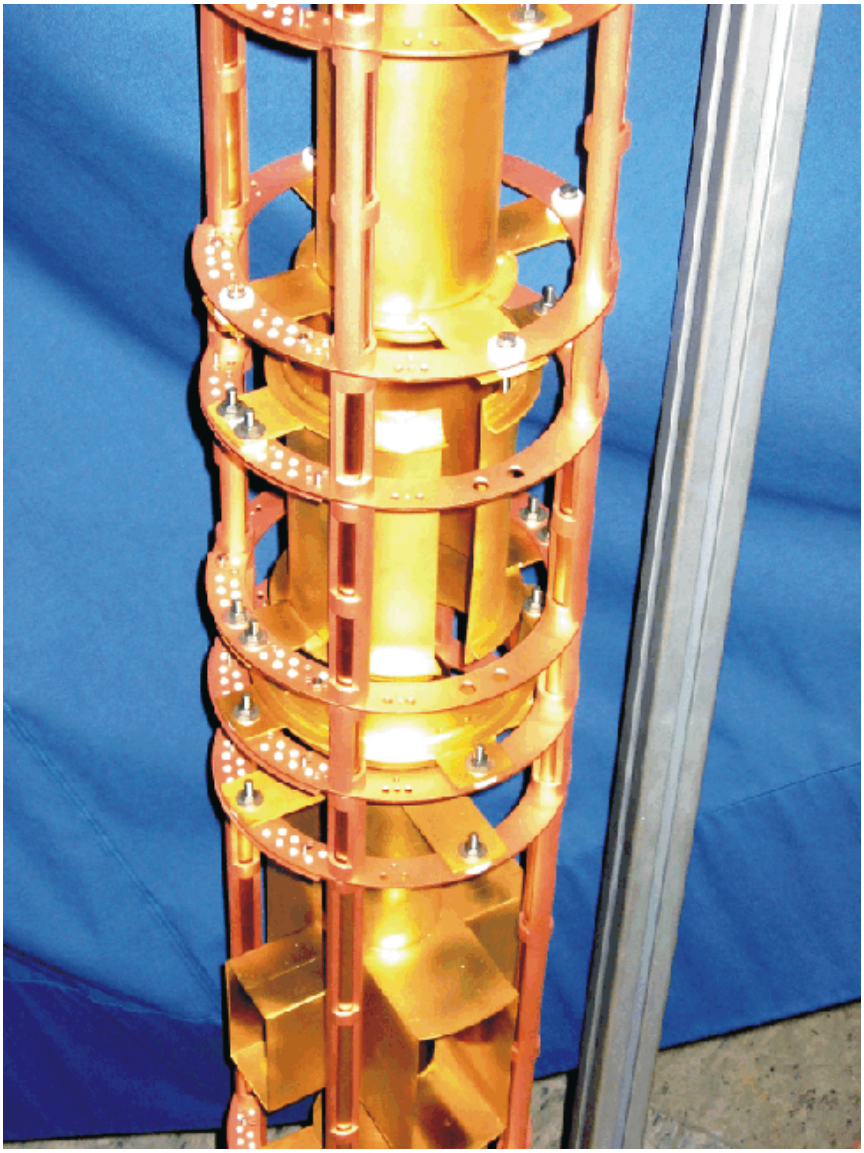

Figure 3.5: A picture of a part of the electrode system of *a*SPECT, showing the decay volume on the bottom and the lower ExB drift electrode (photograph courtesy of S. Baessler).

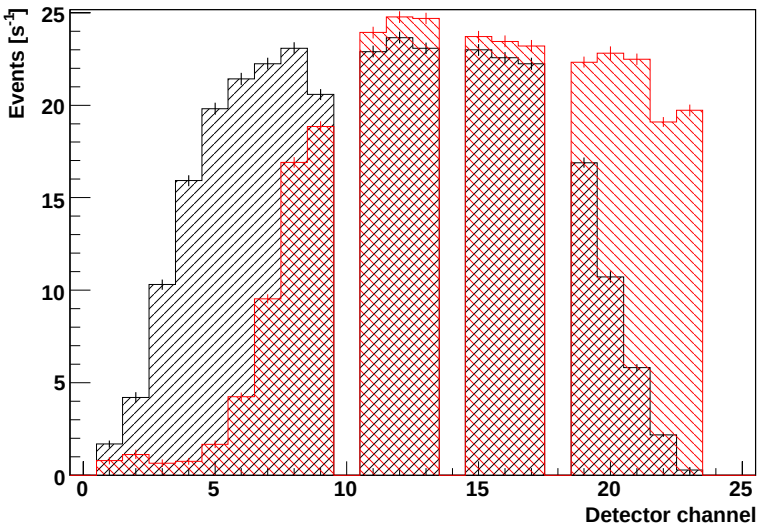

Figure 3.6: Effect of the voltage applied to electrode e8 on the position of the proton beam on the detector. The black area shows the count rates per channel with 0 V difference applied to the electrode, the red area the count rates with 1000 V applied. Channels 10, 14, and 18 were disabled in this measurement due to excessive noise.

Since it is important to know the exact shape of the magnetic fields in order to be sure that they fulfill the necessary conditions (adiabaticity of the proton movement, no traps for charged particles, homogeneity in the analyzing plane), they were measured carefully. Fig. 3.8 shows the measured magnetic field along the z-axis of the spectrometer compared to the calculated field strength. Details on the measurements and the field strength in the various regions of the spectrometer can be found in Ref. [AG05].

3.3 The transmission function

In section 3.1, the inverse magnetic mirror effect was described as a method to orient the proton momentum parallel to the magnetic field lines. In prac-

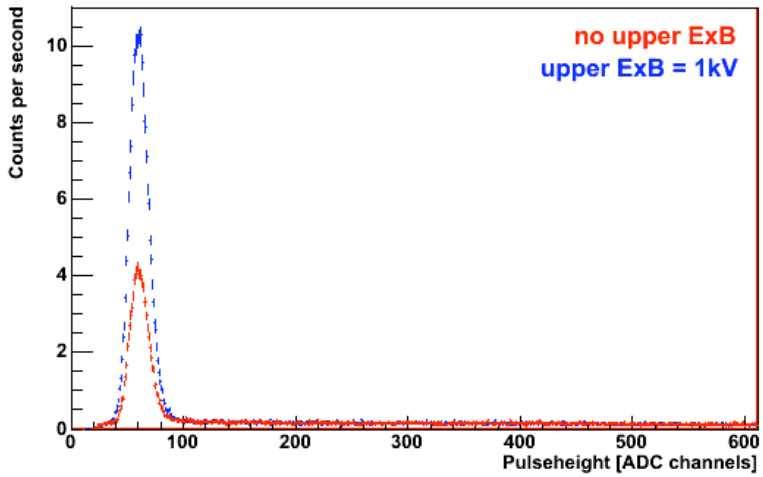

Figure 3.7: Pulseheight spectra taken with voltage applied to the upper ExB electrode and with the electrode on ground potential.

tice, this will never be fully the case, and therefore we need to investigate the transmission of protons depending on their angle to the z-axis of the spectrometer[3] θ[4]. As before, we decompose the kinetic energy T of the protons into two components

$$T_\perp = T \sin^2 \theta, \tag{3.6}$$

$$T_{||} = T \cos^2 \theta. \tag{3.7}$$

As mentioned before, in case of adiabaticity, the value

$$\frac{p_\perp^2}{B} \propto \frac{T_\perp}{B} = \frac{T \sin^2 \theta}{B} \tag{3.8}$$

is a constant. This is true for every point of the trajectory as long as the motion remains adiabatic. Of particular interest are the point where the proton is generated (in the decay volume) and the analyzing plane, which

[3] To which the magnetic field lines are parallel in the analyzing plane

[4] θ is a function of the coordinate z: $\theta(z)$, as is the magnetic field $B(z)$. For the sake of readability, the dependence on z won't be written in the following equations

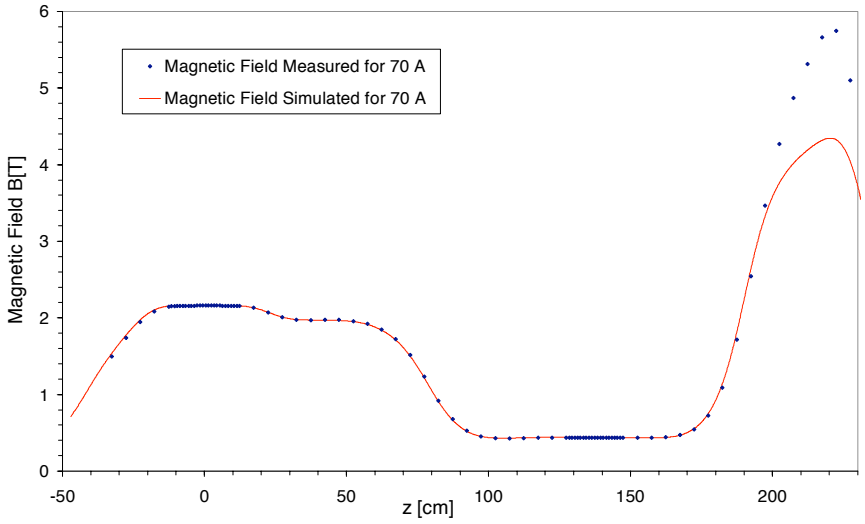

Figure 3.8: Simulated and measured magnetic field strengths along the z-axis of the spectrometer. The difference at high z-values comes from the fact that the Hall probe used for measuring the magnetic fields was not calibrated for fields strengths above 2.2 T citeFidel.

will be denoted with the indices 0 and A respectively. From (3.8), we see that

$$\sin^2(\theta) = \frac{B}{B_0}\frac{T_0}{T}\sin^2\theta_0 \tag{3.9}$$

which we can use to determine the energy component parallel to the z-axis:

$$T_{||} = T(1-\sin^2\theta) = T - \frac{B}{B_0}T_0\sin^2\theta_0 \tag{3.10}$$

Due to energy conservation, the total energy at any point along the z-axis is

$$E = T + V = T + e(U - U_0) \tag{3.11}$$

with the potential energy V and the electric potential U. Since the decay volume is kept at ground potential, $V_0 = 0$, we can substitute $E = T_0$ at any point. Thus, we can re-write (3.10) as

$$T_{||} = T_0 - e(U - U_0) - \frac{B}{B_0}T_0\sin^2\theta_0. \tag{3.12}$$

$T_{||}$ needs to be positive on each point of the trajectory for a proton to reach the detector. The field configuration has to be such that the minimum of the parallel energy is in the analyzing plane, to avoid reflections elsewhere in the spectrometer.

The minimum kinetic energy T_{tr} needed to overcome the potential barrier in the analyzing plane is given by the condition that the $T_{||,\mathrm{A}} = 0$

$$T_{\mathrm{tr}} = \frac{e(U_{\mathrm{A}} - U_0)}{1 - \frac{B_{\mathrm{A}}}{B_0}\sin^2\theta_0}. \tag{3.13}$$

Since this is a function of θ_0, the maximum and minimum values of T_{tr} are

$$T_{\mathrm{tr}}^{\mathrm{min}} = e(U - U_0), \quad T_{\mathrm{tr}}^{\mathrm{max}} = \frac{T_{\mathrm{tr}}^{\mathrm{min}}}{1 - \frac{B_{\mathrm{A}}}{B_0}}. \tag{3.14}$$

All protons with energies smaller than $T_{\mathrm{tr}}^{\mathrm{min}}$ will be reflected and all protons with energies greater than $T_{\mathrm{tr}}^{\mathrm{max}}$ will pass through the analyzing plane. For protons with initial energies $T_{\mathrm{tr}}^{\mathrm{min}} < T_0 T_{\mathrm{tr}}^{\mathrm{max}}$, we need to consider the ratio of the number of transmitted protons

$$\rho_{\mathrm{tr}}(T_0) = \int_0^{2\pi} \mathrm{d}\phi \int_0^{\theta_0^{\mathrm{max}}} \sin\theta_0 \mathrm{d}\theta_0 w(t) \tag{3.15}$$

and the total number of protons

$$\rho_{\mathrm{total}}(T_0) = \int_0^{2\pi} \mathrm{d}\phi \int_0^{\pi/2^{\mathrm{max}}} \sin\theta_0 \mathrm{d}\theta_0 w(t) \tag{3.16}$$

with θ_0^{max} being the maximum angle with which protons are still transmitted and $w(t)$ the proton recoil spectrum (as given for example in (2.38)). Since the proton spectrum has no angular dependence for an unpolarized neutron beam, the integrals become

$$\rho_{\mathrm{tr}}(T_0) = 2\pi w(T_0)(1 - \cos\theta_0^{\mathrm{max}}), \tag{3.17}$$

$$\rho_{\mathrm{total}}(T_0) = 2\pi w(T_0). \tag{3.18}$$

Since the transmission probability is given by the ratio of these numbers

$$\frac{\rho_{\mathrm{tr}}(T_0)}{\rho_{\mathrm{total}}(T_0)} = 1 - \cos\theta_0^{\max} \tag{3.19}$$

Using equations (3.13) and (3.14), we define the cosine function

$$c_{\mathrm{tr}}(T_0) = \cos\theta_0^{\max} = \sqrt{1 - \frac{B_0}{B_{\mathrm{A}}}\left(1 - \frac{T_{\mathrm{tr}}^{\min}}{T_0}\right)} \tag{3.20}$$

The complete transmission function $F_{\mathrm{tr}}(T_0)$ is then

$$F_{\mathrm{tr}}(T_0) = \begin{cases} 0, & \text{if} \quad T_0 \leq T_{\mathrm{tr}}^{\min} \\ 1 - c_{\mathrm{tr}}(T_0), & \text{if} \quad T_{\mathrm{tr}}^{\min} < T_0 < T_{\mathrm{tr}}^{\max} \\ 1, & \text{if} \quad T_0 \geq T_{\mathrm{tr}}^{\max} \end{cases} \tag{3.21}$$

giving the probability that a proton with kinetic energy T_0 will pass the analyzing plane.

4 The aSPECT DAQ

The Data-Acquisition (DAQ) in *a*SPECT consists of several parts: The proton detector, the read-out electronics, and the DAQ computers and slow-control. These subsets will be described in the following.

By far the central part of the DAQ is the proton detector. In *a*SPECT a Si-PIN diode detector manufactured by the Finnish company Detection Technology was used.

4.1 A short introduction to semiconductor diodes

In the following, a very short primer of semiconductor diodes and their application to the detection of ionising particles will be given. For more detail, I refer to textbooks such as [Kno99] and [Lut99].

4.1.1 Basic properties of semiconductor diodes

A semiconductor is a solid state body characterized by a small band gap (≈ 1 eV) between its valence and its conducting band, in contrast to conductors, where the bands overlap, and insulators, where the band gap is large (several eV). Due to this feature, its electrical conductivity can be controlled over a wide range, e.g. by adjusting the temperature or by introducing specific impurities into the crystal ("doping") and thus modifying the band gap.

If an electron is excited from the valence to the conduction band, this results in a so-called "hole" in the valence band. Both electron and hole are freely movable in the semiconductor, although their mobility will generally not be the same [Kno99, p. 357]. The energy needed for the generation of one such free charge carrier pair can come from different sources, e.g.

thermal excitation or the interaction of ionising radiation with the semiconductor. The latter case means that the electron-hole pairs can be used as a basis for detector response, and the amount of pairs produced is a measure of the energy deposited in the detector. This value depends on the deposited energy and the energy needed to create a charge carrier pair, which is about 3.6 eV for silicon[1].

For charged particles, which is the case of interest in aSPECT, the excitation of valence electrons results from momentum transfer of a passing charged particle to the electron shell of a lattice atom via COULOMB interaction. The maximum energy that can be transferred from a charged particle of mass M and energy E to an electron with mass m_e in one such process is $4E\frac{m_e}{M}$ or about $2 \cdot 10^{-3}\ E$ for protons. Hence, the charged particle will undergo many interactions, and the total energy loss is a statistical process. This results in a broadening of the initial energy distribution, called energy straggling [Kno99, p. 30 ff.].

The charge carriers generated by the mechanism described above will undergo a migration through the crystal which is a combination of random thermal movement and a net drift in the direction of an electric field, if present. While the drift velocities of electrons and holes are not the same in the general case, they are of the same order of magnitude[2]. For small detector sizes, the diffusion effect overlying the electric drift is usually negligible.

One of the most important aspects of semiconductor diode detectors is the the junction between negatively (n) and positively (p) doped areas of the semiconductor. Since the electron density on the n-side is much higher than on the p-side, there will be a net diffusion of electrons across the junction, and they will recombine quickly with holes on the p-side. As a result of this, there will be immobile positive charges on the n side in the form of ionized donor atoms[3]. Similarly, the migration of holes from the p- to the n-side leaves behind negatively charged acceptor atoms. The resulting space charge gives rise to an electric field which reduces the tendency for further diffusion. At equilibrium, the field is just strong

[1] The band gap of silicon is only 1.12 eV, however just a part of the interactions results in electron-hole pairs; the remainder generates phonons.

[2] As opposed to the mobility of ions and electrons in gases, for example.

[3] The atoms used to dope an n-type semiconductor are usually called *donors*, while the ones used to dope a p-type semiconductor are referred to as *acceptors*.

enough to prevent additional diffusion across the junction. The region across which the charge imbalance exists is called *depletion region*.

The inherent characteristics of the depletion region already allow it to function as a detector. The abundance of both electrons and holes in the area is very low and any charge carriers generated by ionising radiation at or near the junction are swept out of the region by the electric field, their movement constituting a basic electric signal.

However, semiconductor diodes without external electric fields have poor characteristics. The magnitude of the internal electric field is too small to ensure fast movement of the charge carriers, which can result in loss of charges due to trapping or recombination. In addition, the thickness of the depletion region and as such the area where charges are generated is small.

For these reasons, the diodes are usually operated in *reverse bias mode*[4], where a negative potential is applied to the p-side of the diode. This enhances the natural potential difference between the two sides, both increasing the depletion region and the drift speed of the charge carriers.

The amount of material an ionising particle has to pass through to reach the depletion region is called the *dead layer* of the detector, since the charge carriers generated there do not contribute to the detector signal. The dead layer consists of any material used to coat the detector (e.g. for surface protection) and the part of the n- or p-layer which is not depleted.

4.1.2 Energy loss and penetration depth of charged particles

The energy deposited by a charged particle in the detector material is given by the particle's *specific energy loss* $-\mathrm{d}E/\mathrm{d}x$, for which the classical expression is the Bethe-Bloch formula

$$-\frac{\mathrm{d}E}{\mathrm{d}x} = \frac{4\pi e^4 z^2}{m_0 v^2} NZB. \tag{4.1}$$

In this expression, v and z are the velocity and charge number of the incoming charged particle, respectively, N and Z are the number density and atomic number of the detector material, m_0 is the rest electron mass and

[4] In the opposite case of operating the diode in *forward bias mode*, conductivity through the junction is greatly enhanced.

e is the electronic charge. B is a more complicated expression depending on the particle's energy and properties of the absorber material (namely its mean excitation and ionisation energies). From integration of (4.1), one can determine the penetration depth of a charged particle into the detector. For low energy protons, as we are dealing with in *a*SPECT, this depth is less than one μm. Hence, it is important that the dead layer of the detector is small compared to that value, otherwise there will not be enough electron-hole pairs generated in the depletion region to obtain a detectable signal.

Likewise, the depleted region of the detector should be as large as possible to ensure that all of the generated charge carriers contribute to the detector signal. The *p*-*i*-*n* configuration of a semiconductor diode has several favourable characteristics. By introducing an intrinsic[5] in between the *n*- and *p*- doped layers, a region with very high resistance and low free charge carrier density. Usually the doped layers are small in comparison to the intrinsic layer, and the detector becomes fully depleted already at low bias voltages.

4.2 The aSPECT detector

4.2.1 General properties of the detector

The detector used in *a*SPECT is a custom array based on the XRA-series diodes [dee, Juo02]. It has an active area of 25.8×25.95 mm^2 divided into 25 segments with an active area of each cell of 0.8×25 mm^2. A picture of the general layout of the detector is shown in Fig. 4.1 and a photograph of it in Fig. 4.2.

The strips visible on the figures are on the side of the detector facing the proton beam. They are *p*-doped. The contacts for each strip consist of aluminum. The depth profile of the detector starting at the *p*-doped side is the following [Juo02]:

- A protective entrance window of total thickness 670 Å consisting of
  - 400 Å of Si_3N_4

[5] In practice, it is nearly impossible to create a purely intrinsic semiconductor, as such very weakly doped material is used for this.

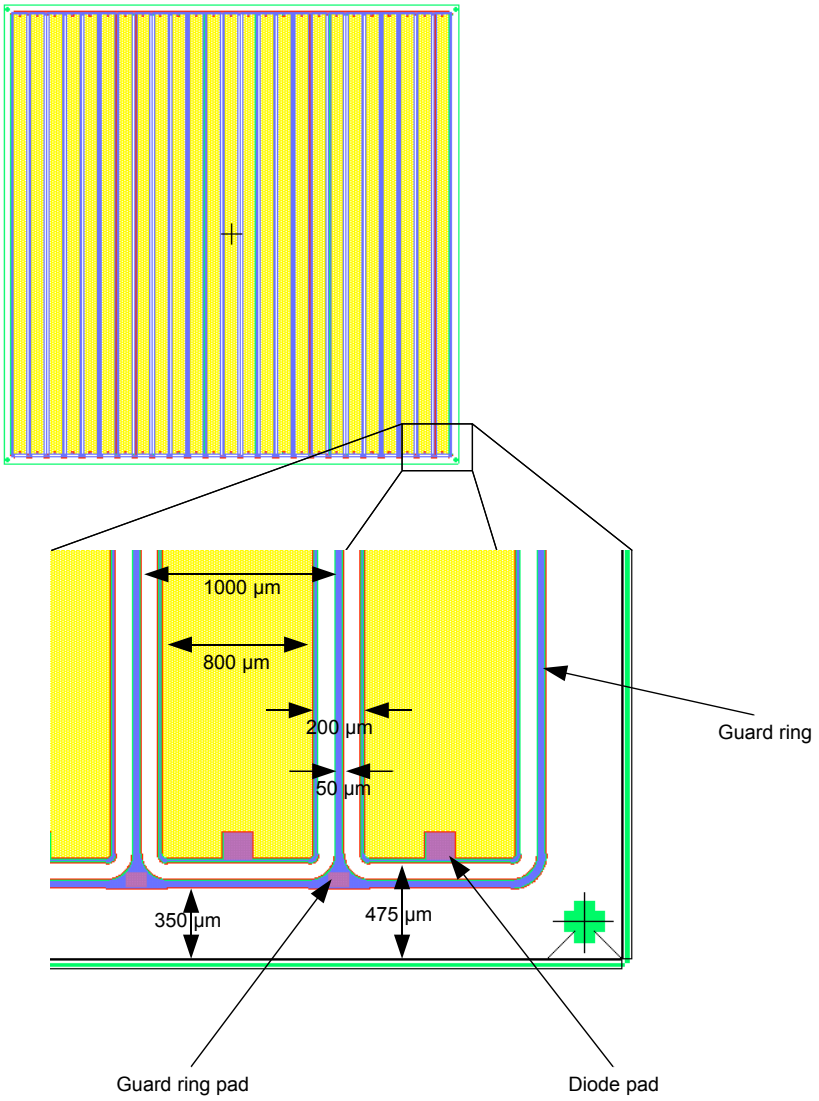

Figure 4.1: Schematic of the detector layout (from [Juo02]).

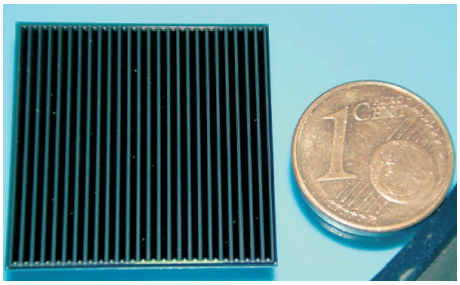

Figure 4.2: A photograph of the *a*SPECT detector, with a 1 Cent coin for size comparison.

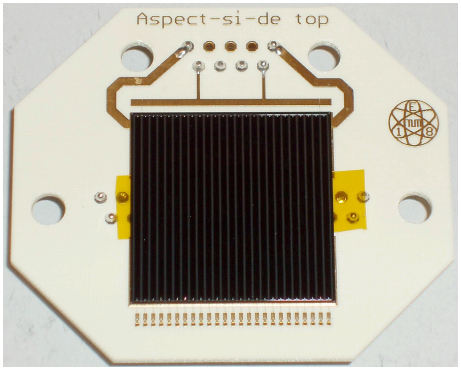

Figure 4.3: The *a*SPECT detector mounted on the PCB.

  - 270 Å of SiO_2

- a p-doped layer of 0.5 μm thickness
- an intrinsic layer of low n-doped silicon with a thickness of 380 μm
- an n-doped layer of 0.5 μm thickness
- a 0.5 μm thick layer of aluminum

Both the n-doped and aluminum layer are common to all strips.

The detector was glued to a specially designed printed circuit board (PCB) which was made from a special plastic (RO2350™ produced by Rogers Corporation) with the circuit imprinted in gold to make the board suitable for ultra-high vacuum (UHV). A conducting UHV glue of the type UHVGLUE-H27D from the company CABURN was used for the same reason. A picture of the detector mounted on the board can be seen in Fig. 4.3.

All strips are separately bonded and each bond is led to a *vertical interconnect access* (VIA) which consists of a gold plated hole into which a single pin fitting into a standard SUB-D connector is pressed and soldered. The VIAs are visible in Fig. 4.3 behind the detector, under a Kapton foil, which is used to insulate the backside for the detector from the VIAs. Since we need to read out all 25 channels and also provide the bias voltage, one single standard 25 pin connector is not enough. For this reason, there is

another 9 pin connector near the top of the PCB. This connector is also used to lead the signals from a PT-100 temperature sensor mounted on the back of the PCB to the read-out electronics.

4.2.2 Mechanical setup of the detector inside aSPECT

As can be seen in Fig. 3.1 and Fig. 3.3, the detector is placed inside the cold bore of *a*SPECT in a high magnetic field. Since the detector is also placed on a high voltage, occasional breakthroughs and resulting damage to the detector or electronics can't be completely avoided. For this reason, it has to be accessible for maintenance during beam times. Since the process of warming up and cooling down the cryostat takes approximately two weeks, it is not a feasible option to install the detector in a fixed way inside the spectrometer.

For this reason, a mechanics was built that allows the detector to be retracted towards the top of *a*SPECT behind a UHV gate valve. This setup can be seen in Fig. 4.4. The part marked with "Detector" on the drawing consists of a CF-63 flange containing two SUB-D UHV feed-throughs. These are spaced as to fit the connectors on the detector PCB, which is plugged into the connectors. The detector is shielded by a lead-filled stainless steel cup (not visible in Fig. 4.4).

The flange is fixed to a stainless steel tube, which contains the preamplifier board (see section 4.3.1). This board is plugged into the side of the flange opposite of the detector. This way, we mount the first amplification stage very close to the detector, which helps to reduce pick-up noise. The entire electronics as well as the tube is put on high voltage together with the detector. It is isolated from the rest of the setup (and the spectrometer) by a CF-35 ceramic insulator. A membrane bellows is connected to the other side of the insulator. It separates the inner steel tube, which is on atmospheric pressure, from the UHV inside the spectrometer, and it also makes the movement of the lower part possible.

The digital part of the electronics is too large and generates too much excess heat to be put inside the cryostat and is mounted on top of the setup as a consequence. The cables which connect the two part of the electronics are contained in a Plexiglas tube inside the central stainless steel tube, to shield the high voltage. In the same Plexiglas tube, a plastic hose leads from the top of the setup to the preamplifier. It is used to blow compressed

air across the electronics when it is inside the cryostat. The purpose of that is two-fold: If the electronics are running, it cools the preamplifier board, while it prevents condensation of moisture (and possible resulting short-circuits) on the board and the insulator when the electronics are switched off. The latter is necessary since the surrounding cold bore is roughly at liquid nitrogen temperature.

The entire setup is contained in two T-shaped CF-160 vacuum pieces. At the upper side access, a turbo-molecular pump is attached which is used to evacuate the setup after it has been attached to the spectrometer. A vacuum sensor is attached to the lower side access.

The setup can be moved vertically by means of a gear drive which is mounted on the outside of the T-pieces and connected to the central stainless steel tube. The membrane bellows allows for a total movement distance of about 70 cm, which is enough to withdraw the detector from its measurement position (see Fig. 3.3) behind the UHV gate valve. If the detector is in this retracted position, closing the valve will separate the vacuum inside the setup from the main vacuum of the spectrometer and the setup can be aired and detached from *a*SPECT.

4.2.3 Detector characteristics

Several properties of the detector were measured and a concise description of these measurements is given in Ref. [Sim06]. The following is a list of the most important features.

Energy loss in the entrance window

Simulations with the program SRIM 2006 [Zie07] indicated that 30 keV protons lose approximately 8 keV in the entrance window of the detector, resulting in a proton peak centred at 22.8 keV. However, calibration measurements with several gamma ray sources as well as measurements done at the proton source PAFF [Mül07] indicate that the peak is actually centered around 24 keV instead. The reason for this discrepancy is not fully understood yet, but a possible reason is that the entrance window is actually somewhat thinner than the company stated.

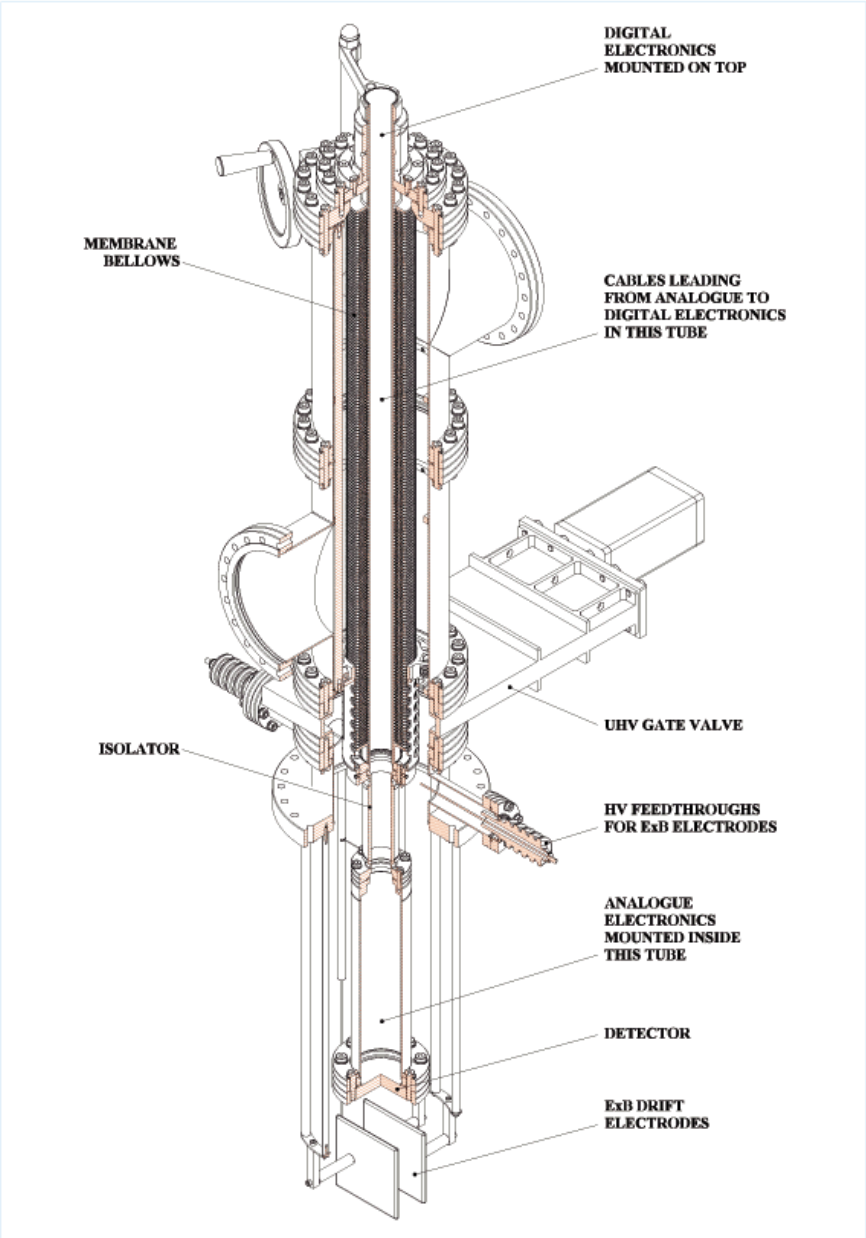

Figure 4.4: A drawing of the mechanics used to fix the detector inside *a*SPECT.

Energy dependence of detector efficiency

A possible false effect in a could result from an energy dependent detection efficiency of our detector. Unfortunately, it is not possible to generate a test beam that is stable enough to study these effects to the required precision. It is possible to do some simulations and calculations, however.

Simulations with SRIM-2006 indicate that the chance to detect a proton with initial energy of 30 keV is lower by about $3 \cdot 10^{-4}$ than the chance to detect a proton with 30.8 keV energy [Sim07a].

A possible effect due to energy dependant backscattering on the detector was investigated by means of a semi-analytical calculation of the backscattering probability. This was done by subdividing the detector into thin slices and evaluating a modified RUTHERFORD cross section after each slice. For each slice, a critical angle was calculated which would result in the proton not being detected. This procedure was repeated up to a maximum depth inside the detector, which was defined as the depth where a particle would not deposit enough energy to be detected when scattered back by 180°. The energy loss through each layer was interpolated from data obtained from SRIM.

The resulting difference in backscattering probability between 30 and 30.8 keV was roughly $8 \cdot 10^{-5}$, or $\approx 10^{-7}\text{eV}^{-1}$, well below the value given above. However, it has to be stated that these value only are average backscattering probabilities, since there's no true account for the statistical nature of single interaction processes; the energy loss and the evaluation yield only mean values.

The calculations were done with the help of a C++ program using the ROOT libraries [roo07].

Diode characteristics

Several measurements of the diode characteristics have been made [Sim06]. We could show that the capacitance of one detector strip is about 13 nF and as such very close to the manufacturer quoted value of 12 nF.

The detector is already fully depleted at a bias voltage of about -57 V, which is what was used in all measurements.

4.3 The read-out electronics

The read-out electronics was built at E18 and is based in a large part on read-out electronics developed for the COMPASS experiment at CERN.

4.3.1 The preamplifier board

As mentioned before, the PCB containing the preamplifier stage of the electronics is plugged into the opposite side of the detector flange. A picture of the board can be seen in Fig. 4.5.

The key feature of the board are the two preamplifier chips of the type CG16In-16Out on the front and back side of the board. They are modifications of the GASSIPLEX chip which is used in COMPASS [Bau03], the main difference being the removal of the multiplexer element of the chip, which isn't useful for *a*SPECT since we do not use an external trigger. Each of the chips can process 16 input channels at the same time.

Also present on the board are shaper and line driver chips. The latter are required to transfer the signals via twisted-pair cables to the digital part of the electronics, which is about 2 m distant. The driver chips are located underneath the heat sink visible in Fig. 4.5. The peaking time of the preamplifier is fixed at 400 ns. The expected noise performance as stated by the developer was 400 e^-, corresponding to about 1.4 keV for silicon. However, in practice, the noise performance was worse than that by about a factor of 2 (see also 5.3.1 for implications of the higher noise). The reasons for this discrepancy are not fully understood as of yet.

Also situated on the premplifier board is another PT-100 temperature sensor; it is situated beneath the heat sink as well.

4.3.2 The digital electronics

The SADC board

The signals from the preamplifier are continuously digitized by 32 analog-to-digital converters (ADC) with a resolution of 12 bit, which are mounted on a PCB (referred to as "SADC board") as can be seen in Fig. 4.6. The sampling frequency of the ADCs is 20 MHz, and this was adopted as clock

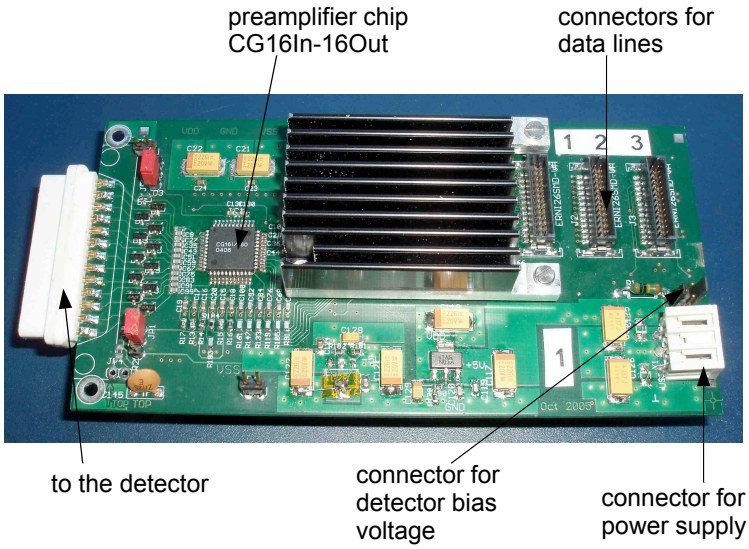

Figure 4.5: The preamplifier board of *a*SPECT.

cycle for all operations on the SADC board. The board was developed at E18 and is described in detail in Ref. [Man06].

Of the 32 channels, 25 are used to process the detector channels, and two are connected to the temperature sensors. The rest of the ADCs are not used.

The second important feature of the SADC board are two Xilinx Virtex-II 1000 field programmable gate arrays (FPGA) which are directly connected to the ADC outputs and provide the data buffering and processing for 16 channels each. Since *a*SPECT has no external trigger, the pulse detection[6] is done at this stage.

In the FPGA, the data from each channel are stored in a FIFO buffer which can store a total of 1024 data words[7]. Depending on the event length that is set, this means that between 7 and 12 events can be cached in the buffer. A multiplexer running with the same clock as the ADCs pulls events

[6] I.e. the decision whether an event is discarded or passed along the DAQ chain.

[7] The length of one word in this context is the length of one data word from the ADC, i.e. 12 bits.

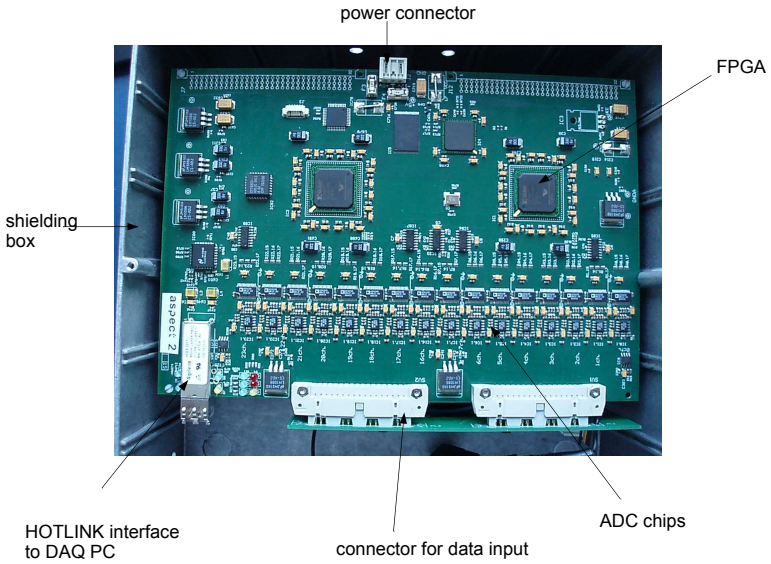

Figure 4.6: The SADC board containing the digital electronics of *a*SPECT.

from each channel in turn. The time required to cycle through all channels is maximal if each channel has data waiting to be processed, and again depends on the event length. With an event length of 80 samples[8], every channel would take 4 μs to process, and it would take roughly 50 μs for one cycle. This means that as long as the data rate per channel is less than 20 kHz per channel, no event will be lost. Since the expected data rate for *a*SPECT was in the order of 1-2 kHz for all channels[9], the only source of dead time is the pulse detection, which is discussed in the following.

The pulse detection is done for all 16 channels with an algorithm which is illustrated in Fig. 4.7. The FPGA maintains average values of two "windows" internally, a long one[10] which defines the baseline of the ADC channel, and a short one which is used to define when an event is written out. The ADC data is shifted continuously through a shift register and discarded

[8] See section for details on the event structure.
[9] This includes both protons and electrons from the neutron decay.
[10] The length of this window is much more than the defined event length.

at the end if no pulse was detected. The average values of the windows are constantly updated during this procedure. When the difference between the two average values is bigger than a defined threshold value for a defined number (the so called *delay*) in a row, a pulse is detected. In this case, the ADC values in the shift register are put into the FIFO for read out. To obtain the full pulse, a certain amount of ADC values before the pulse was detected is written out as well (the so-called *buffer*). Additionally, a timestamp is added to the event. Once a pulse has been detected, no more triggering is done in the time interval of this event. This means that the earliest time another trigger can be detected in this channel is exactly the length of one event, which is about 4 μs for an event length of 80 ADC samples.

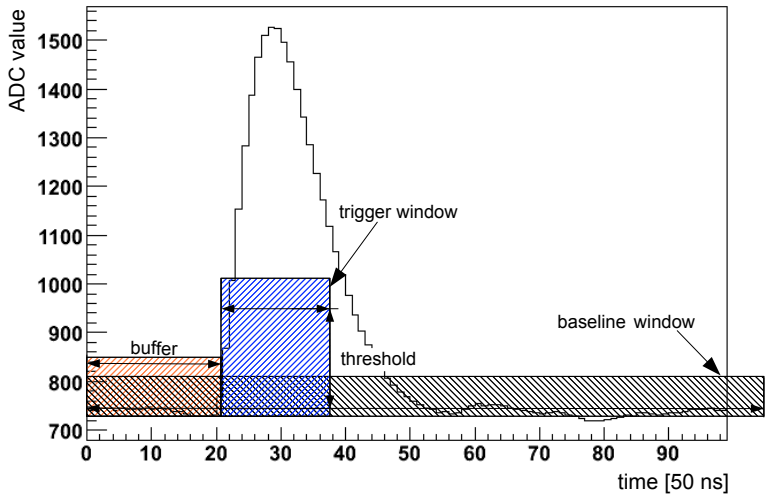

Figure 4.7: Illustration of the trigger algorithm used for pulse detection. For details, see the text.

All parameters of the described algorithm are adjustable. The window sizes can be set in powers of 2, while buffer size, delay, threshold and event length are adjustable more freely. To change parameters, it is not necessary to access the board directly, but it can be done by programming them from the read-out computer, since the communication is bi-directional.

We decided to use this algorithm after trying out several others because it allows flexibility while being relatively easy to implement for 16 channels in the FPGAs. An advantage over a simple "over threshold" trigger is e.g. that it is possible to filter out high pulses with have a much shorter timing than pulses which come from the detector.

In addition to the pulse detection, the SADC board can be programmed to send out data in regular intervals. These *heartbeat* events are used to write out data from the temperature sensors as well as events from the detector channels without triggering (e.g. for noise estimates).

After an event has been polled from the FIFO buffer, the FPGA attaches headers containing information about the channel it was detected in and control words. It is subsequently sent out via a HOTLINK interface and optical cables to a PCI card in the DAQ computer.

The SADC board is put on the same high voltage as the preamplifier board. It is decoupled from the later stages by the optical cables just mentioned. To prevent discharges, the board is mounted inside a metal box (with openings for air circulation) which in turn is installed into a larger Plexiglas box to isolate it. This setup can be seen in Fig. 5.1, which shows the electronics mounted on the spectrometer.

The interface card

The PCI card receiving the data from the SADC board is based on a similar read-out card developed for COMPASS detectors described in [Gru06, p. 30 ff.] and it can be seen in Fig. 4.8. The main difference between the card described there and ours is the *mezzanine* card which is plugged into the actual PCI card (the *mother card*). In the case of COMPASS, a S-LINK interface is used, in our case a HOTLINK. The reason for this is that in COMPASS an additional DAQ stage is situated between the ADC and the read-out PC, the so-called GESSICA, a multiplexer module. S-LINK is the standard communication interface to this module, while HOTLINK is the standard interface to the SADC board. Since *a*SPECT does not need the GESSICA module, the HOTLINK interface is directly located on the PCI card of the read-out PC. Data is passed from the mezzanine card to a FPGA on the host card which then writes it to a standard 512 MB SDRAM memory buffer.

This buffer can be accessed from the computer via the PCI bus. Existing

drivers for Linux provided by CERN, the so-called *autobahn* or *ab* divers were used for this.

4.3.3 Data structure

After passing through the electronics, one event has a defined structure, as shown in table 4.1. For later analysis, only the first SLINK header and

SLINK header 1 (32)			
SLINK header 2 (32)			
SLINK header 3 (32)			
ADC header (32)			
1	0	timestamp (30)	
unused (8)	ADC data (12)	ADC data (12)	
⋮			
⋮			
unused (8)	ADC data (12)	ADC data (12)	
footer (32)			

Table 4.1: Structure of one event. The number of bits for each block is given in parentheses.

the ADC header are important, since they contain information about the event length, event type and channel. The exact structure of these headers can be seen in table 4.2.

Blocks labeled "zero" do not contain relevant information. The bit labeled "h" is the heartbeat bit, which is 1 for heartbeat events and 0 for events which were detected with the trigger algorithm. To distinguish between heartbeat events from the temperature sensors and the detector channels, the bit labelled "s", the *slow-control* bit, is used.

The bit labeled "o" is the *overflow* bit. It is set in case the FIFO mentioned earlier is full and the event can't be buffered anymore. In this case, only the time stamp is recorded and sent out. This can act as a warning signal that events may be lost.

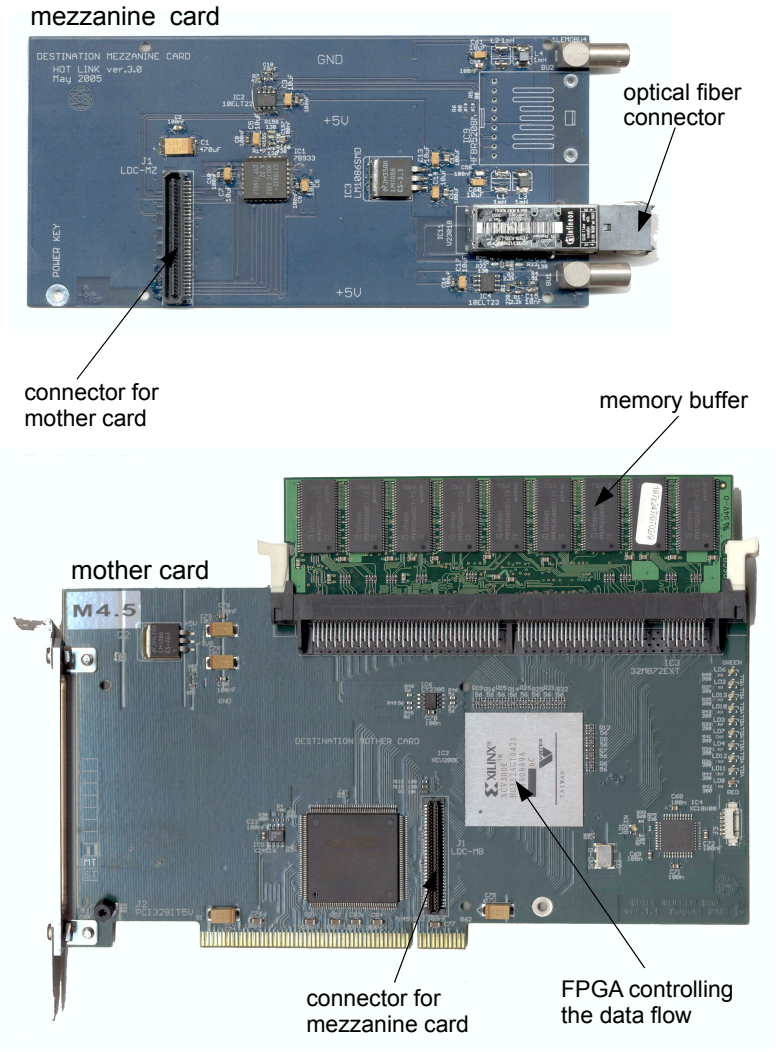

Figure 4.8: The interface card used to receive data from the SADC board.

1	type (5)	id (10)	size (16)
⋮			

1	zero (4)	h	s	o	zero (3)	channel (5)	zero (4)	size (12)

Table 4.2: Structure of SLINK header 1 (top) and the ADC header (bottom).

4.3.4 The DAQ setup

A diagram of the data flow in the experiment can be seen in Fig. 4.9. Two separate computers, the *read-out PC* and the *slow-control PC* are used in the experiment. The read-out PC was a commercially available computer running with the E18 Linux distribution[11] and containing the PCI card described above. The slow-contol PC was a dual-processor computer running Windows XP™ and containing several National Instruments™ interface cards, namely a GPIB card and a counter card .

The individual components of the DAQ system are described in the following.

The read-out software

The data stored in the memory buffer is read out with a C-program and a LabVIEW™ graphical user interface (GUI). A screenshot of this program can be seen in Fig. 4.10. The C-program interfaces with the PCI card via the ab driver mentioned earlier. Once a measurement is started, all data from the card is written to a raw file, where each event is stored in the structure described in table 4.1. The GUI does not interfere with the datastream, but decodes selected events in parallel and can display the event shape in the right window visible in Fig. 4.10. This allows us to check the pulse shape of the events online.

The left window is used to display the number of events per channel, which is useful both for getting an impression of the proton beam's position on the detector online and for being able to spot channels with bigger noise than the rest and adjusting the trigger conditions for these channels

[11] A modified Debian distribution.

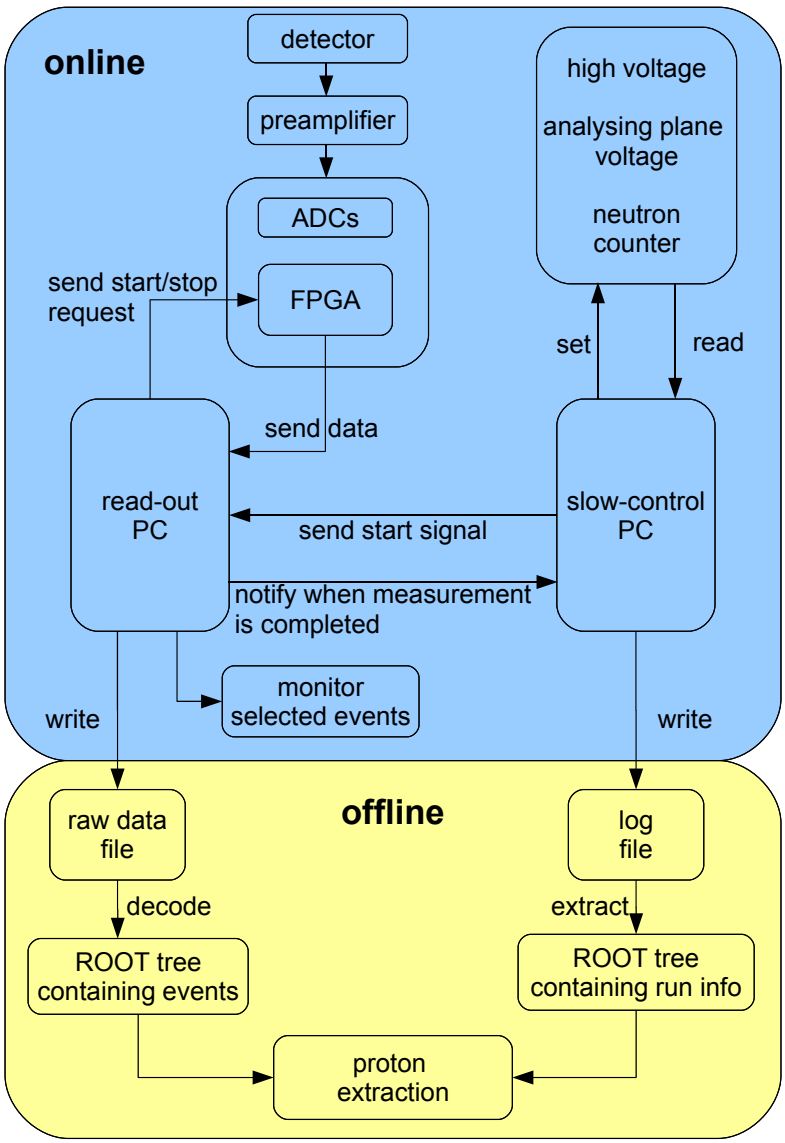

Figure 4.9: The data flow in *a*SPECT (schematic).

accordingly. The trigger parameters can be set and sent to the SADC

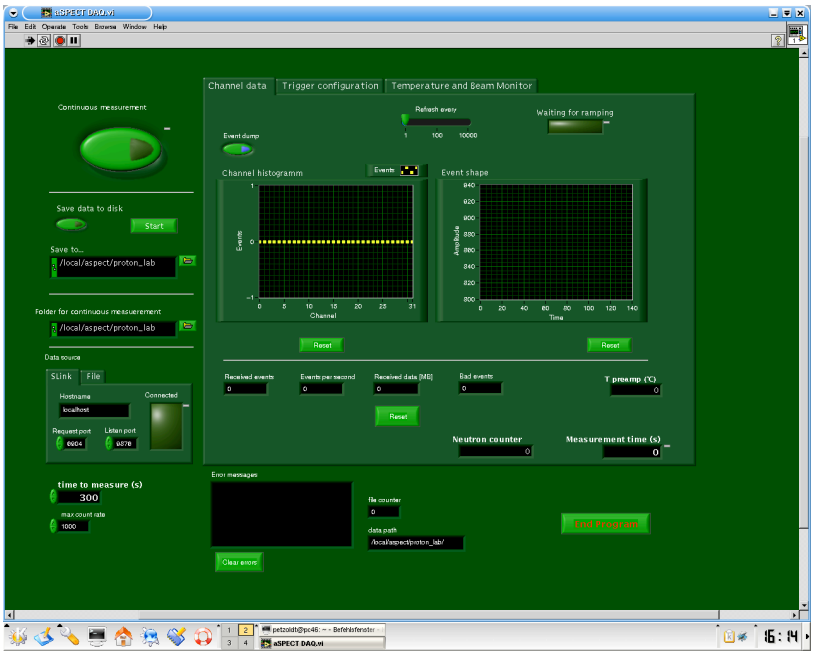

Figure 4.10: The LabVIEW™ graphical user interface for the read-out software.

board from the second tab of the GUI. The destination file for the raw data can be set manually when controlling the GUI directly; in case of a measurement cycle, the destination folder has to be set and the data files are named "⟨measurement number⟩.dat" automatically.

The program is written in a way that allows it to be remotely controlled via the DataSocket™ interface[12] from another computer, on which the slow control software is running. That way, we can setup a defined sequence of measurements with different analysing plane voltages on the slow control computer and then conduct these measurements automatically at the push of a button.

[12] DataSocket™ is LabVIEW™'s interface to networking mechanisms and is a comfortable way to setup communication between LabVIEW™ programs.

The slow control

The software for reading out and controlling consists of several independent LabVIEW™ programs which exchange their data via a DataSocket™ server application running on the same computer. This server also manages the data exchange between the read-out and the slow-contol computer. A screenshot of the different applications can be seen in Fig. 4.11, showing the high voltage control, the analysing plane voltage control and the program to set and start measurement cycles. The analysing plane voltage

Figure 4.11: The LabVIEW™ applications for slow-control.

is provided by a voltage supply of the type HCNO.8M-800 manufactured by the company FUG, which was enhanced for a high stability. It can be controlled via an in-built GPIB interface; the voltage is monitored by an Agilent 3458 multimeter[13] which is also read-out via GPIB. The controlling program sends the command to set a voltage to the power supply, waits for the measurement value from the multimeter and performs fine corrections if needed.

[13]This version was specified to have a more precise reference than the standard version.

The high voltage is supplied by a power supply of the type HCN 35-335000, also built by FUG. This supply does not have an internal GPIB interface, but is instead controlled via a USB-to-Analog (or *UTA*) device manufactured by the company E&A, who also provided the necessary LabVIEW™ drivers. A second supply of the same type was used to provide the high voltage for the upper ExB electrode.

The program used to set up measurement cycles and start the measurement process also polls data from the monitoring programs and writes the gathered information to a logfile, which then contains the filename of the raw data, the measurement time, the analysing plane voltage, the high voltage and the total amount of neutron counts, which is provided by a neutron counter connected to the counter card in the slow-control PC, for each measurement in one line.

5 Measurements and data analysis

Between summer 2005 and May 2006, the spectrometer *a*SPECT was set up at the MEPHISTO beamline of the Forschungsneutronenquelle Heinz Maier-Leibnitz (FRM-II) in Munich for a total of four beamtimes. In the following section, an overview of the activities during these beamtimes will be given and a first analysis and discussion of the data taken will be presented, with a focus on different methods to extract the proton count rates from the raw data and the effect on the value of a. The total size of raw data taken during the entire time is roughly 350 GB.

5.1 Setup of the experiment at the MEPHISTO beamline

Fig. 5.1 shows *a*SPECT as it was installed at the MEPHISTO beamline. The spectrometer was attached to the neutron guide NL3a of the reactor via two CF 200 bellows with a 65 cm long CF 200 vacuum tube inserted in between those. This setup allowed for alignment correction of the spectrometer in case of a mismatch of the spectrometer's beam axis with the exit of the neutron guide. Inside the vacuum tube, two apertures were installed for a rough collimation of the neutron beam. They each consisted of several layers of borated plastic glued onto two semicircular lead pieces with a thickness of 50 mm. Tubes of boron-silicate glass were inserted into the tube to provide biological shielding. Fine collimation of the beam was done inside the spectrometer with six apertures made from lithium fluoride. Three of those were installed both at the entrance and at the exit of the spectrometer.

A similar setup was used at the exit of the spectrometer to connect it to

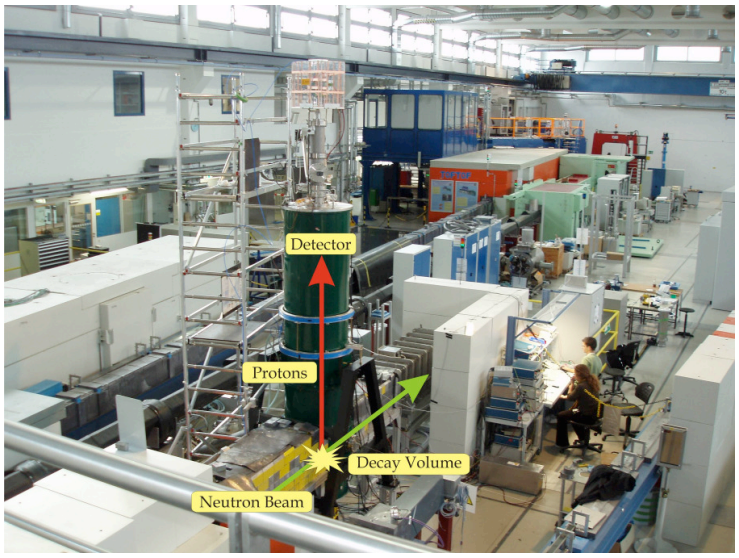

Figure 5.1: The spectrometer *a*SPECT as it was set up at the MEPHISTO beamline of the FRM-II. Photograph courtesy of M. Simson.

the beam dump, which consisted of a vacuum tank shielded with layers of borated plastic and lead and located downstream of the spectrometer. To monitor possible beam fluctuations, a neutron counter was installed at the back of the beam dump. Both the entrance and exit tubes were surrounded by roughly 5 cm of borated plastic and 5 to 10 cm lead; the outer layer of the shielding is visible in Fig. 5.1.

The two blue coils mounted on *a*SPECT are (non-superconducting) correction coils for the magnetic field[1]. The analyzing plane is located roughly in the middle of the two coils. The necessity of mounting the coils became evident after the first beamtime to achieve the desired field configuration inside the spectrometer.

On top of the spectrometer, the mechanics for insertion and retraction of the detector as described in section 4.2.2 can be seen. The digital part of the readout electronics was placed inside a metal box which in turn was placed inside a box made from plexiglass. This was necessary to provide shielding for the high voltage on which the detecor and the electronics

[1]The visible part are the water hoses which were necessary for cooling of the coils.

were put. The visible copper strips were added to keep the electric field homogeneous and prevent electrostatic charging of the outer box.

The electronics was powered by an external generator providing +12 V, which was converted to the necessary ± 5 V with DC/DC converters mounted on top. The ground of this generator was the negative high voltage. A more detailed description of the setup of the spectrometer during the beam times can be found in Ref. [Sim06].

A major problem during the first beamtimes were repeated HV breakthroughs which damaged the readout electronics. Consequently, a lot of the time during and in between these beamtimes was spent for improving the HV insulation and better shielding against breakthroughs, and only little actual data was taken. While this situation did improve in the last beamtimes, due to better shielding, HV breakthroughs still occured sporadically and posed a serious obstacle to routine measurements. Nevertheless, a significant amount of data could be taken in the last two beamtimes.

5.2 Data taking

5.2.1 Measurement process

To determine the value of a, measurements at different analyzing plane voltages have to be performed. In the actual measuring process, the analyzing plane voltage was changed every five minutes and a new measurement was started. The main reason for this procedure is to suppress effects which might be introduced by a slow drift of the barrier voltage or of other external parameters. A comparatively short measuring time ensures that over one measurement, the external conditions stay the same. One measuring cycle would typically consist of several hundred individual measurements at several different analyzing plane voltages.

5.2.2 Activities during the beamtimes

Beamtimes 1 and 2

*a*SPECT replaced the experiment RASPAD[2] on the MEPHISTO beamline in July 2005 during the third reactor cycle of that year. Most of this beamtime was spent with setting up the spectrometer and necessary shielding. After the shielding requirements were met and we were approved by radiation protection to begin measuring, it became apparent that there were problems with the powering of the electronics. The initial concept was to convert the 12 V provided by the battery to ± 5 V close to the generator and connect this voltage to the electronics via high voltage cables. The voltage drop over the length of these cables (roughly 3 m) proved to be so large that the electronics wasn't operating stably. Hence the wiring had to be changed and the DC/DC converters had to be moved to the top next to the digital electronics. These problems resulted in very little data being taken during this beamtime.

In the break between the third and fourth reactor cycle, the necessary improvements to the the wiring and the voltage supply of the electronics were made. In addition, the magnetic field inside *a*SPECT at the beamline was measured[3]. For this procedure, a dewar has to be inserted into the spectrometer [AG05], which due to the height of *a*SPECT and the operating height of the neutron guide hall crane was only possible by turning the spectrometer by 90 degrees and inserting the dewar horizontally. This required the dismantling of the radiation shielding and disconnecting the spectrometer from the neutron guide. The re-setting up of *a*SPECT and the radiation shielding following the magnetic field measurements and the subsequent cooling down of the cryostat lasted well into the next beamtime.

In November 2005, some data was taken, before the spectrometer was warmed up for installation of the upper ExB drift electrodes which up until this point had been missing. The effect of the electrodes on the proton count rate has already been shown in Fig. 3.7.

The total process of warming up, installing the electrodes and cooling down again took about two weeks' time. From the middle of December

[2] An experiment on radiative beta decay.

[3] Before, it had only been measured at the TRIGA reactor in Mainz, where the spectrometer was assembled.

until the end of the beamtime, data was taken.

Beamtime 3

The third beamtime beginning in January 2006 was initially spent performing high voltage tests, since the problems with sporadic breakthroughs persisted. Since a breakthrough often required exchange of the preamplifier electronics which in turn meant the dismounting of the entire detector mechanics as well, these tests were very time intensive[4]. At the same time, the DAQ software was being enhanced and adapted to monitor and control the various voltages automatically, specifically with regard to reducing the possibility of breakthroughs. Additionally, more automatization was implemented in the entire data acquisition procedure. This allowed more extended measurements with little need for manual control of the parameters.

Beamtime 4

The last beamtime was used to check a lot of systematics, like the influence of the upper and lower ExB drift electrode voltages on the proton beam position and a more in detail study of the dependence of the trigger parameters on the spectrum shapes. A more comprehensive coupling of the neutron monitor to the rest of the DAQ software was implemented as well, allowing a better documentation of possible neutron beam fluctuations over one measuring cycle.

5.3 Data analysis - extraction of a

To extract the actual value of a from the raw data, a series of processing steps is necessary:

- The raw data needs to be decoded into a processable format.

[4] A complete exchange of the detector mechanics includes powering down of the turbo molecular pumps, extraction of the detector from the cryostat, detaching of the mechanics from the spectrometer, lifting the mechanics down from the top of *a*SPECT to the floor with the neutron guide hall crane, exchange of the electronics, lifting the mechanics back to the top, re-attaching it and a lengthy evacuation time to reach a vacuum comparable to the one inside the cryostat.

- An event-by-event analysis of the pulses and extraction of the pulse-height information has to be done.
- From the resulting pulseheight spectrum, the number of protons must be extracted, including background subtraction.
- Doing this for multiple analyzing plane voltages yields an integral proton count spectrum, which can be fitted with the theoretical function and a as fit parameter.

Most of the software used for this analysis process was written from scratch and uses the ROOT framework and libraries unless stated differently.

5.3.1 Decoding of the raw data

The data format of one event has already been described in section 4.3.3. For one measurement, the raw data is completely dumped into a single file, which then contains all events taken in that measurement. To further process the data, a dedicated program was written[5] which extracts for each event the timestamp, absolute time, channel number, maximum ADC value, baseline value, and an array containing all ADC values for that given event (see Fig. 4.9). That information is stored into a ROOT tree with corresponding branches for later retrieval and analysis.

Since the timestamp for each event is comprised of 30 bit and one bit corresponds to 50 ns (one cycle of the ADC clock running at 20 MHz, see section 4.3.3), an overflow of the timestamp occurs every 53.7 seconds. To extract the absolute time for each event[6], it is therefore necessary to take the possible overflow into account when decoding. In addition, due to the multiplexing nature in which the data is sent out by the digital electronics, it may happen that an event from one channel with slightly higher timestamp is written to disk before an event from a different channel with slightly lower timestamp. To prevent this, data blocks of a set number of events are first stored internally in memory and sorted if necessary before they are written to the ROOT file. This output file then contains the ROOT tree with the above mentioned information for each event.

[5] Based on a program originally written by L. Schmitt for the readout of COMPASS.
[6] Absolute in relation to the start of the measurement.

5.3.2 Analysis of events and extraction of the pulseheight spectra

A typical proton event is shown in Fig. 5.2. Since the information about

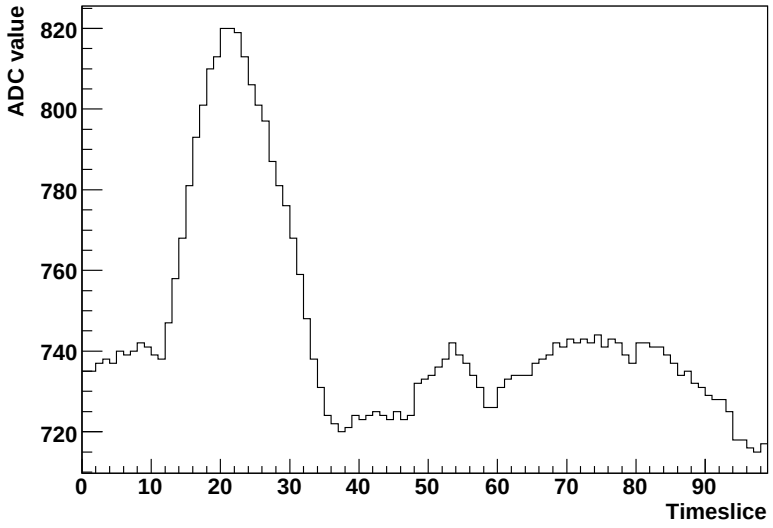

Figure 5.2: A typical proton event. The baseline value of the ADC channel is ≈720. One timeslice corresponds to 50 ns.

the corresponding energy of the event is contained in the height of the pulse, the energy spectrum of a measurement is obtained by filling a histogram with the pulseheights of all events in the measurement. The most straightforward way to extract the pulseheight information is to simply take the maximum of the pulseshape histogram and subtract from it the baseline value of the channel in which the event was recorded. The latter value can also be extracted from each event separately by taking the mean value of the last 20-40 channels of the pulseshape histogram. A typical pulseheight spectrum obtained in this way can be seen in Fig. 5.3.

One thing which is immediately noticeable is that the separation of the proton peak and the electronic noise peak is not complete and that they overlap; additionally, the proton peak has a significant width. The noise of the system was far higher than expected, which also can be seen in

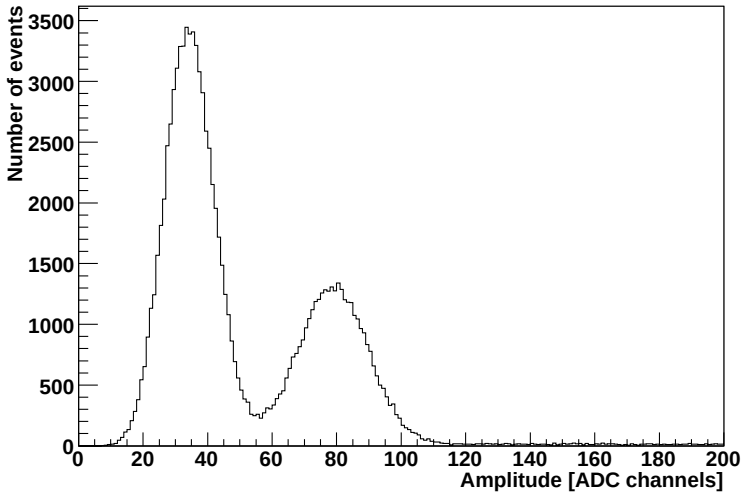

Figure 5.3: A pulseheight spectrum for one detector channel obtained by taking the maximum of a signal and subtracting the baseline determined from the same pulse.

the signal shape depicted in Fig. 5.2. There, the overlying noise is clearly visible; the signal-to-noise ratio is approximately 10:1, which is bad for a semi-conductor detector. A common-mode noise correction was planned for the read-out electronics and would have been valuable for reducing the noise, but unfortunately, it was not implemented due to reasons of time. Subsequently, significant time was invested to try and enhance the resolution of the energy spectrum and suppression of the noise in the offline analysis.

Averaging of the baseline

Analyzing the time-dependance of each channnel's baseline for one measurement cycle (see 5.2.1) showed that there is no significant drift of the value over time. This was done by extracting the mean baseline for all events of one measurement at the start of a cycle, several measurements during the cycle and the final measurement of the cycle. The result of this is shown in Fig. 5.4. It can be seen that over the complete cycle, the differ-

ence to the average baseline is negligible. The maximum deviation from the mean value is 0.3 ADC channels, with a standard deviation of 0.17 ADC channels. From this follows that for the extraction of the pulseheight, the

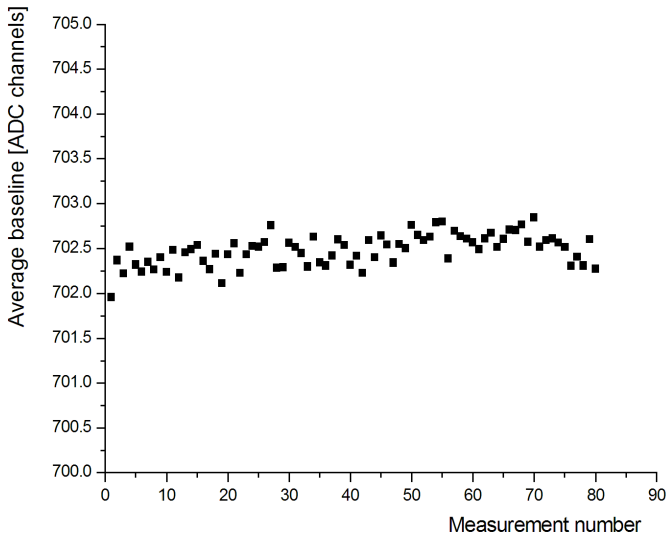

Figure 5.4: Averaged baseline for detector channel 13 as a function of the measurement number. The average value is 702.5 with a standard deviation of 0.17.

baseline value can be fixed for each channel instead of being determined on an event-by-event base. This results in a much more accurate value of the baseline, due to better statistics[7]. Fixing the baseline for each channel individually, and then subtracting that value from the maximum of the signal histogram for each event yields a pulseheight spectrum as shown in Fig. 5.5.

[7]Which are increased from 20 values in the case of event-by-event to several 10^6 by taking all events.

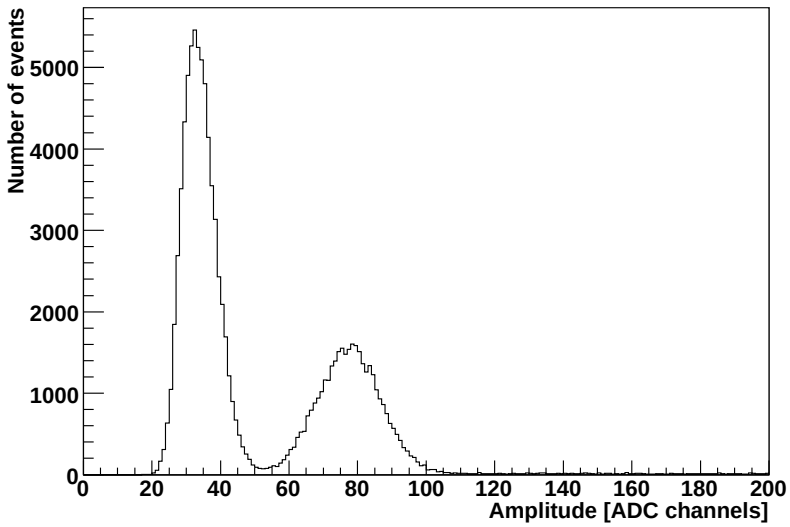

Figure 5.5: Pulseheight spectrum obtained by fixing the baseline, for the same channel and dataset as in Fig. 5.3.

Fitting of events

While the averaging of the baseline smoothes the noise in that component of the pulse, the maximum of the signal histogram can still be affected by it. To reduce that contribution, a fitting of the actual signal by a theoretical pulse shape can be done. The signal arriving at the ADC chip of the electronics has a shape which can be described by the product of two exponential functions with different time constants, as given in equation (5.1).

$$y(x) = \begin{cases} y_0 & \text{for } x < x_0 \\ y_0 + A \cdot \left(e^{-\frac{x-x_0}{\tau_1}}\right)\left(1 - e^{-\frac{x-x_0}{\tau_2}}\right)^p & \text{for } x \geq x_0 \end{cases} \tag{5.1}$$

The x-coordinate of this function's maximum depends on the time constants and p as follows:

$$x_{\max} = x_0 + \tau_2(\ln(p \cdot \tau_1 + \tau_2) - \ln(\tau_2)) \tag{5.2}$$

The function is shown in Fig. 5.6. The maximum value of the function

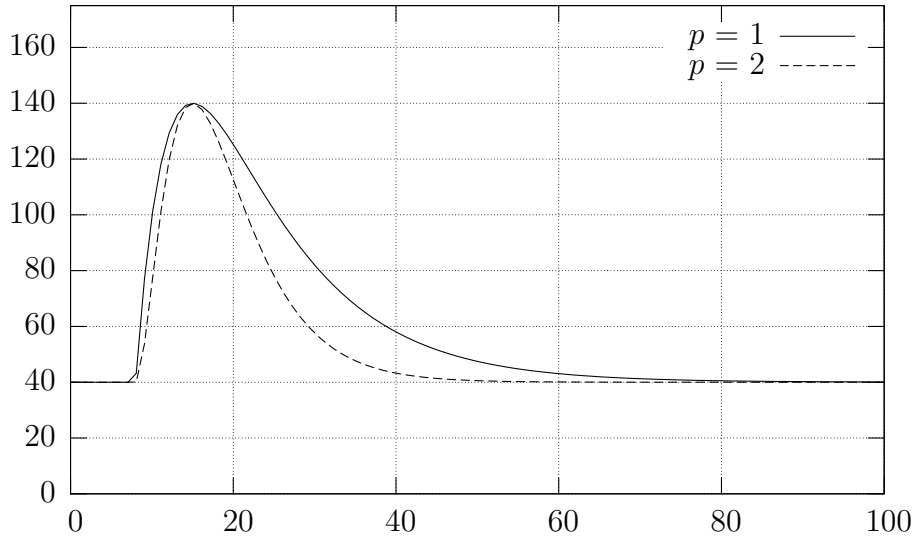

Figure 5.6: Theoretical shape of a pulse, as given in (5.1) for two different values of p. The parameters are $\tau_2 = 8$, $y_0 = 40$, $x_0 = 8$ and $x_{\max} = 15$. τ_1 is given by (5.3). A was chosen so that $y(x_{\max}) - y_0 = 100$.

depends on the parameters A, p, τ_1, and τ_2. Hence it is important to find suitable initial values for a fit. This can be done by examining a typical proton event, such as the one depicted in Fig. 5.2. The parameters y_0, x_0 and $x_{\max}$ are the ones most easily obtained and can easily be estimated by eye.

Of the time constants τ_1 and τ_2, only one has to be determined from a sample pulse. The other is then fixed and given by

$$\tau_1 = \frac{\tau_2}{p} \cdot \left(e^{\frac{x_{\max} - x_0}{\tau_2}} - 1 \right). \tag{5.3}$$

This relation is plotted in Fig. 5.7 for a value of $x_{\max} - x_0 = 7$ and $p = 1$. The scaling factor A is determined by

$$A = \frac{y(x_{\max}) - y_0}{e^{-\frac{x_{\max}}{\tau_1}} \cdot \left(1 - e^{-\frac{x_{\max}}{\tau_2}} \right)^p} \tag{5.4}$$

Thus, there are two parameters which can not be easily obtained from the characteristics of the signal histogram, namely τ_2 and p. To find suitable

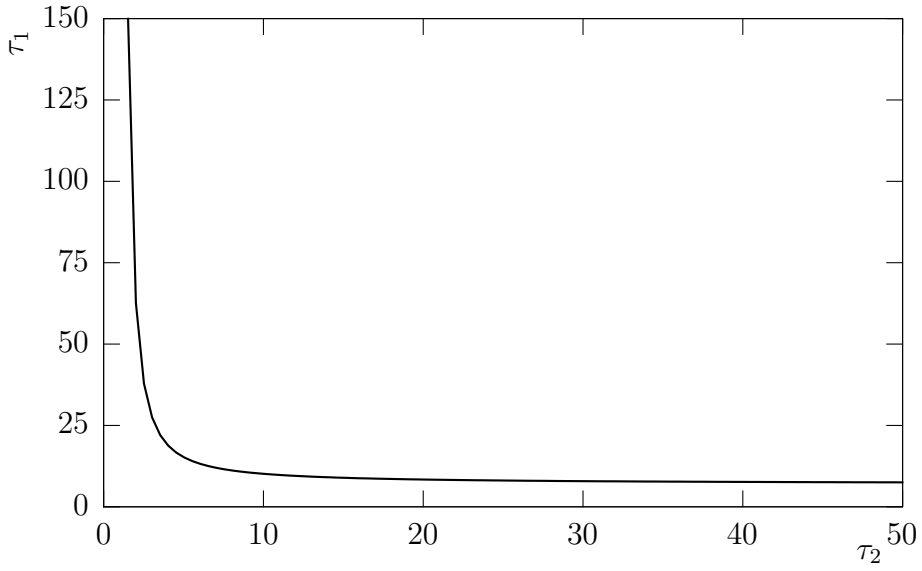

Figure 5.7: τ_1 as a function of τ_2 for a fixed value of $x_{\max} - x_0 = 7$ and $p = 1$.

initial values, a sample pulse has to be fitted with different initial values of τ_2 and p. The result of this is shown in Fig. 5.8

A pulseheight spectrum created by fitting each pulse and then histogramming the maximum of the fitted function is shown in Fig. 5.9. It should be noted already that the area under the proton peaks in Fig. 5.5 and Fig. 5.9 is the same within statistical limits. A comparison of both methods in regard to the value of a will be done later in this work. For all data presented, the method of fitting single events was used, unless otherwise mentioned.

Since every channel of the detector has subtly different parameters (e.g. the baseline of the ADC or slightly different amplifications), the pulseheight analysis has to be done separately for each channel.

5.3.3 Background treatment and extraction of protons

After the pulseheight diagram for one measurement has been created, the background, which is mainly comprised of electronic noise and electrons

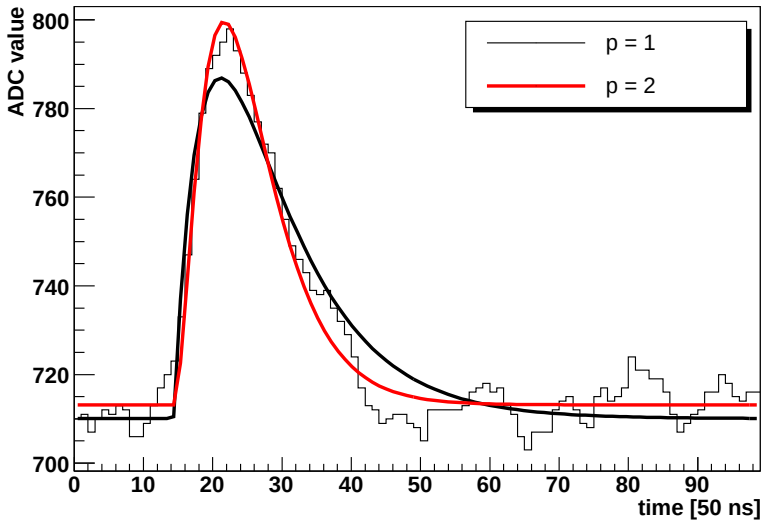

Figure 5.8: A proton signal fitted with the function given in (5.1) with two different values for p.

from neutron decay, has to be taken into account. It can either be subtracted using a measured background spectrum or it can be included into a fit of the uncorrected pulseheight spectrum. Figure 5.10 shows background measurements (i.e. analyzing plane voltage 780 V) with and without beam. It can be seen that the background with beam is comprised of two components: the electronic noise, which generates a peak at low ADC channels, and a component which is nearly constant across the energy range to which the detector is sensitive. The main source for this background are the electrons from neutron decay.

Method one - Subtraction of a background measurement

In the case of subtracting the background, the closest measurement taken at an analyzing plane voltage of 780 V is used as background spectrum. Both spectra have to be normalized by either measurement time or the neutron counter, since these parameters can be subtly different from measurement to measurement, which would lead to an incorrect number of protons extracted. A typical pair of normalized histograms can be seen in

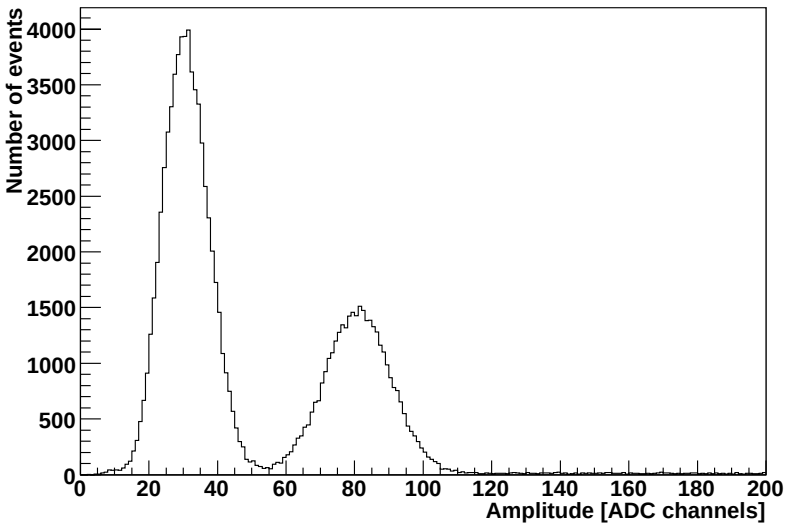

Figure 5.9: Pulseheight spectrum obtained by fitting the individual pulses. The same dataset as for the spectra depicted in figures 5.3 and 5.5 was used.

Fig. 5.11. The error bars represent the statistical uncertainty coming from the normalization process.

It is apparent from the background corrected spectrum that while the proton peak itself is rather clean, the background at lower ADC channels gets reduced, but not completely removed. This can lead to problems when extracting the number of protons from the spectrum and means that the integration limits have to be chosen carefully.

When using this method, once the background histogram has been subtracted, the sum over the histogram bins containing the proton peak yields the proton number. To obtain suitable integration limits, the pulseheight spectra of measurements at analyzing plane voltage 50 V[8] are fitted with the function (5.7). The limits were then set to

$$ll = x_0 - 3 \cdot \sigma \qquad ul = x_0 + 4 \cdot \sigma \tag{5.5}$$

[8]This voltage was chosen to obtain a well developed proton peak. As mentioned before, the width is dominated by the electronic noise and should be independent of the analyzing plane voltage.

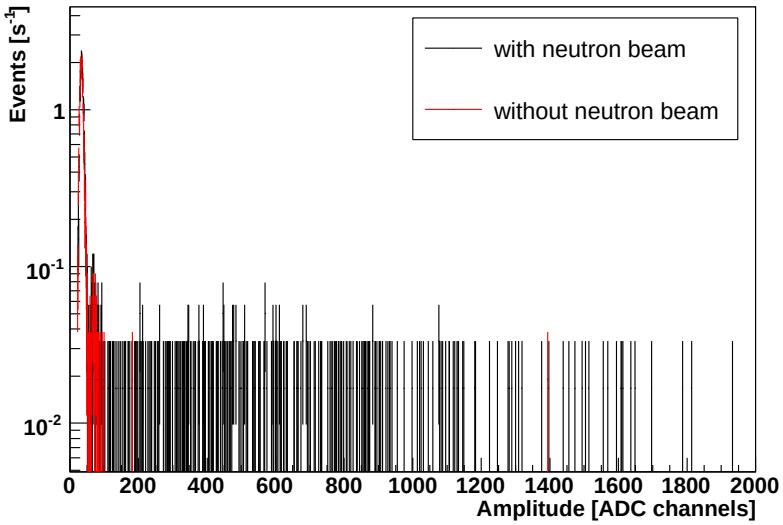

Figure 5.10: Pulseheight spectra recorded with 780 V applied to the analyzing plane. The black spectrum was taken with neutron beam, the red without. Both curves represent data taken over one minute.

These values were chosen because they minimize overlap of electronic noise and the proton peak while still covering most of the peak's area[9], which is shown in Fig. 5.12. The exception was channel 9, for which the electronic noise was higher, so the lower limit was changed to $x_0 - 2 \cdot \sigma$ (see also section 5.4.5).

The uncertainty in the number of protons with this method is given by the usual error propagation for a sum using the individual errors of the histogram bins.

Method two - Fitting the peak obtained after background subtraction

Another approach than to directly sum over the bins of the of histogram would be to fit the resulting proton peak with a Gaussian peak. The result of this fit is shown in Fig. 5.13. The advantage in this case is that

[9]The integral of a normalized Gaussian over the interval $[x_0 - 3\sigma; x_0 + 4\sigma]$ is 0.99862.

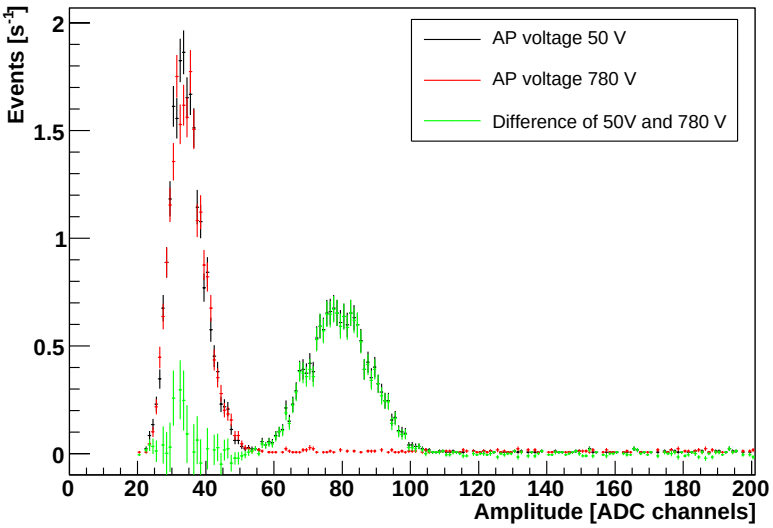

Figure 5.11: Illustration of method one of the proton extraction. The picture shows spectra taken with 50 V ad 780 V applied to the analyzing plane and their difference.

the area under the fitted Gaussian can easily be calculated for the entire peak, even if only a part of the histogram is used to fit the peak. The reason for choosing a Gaussian shape for fitting the peak is that the factor dominating the peak width is the electronic noise, which can be assumed to be normally distributed "white" noise [Kno99, p. 629 ff.].

If using this method, it is helpful to sum up the pulseheight histograms after subtracting the background measurements. This ensures that the statistics are sufficient for a good fit. Figure 5.14 shows one measurement at an analyzing plane voltage of 600 V on the left and the sum of all (background-subtracted) histograms, normalized by the number of measurements, on the right. It is clearly visible that the proton peak is more pronounced on the right picture.

To get the number of protons directly from the fit, the function

$$f(x) = A\frac{1}{\sqrt{2\pi}\sigma} \cdot e^{-\frac{1}{2}\left(\frac{x-x_0}{\sigma}\right)^2} \tag{5.6}$$

is used, which includes the area under the Gaussian as fit factor A.

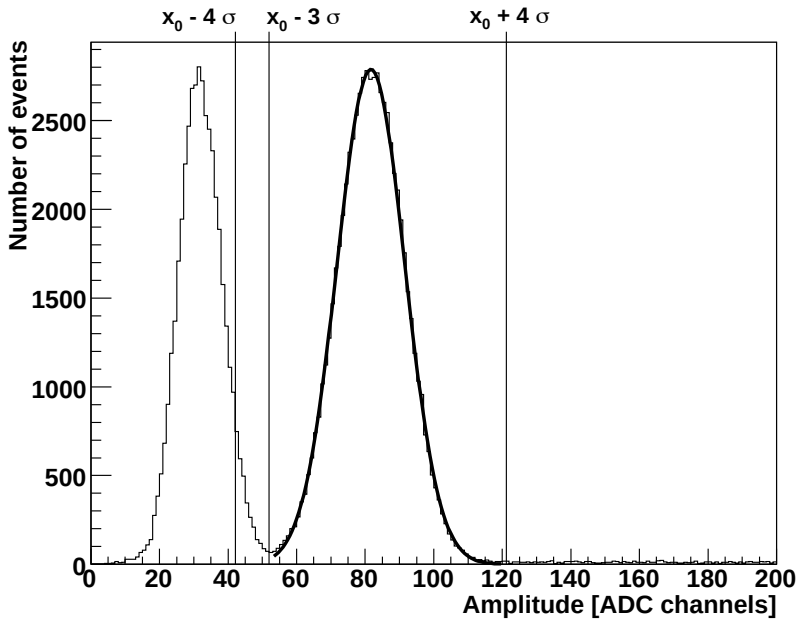

Figure 5.12: Integration limits for the proton peak, as used in method one.

Method three - Fitting of the pulseheight spectrum including the background

Another approach to treat the background is to fit the uncorrected pulseheight spectrum with a function that already includes the background. The shape of the pulseheight spectra depicted in figures 5.3, 5.5, and 5.9 suggest a Gaussian peak combined with a combination of a constant and an exponentially decaying background:

$$f(x) = A\frac{1}{\sqrt{2\pi}\sigma} \cdot e^{-\frac{1}{2}\left(\frac{x-x_0}{\sigma}\right)^2} + e^{b+c\cdot x} + B \tag{5.7}$$

The decaying exponential represents the electronic noise, while the constant accounts for the electron background[10]. As in function (5.6), the

[10]The electron background is not really constant across the energy range, as will be shown in section 5.5. However, since the count rates for a single measurement of one minute are fairly low (as can be seen in Fig. 5.15), the shape of the electron, a

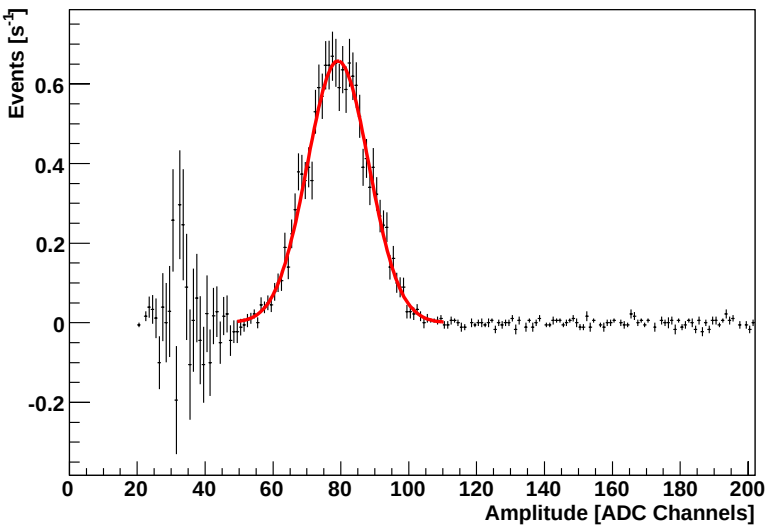

Figure 5.13: Fit of a background-subtracted pulseheight spectrum with a Gaussian (analyzing plane voltage 50 V), as it is done in method two.

Gaussian part of the function is normalized and thus its integral is included as fit parameter A. A fit of a pulseheight spectrum with this type of function can be seen in Fig. 5.15.

The advantage of fitting the entire pulseheight spectrum is that the actual background of the measurement itself is fitted, instead of subtracting a background gotten from another measurement, and thus is not sensitive to changes in the experimental environment happening between measurements. As with method two, the number of protons is given by the fit parameter A.

To get a set of good initial fit parameters, the following is done for each channel: The histograms of measurements with 50 V analyzing plane voltage are added up to obtain good statistics. These histograms are fitted with function (5.7), which is initialized manually. The parameters obtained from this fit are stored and used to initialize (5.7) for the fit of each individual measurement.

constant is a good approximation and a more complicated background function will not improve the result of the fit.

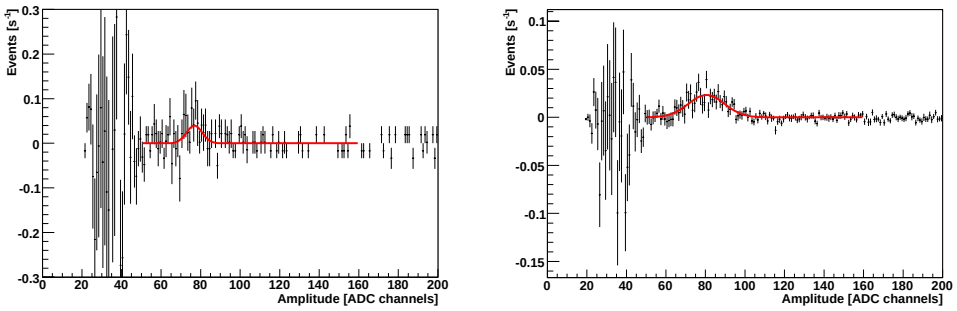

Figure 5.14: Fits of pulseheight spectra recorded with an analyzing plane voltage of 600 V after background subtraction: A single measurement (left, corresponding to one minute measurement time) and the sum of all measurements (right, corresponding to 20 minutes of measurement time).

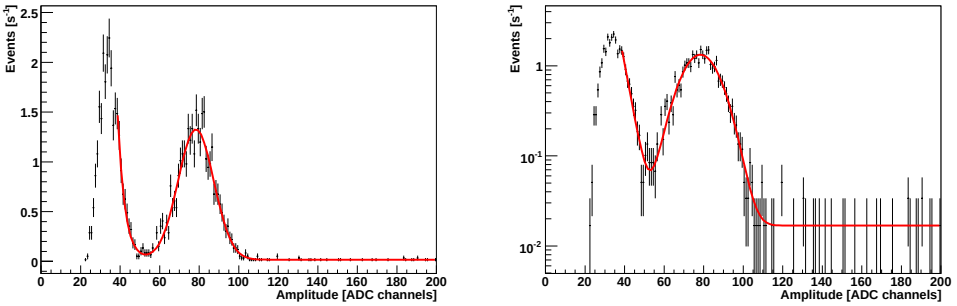

Figure 5.15: Illustration of method three of the proton extraction: A pulseheight spectrum fitted with the function (5.7), plotted logarithmic on the right side to better show the constant part of the background.

The channel histogram

For each measurement, the number of protons in each channel can be extracted in the ways described above. The total number of protons for that measurement is then given by the sum over all channels. Fig. 5.16 shows the distribution of protons over the detector channels for one measurement at an analyzing plane voltage of 50 V.

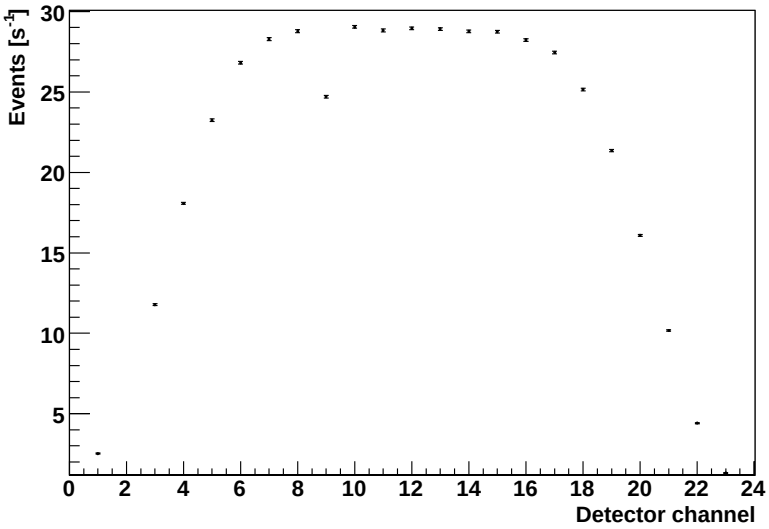

Figure 5.16: Protons per channel and second for the entire measurement cycle for analyzing plane voltage 50 V, obtained using method two. For a discussion of the lower count rate in channel 9, see section 5.4.5

5.3.4 Fitting of the integral spectrum

To obtain the integral proton spectrum from which a can be extracted, the number of protons for each analyzing plane voltage is determined by summing up the protons of all corresponding measurements, which have been calculated with one of the methods described above. Normalizing these values by the number of measurements for each analyzing plane voltage then gives the values for the integral proton spectrum.

The resulting datapoints are then fitted with a theoretical function $W(T)$ which includes a as fit parameter. The function is obtained by numerically integrating the product of the transmission function F_{tr} (3.21) and the differential proton spectrum $w_{\mathrm{p}}(T)$ (2.38)

$$W(T) = \int_0^{T_{\max}} F_{\mathrm{tr}} w_{\mathrm{p}}(T) dT \tag{5.8}$$

This function only contains three free parameters: An amplitude factor, the electron-antineutrino angular correlation coefficient a and the FIERZ parameter b, which in this analysis was fixed at a value of 0. A typical set of datapoints and their fit with function (5.8) is shown in Fig. 5.17.

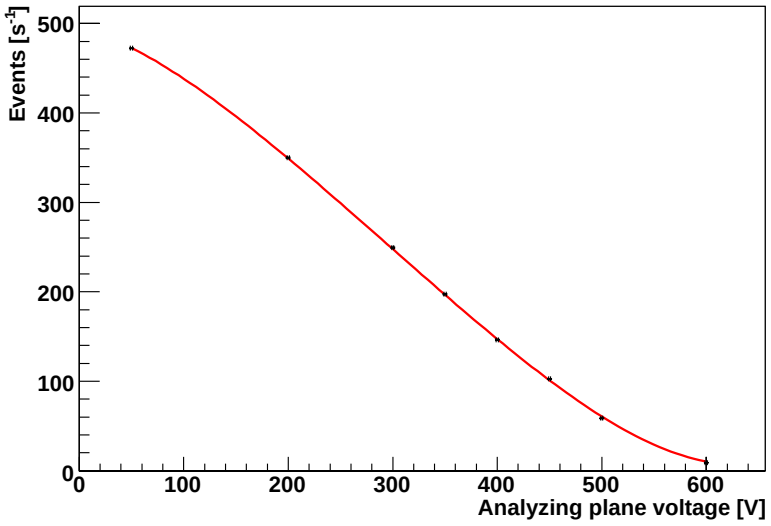

Figure 5.17: Integral proton spectrum, measured (black points) and fitted (red curve). The data points were obtained using method two and are listed in 5.2. The χ^2/NDF value of the fit is 5.01.

5.4 Results

In the framework of this work, one measurement cycle was analyzed in detail. It was taken between 0:30 and 18:00 on the 27th of April and is comprised of 681 individual measurements, each of which lasted one minute. The high voltage applied to the detector was 30 kV, the magnetic fields were set to about 50% of the maximum values, and the voltage differences applied to the upper and lower ExB electrodes was 2 kV and 150 V, respectively[11].

These measurements were taken with 9 different analyzing plane voltages. There were 8 "duplicate" measurements, in which the DAQ software wrote measurements to the same file twice in a row, which had to be discarded. Also, between 14:40 and 15:10 the beam had to be shut off while the DAQ kept running, resulting in "empty" files 562 to 581 which can't be used for analysis. The exact number of measurements per analyzing plane voltages can be seen in table 5.1.

AP voltage	0	50	200	300	350	400	450	500	600	780
number of measurements	216	80	21	21	20	20	21	20	20	214

Table 5.1: Number of measurements per analyzing plane voltage

The measurements at 0 V are not used for the determination of a, since ions could be generated between the decay volume and the analyzing plane. These would reach the detector and falsely be counted as protons if the potential barrier was set to 0 V. The reason why these measurements were performed nevertheless was to remove particles from the spectrometer which might have become trapped between the analyzing plane and the detector.

The trigger parameters can be seen in Fig. 5.18. Channel 2 was deactivated due to being excessively noisy. The threshold for channel 9 was slightly higher than for all other channels, since the electronic noise was also higher than average. The implications of this settings for a are discussed in section 5.4.5. Fig. 5.19 shows pulseheight spectra for channel 9 and channel 16. The maximum of the proton peak is located at the same ADC channel, but the electronic noise of channel 9 is markedly larger.

[11] The electrodes were set to -4 kV/-2 kV and -1 kV/-1.15 kV.

Figure 5.18: Thresholds and trigger parameters used the analyzed cycle.

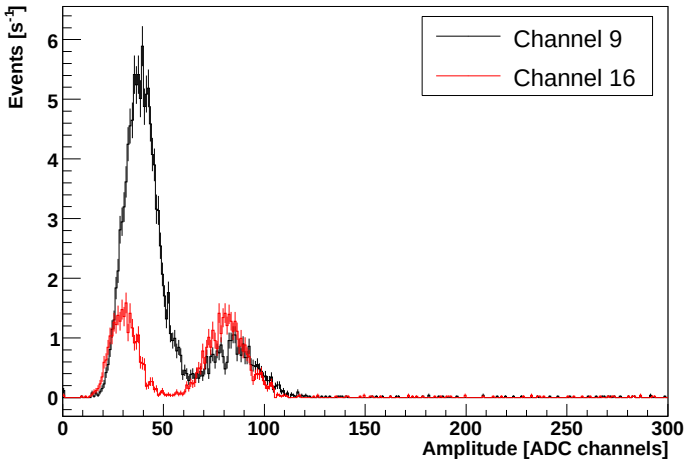

Figure 5.19: Pulseheight spectra for channel 9 and channel 16 of the same measurement.

The data was analyzed with the methods described before, and the pulse-height histograms were normalized by measurement time. This was done because the neutron counter was not yet synchronized exactly with the read-out PC and the neutron counts might therefore be off by some margin. The measurement time is calculated from the time stamps of the first and last events in the data file and is as such very precisely known[12].

[12] An uncertainty of 0.1 seconds is assumed internally when normalizing the histograms.

5.4.1 Proton count rates obtained

The proton numbers obtained for each analyzing plane voltage by the three methods explained in the previous section are listed in table 5.2 and shown in Fig. 5.20. The spectra agree very well with each others at low analyzing plane voltages, but method three deviates at high AP voltages markedly from the other methods.

Analyzing plane voltage [V]	Proton counts [s^{-1}]		
	Method one	Method two	Method three
50	471.80 ± 0.35	472.26 ± 0.35	470.59 ± 0.50
200	350.17 ± 0.59	349.77 ± 0.59	350.54 ± 0.57
300	249.63 ± 0.52	249.25 ± 0.51	250.14 ± 0.50
350	198.10 ± 0.48	197.41 ± 0.48	199.40 ± 0.45
400	146.90 ± 0.44	146.39 ± 0.43	150.21 ± 0.40
450	103.01 ± 0.37	102.55 ± 0.36	106.34 ± 0.86
500	58.94 ± 0.33	58.58 ± 0.32	66.16 ± 0.83
600	8.59 ± 0.25	8.77 ± 0.22	26.42 ± 0.62

Table 5.2: Proton count rates per analyzing plane voltage

5.4.2 Values of a extracted from the count rates

The spectra given by the count rates listed in table 5.2 were fitted as described in section 5.3.4. This yielded the values for a shown in table 5.3. Also listed is the distance of these values to the world average.

Methods one and two agree with each other within the statistical uncertainty, and are both fairly far away from the world average. Method three agrees with the world average value, but not with the other two methods; the reason for this is obviously the difference in count rates at high analyzing plane voltages, which is visible in Fig. 5.20. The reason for this divergence will be discussed in the following.

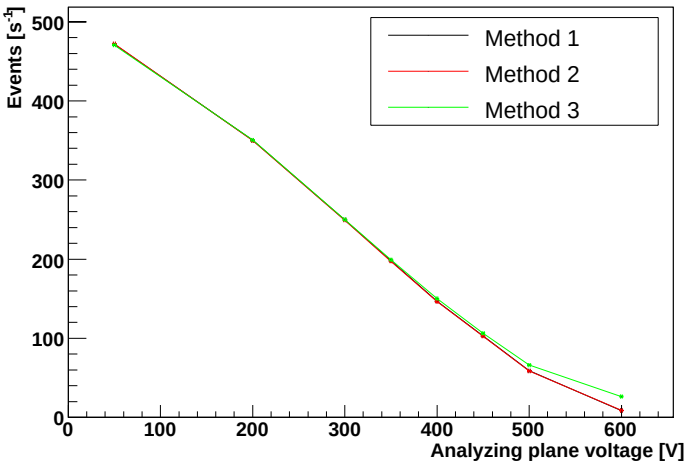

Figure 5.20: Count rates obtained with methods one to three, as defined in section 5.3.3.

5.4.3 Background under the proton peak

The different methods for treatment of the background were described in section 5.3.3. A closer look at a "background" measurement (i.e. a measurement with 780 V applied in the analyzing plane) shows that there are still events in the energy range of the proton peak. An example for this is shown in Fig. 5.21.

The shape of this "background peak" as it will be referred from here on, is similar to the proton peak, meaning one can fit the background measurements with (5.7) to get information about the peak's characteristics.

To obtain good statistics for the fit, again all background measurements for each channel are added before being fitted. The result of fitting the background of one channel in this way is shown in Fig. 5.22, and table 5.4 lists the fit results for both the background peak and measurements done with 50 V in the analyzing plane, where the proton peak dominates the fit.

For all channels, the the background peak is centred between 4 and 8 ADC channels below the proton peak and has a slightly bigger width.

Fig. 5.24 shows the number of background events for each measurement

Method of proton extraction	Value of a	Distance to world average
1	-0.1799 ± 0.0081	$\approx -9.5\ \sigma$
2	-0.1903 ± 0.0081	$\approx -10.8\ \sigma$
3	-0.1018 ± 0.0087	within statistical uncertainty

Table 5.3: Values of a obtained by the three different methods for proton extraction and their distance to the world average (-0.103 ± 0.004); all channels were used for the analysis. The given uncertainties are purely statistical.

depending on the channel number. These background events appear more prominently in the center channels, which is an indication that they are beam-correlated. The values shown in Fig. 5.23 are the mean values of all measurements for the corresponding channel. These values do not vary significantly with time, as can be seen in Fig. 5.24, which shows the dependence of the numbers on the measurement number for channel 16.

It becomes clear from this that method three is not a good way of extracting protons from the pulseheight spectrum, at least not for the studied measurement cycle, since the background peak is not included in the fit function. A puzzling effect is on the first glance that the proton count rate is not higher for method three at all analyzing plane voltages. It should be, since the background peak is always subtracted when using methods one or two.

The reason for this effect can be seen in Fig. 5.15, which depicts a measurement at 50 V. Due to the statistics, the fit agrees with the data even though it probably underestimates the area of the proton peak. Since the shape of the peak at this voltages is dominated by the proton peak, the slight "bump" it gets is attributed to statistics. At higher analyzing plane voltages, the contribution from the background peak is included into the fit, resulting in a higher count rate.

To verify this assumption, one can look at how the situation changes if one adds up all pulseheight histograms for one analyzing plane voltage and all channels, and then fits the resulting spectrum with function (5.7) to extract the proton numbers. This improves the statistics enough to get more accurate fits. The result of this can be seen in Fig. 5.25, with the

Detector channel	Background peak		Proton peak	
	x_0	σ	x_0	σ
0	77.53 ± 0.63	15.68 ± 0.88	81.95 ± 0.26	11.57 ± 0.27
1	76.43 ± 0.38	13.76 ± 0.45	81.46 ± 0.10	10.04 ± 0.09
2	-	-	-	-
3	75.01 ± 0.26	12.38 ± 0.31	81.15 ± 0.05	9.86 ± 0.04
4	77.52 ± 0.24	12.89 ± 0.27	83.94 ± 0.04	9.98 ± 0.03
5	74.49 ± 0.21	12.08 ± 0.22	81.79 ± 0.03	9.89 ± 0.03
6	75.66 ± 0.19	12.26 ± 0.20	82.95 ± 0.03	9.94 ± 0.02
7	73.62 ± 0.16	11.77 ± 0.18	80.97 ± 0.03	9.74 ± 0.02
8	73.03 ± 0.17	11.98 ± 0.18	80.84 ± 0.03	9.69 ± 0.02
9	77.07 ± 0.98	14.35 ± 0.59	84.24 ± 0.05	11.64 ± 0.04
10	72.19 ± 0.25	12.29 ± 0.22	79.60 ± 0.03	10.18 ± 0.03
11	73.17 ± 0.13	11.16 ± 0.14	80.53 ± 0.03	9.71 ± 0.02
12	74.32 ± 0.13	11.43 ± 0.14	81.84 ± 0.03	9.89 ± 0.02
13	72.63 ± 0.13	10.77 ± 0.14	79.88 ± 0.03	9.74 ± 0.02
14	73.82 ± 0.14	11.15 ± 0.15	80.86 ± 0.03	9.71 ± 0.02
15	74.23 ± 0.15	11.54 ± 0.16	81.69 ± 0.03	9.72 ± 0.02
16	73.93 ± 0.16	11.40 ± 0.17	81.12 ± 0.03	9.65 ± 0.02
17	73.76 ± 0.18	11.70 ± 0.19	80.67 ± 0.03	9.62 ± 0.02
18	74.17 ± 0.20	11.89 ± 0.23	80.87 ± 0.03	9.78 ± 0.02
19	73.70 ± 0.22	11.96 ± 0.25	80.63 ± 0.03	9.50 ± 0.03
20	75.72 ± 0.26	12.14 ± 0.27	81.50 ± 0.04	9.77 ± 0.03
21	73.90 ± 0.25	11.32 ± 0.28	79.29 ± 0.05	9.46 ± 0.04
22	75.23 ± 0.32	12.41 ± 0.38	80.18 ± 0.07	9.67 ± 0.06
23	73.79 ± 0.35	12.09 ± 0.40	78.84 ± 0.14	9.80 ± 0.13

Table 5.4: Center (x_0) and width (σ) of the background and proton peaks for channel 16. All values are in units of ADC channels.

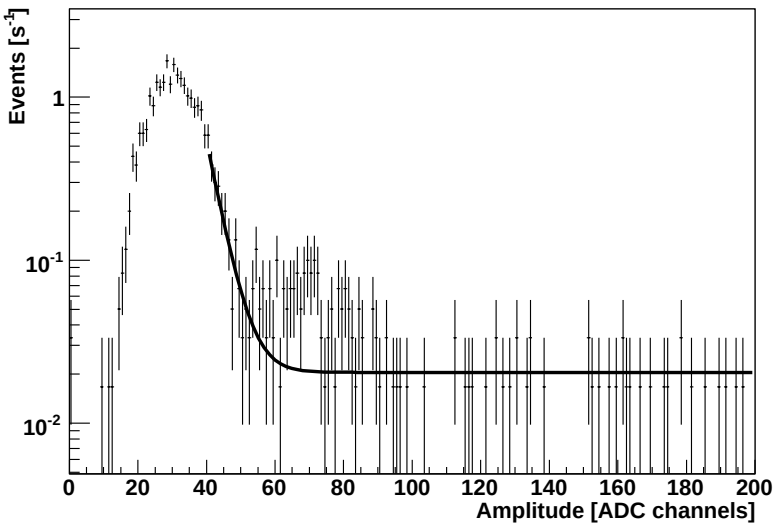

Figure 5.21: The pulseheight histogram of one background measurement (one minute measurement time) of channel 16 fitted with the background part of (5.7). There are events in the region between ADC channels 60 and 80, which is the interval in which also the proton events are registered.

count rates obtained by method two for comparison.

It is obvious that there is simply a constant offset between the two methods, in contrast to the increasing divergence which was observed (see Fig. 5.20) when using method three as it was described in section 5.3.3.

An interesting question is if the background peak depends on the analyzing plane voltage in any way or not. From looking at Fig. 5.25, it seems likely that if there is any such effect, it is a small one. Unfortunately, there is no way to obtain information about this from the pulseheight spectra directly, since if the analyzing plane voltage is set to values lower than 780 V, the proton peak and the background peak will overlap and a separation of the two is very difficult.

However, since the background peak can be fitted, one possible way to gain additional information would be to include it as a second Gaussian in the complete fit function:

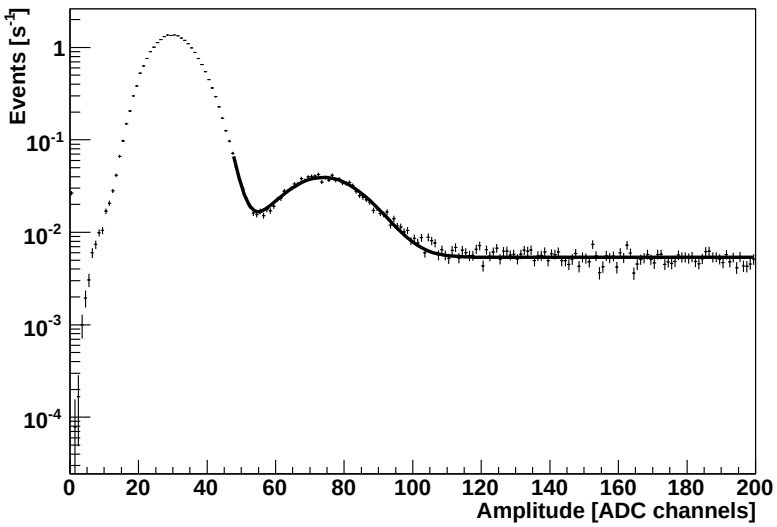

Figure 5.22: The summed up background spectra of channel 16, fitted with (5.7).

$$f(x) = A\frac{1}{\sqrt{2\pi}\sigma}\cdot e^{-\frac{1}{2}\left(\frac{x-x_0}{\sigma}\right)^2} + A'\frac{1}{\sqrt{2\pi}\sigma'}\cdot e^{-\frac{1}{2}\left(\frac{x-x_0'}{\sigma'}\right)^2} + e^{b+c\cdot x} + B \quad (5.9)$$

If one initializes this fit function with carefully chosen parameters (obtained from only fitting the background and from fitting 50 V measurements, where the proton peak dominates), one can fit pulseheight spectra for each analyzing plane voltage with this function and see whether the area under the background peak changes. The values x_0, σ, x_0' and σ' were constrained heavily, since they are fairly well known from fitting the 50 V and 780 V measurements, respectively. Again, to have sufficient statistics for a fit, added histograms need to be used. Figure 5.26 shows a pulseheight spectrum recorded at 600 V in the analyzing plane and fitted with function (5.9). It appears to reproduce both peaks. However, if one looks at the χ^2/NDF values for this fit (1.40) and a fit of the same spectrum with function (5.7) (1.25), there is no indication that this method results in a better agreement of the fit with the measured data.

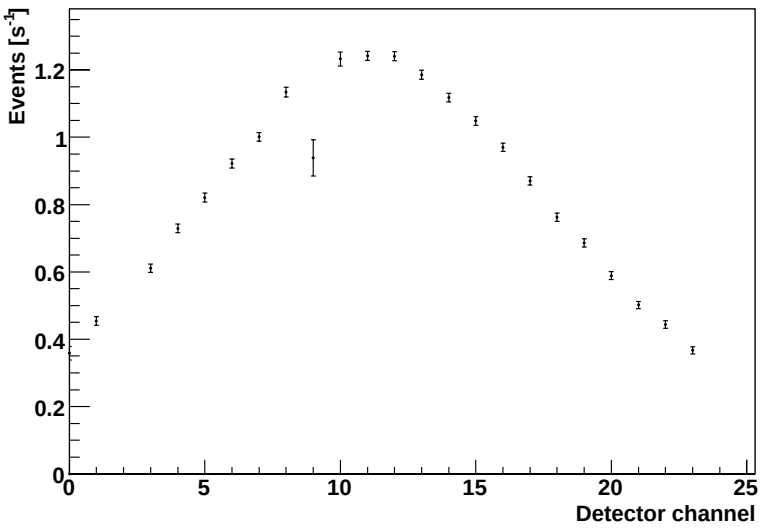

Figure 5.23: Mean number of events in the background peak for all channels.

The fit depicted in Fig. 5.26 is also very sensitive to changing initial parameters as well as the range of the fit. It should therefore not be relied on for proton extraction at all. The only thing of interest that might be learned from fitting pulseheight spectra in such a way is if the area under the background peak shows any dependence at all on the analyzing plane voltage. Figure 5.27 shows a plot of this value versus the analyzing plane voltage for channel 16. It should be noted that even if there was a dependence, it certainly can't be resolved with this method.

For the further analysis, the background peak is assumed to not depend on the analyzing plane voltage. We do not have any proof for this, but neither is there any way to find out from looking at one data set only. Efforts are underway to study the effect depending on external parameters such as the ExB voltage by our colleagues in Mainz.

In effect, the presence of the background peak makes method three unsuitable for the extraction of protons. One could use the method of summing all histograms of one channel for each analyzing plane voltage, then

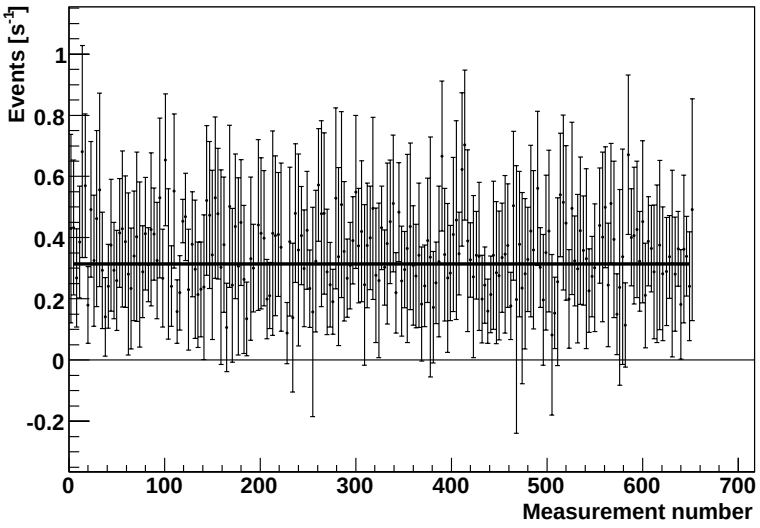

Figure 5.24: The number of events in the area of the proton peak depending on measurement number for the detector channel 16.

fitting these spectra with function 5.7, and subtracting a constant background from this value to account for the background peak. However, since the idea of method three was to be independent of possible background fluctuations by fitting single measurements, this procedure would be defeating the purpose. For single measurements, the statistics apparently is not good enough to get reliable results.

In the following, method two will be used for extracting protons solely. Methods one and two agree well with each other, method two has however the advantage that it is independent of possible effects imposed by the integration limits, since the number of protons always corresponds to the area under the full Gaussian.

5.4.4 Gaussian shape of the proton peak

To check whether a Gaussian is really a good choice as fit function for the proton peak, one can check the stability of its x_0 and σ values when analyz-

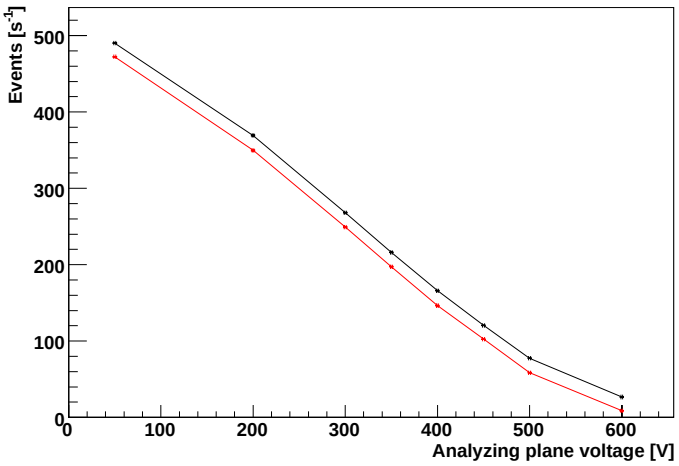

Figure 5.25: Proton count rates obtained by using method two (red) and by adding all pulseheight histograms for each channel and analyzing plane voltage and fitting the resulting spectrum with (5.7) (black).

ing pulseheight spectra of different analyzing plane voltages with method two. If x_0 only varies slightly, and σ, remains constant the Gaussian is a good choice. The reasoning for this is that the center of the peak is expected to move slightly with higher analyzing plane voltage, since the mean energy of protons will be higher in these cases, but the σ is dominated by the electronic noise, which should not depend in any way on the analyzing plane voltage. The results of this analysis for channel 16 can be seen in table 5.5 .

As expected, the x_0 value is shifted to slightly larger values with increasing analyzing plane voltage. Since we can deduce from the position of the peak at 50 V that one ADC channel corresponds to roughly 300 eV of energy[13], the observed shift of 1-2 channels agrees well with the expectations. The σ is constant within uncertainty limits, also as expected. Together with the fact that χ^2/NDF values are close to 1 for all channels, this confirms that the Gaussian is a good representation for the proton

[13]It should be noted that this is just an estimate and shouldn't be considered an exact calibration.

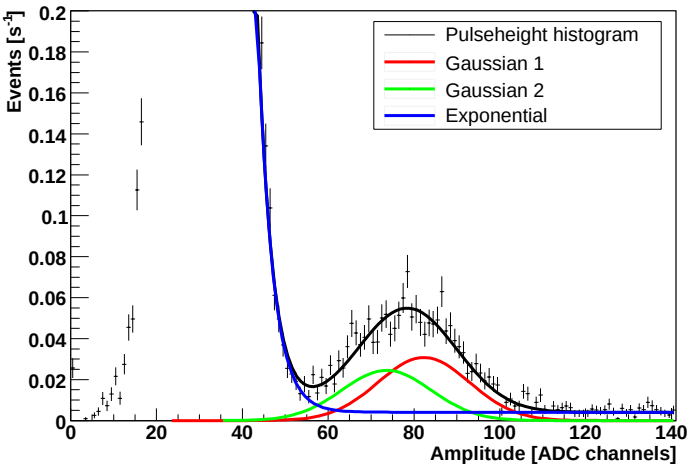

Figure 5.26: Fit of the added 600 V pulseheight spectra for channel 16 with function (5.9).

peak.

5.4.5 Effect of channel 9

From Fig. 5.16, it can be seen that the proton count rates are very similar in the central part of the detector, excepting channel 9. Fig. 5.28 shows a blow-up of the Fig. 5.16, focusing on the central channels. The black points denote proton count rates extracted with method two.

It is possible to correct this effect; since the count rates in the neighbouring channels are very homogeneous, one can calculate the mean value of channels 8 - 13 (without channel 9) and assign that value to channel 9. This is shown with the red points in Fig. 5.28.

The increase of the count rates is in the order of 1% for all analyzing plane voltages, hence there is also no change in the general shape of the spectrum. The resulting value of a is

$$a = -0.1895 \pm 0.0081$$

and as such the same within the statistical uncertainty as the value given

AP voltage [V]	Fit parameters of the Gaussian		
	x_0	σ	χ^2/NDF
50	81.30 ± 0.29	9.54 ± 0.03	0.96
200	81.50 ± 0.07	9.48 ± 0.05	1.08
300	81.86 ± 0.08	9.45 ± 0.07	0.98
350	81.80 ± 0.10	9.50 ± 0.08	1.10
400	82.07 ± 0.12	9.47 ± 0.10	1.00
450	81.85 ± 0.15	9.46 ± 0.12	0.92
500	83.77 ± 0.22	9.53 ± 0.19	0.96
600	82.58 ± 1.03	8.62 ± 0.90	1.07

Table 5.5: Fit parameters of the Gaussian versus the analyzing plane voltage for channel 16.

AP voltage [V]	Count rate after correcting channel 9	
	Absolute [s^{-1}]	Relative to uncorrected [%]
50	476.45 ± 0.35	100.89 ± 0.11
200	352.80 ± 0.60	100.87 ± 0.24
300	251.53 ± 0.52	100.91 ± 0.29
350	199.30 ± 0.49	100.96 ± 0.35
400	147.74 ± 0.44	100.92 ± 0.42
450	103.36 ± 0.37	100.79 ± 0.51
500	59.05 ± 0.33	100.80 ± 0.79
600	8.93 ± 0.24	101.82 ± 3.74

Table 5.6: Count rates after correcting channel 9 (absolute and percentages)

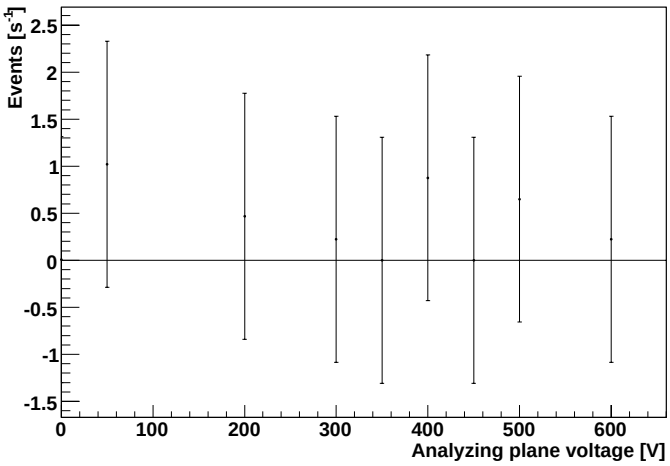

Figure 5.27: The values for the amount of events in the background peak obtained from fitting the summed pulseheight spectra with function (5.9) for channel 16.

in table 5.3.

5.4.6 Geometric effects

The geometry of the spectrometer could have effects on the count rate as well. They could e.g. stem from the finite size of the diaphragm defining the diaphragm. To investigate a possible effect on the integral proton spectrum, we compare the spectra (and corresponding values for a) which are obtained by analyzing all channels and the spectra gained from only the central detector channels which show a basically constant count rate, as seen in Fig. 5.16. To avoid additional effects from channel 9, the central channels are defined as the channels 10-16. Including only these channels in the analysis, one obtains the count rates listed in table 5.7.

Figure 5.29 shows the fraction of events which is counted in the central channels compared to the full detector. It is visible that for higher analyzing plane voltages, that fraction decreases. This has in turn an effect on

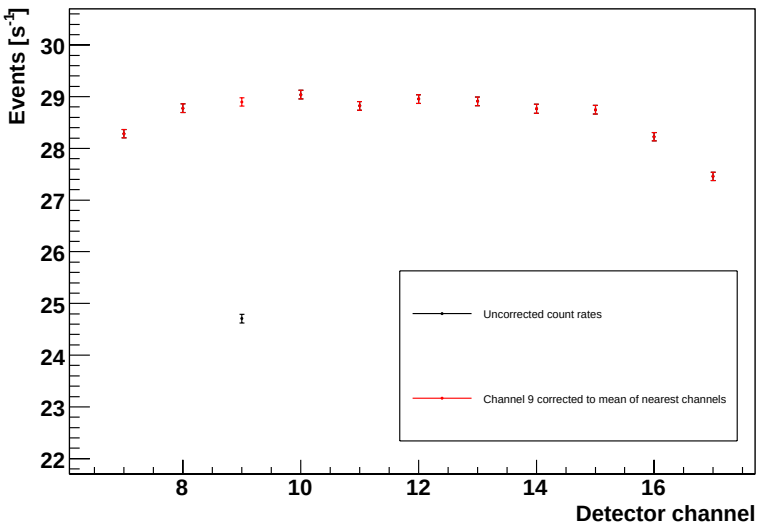

Figure 5.28: Protons per channel in the center region of the detector, count rates obtained with method two.

the value of a, which is

$$a = -0.22468 \pm 0.00895.$$

As expected from the shift in count rates (towards lower analyzing plane voltages), a gets shifted to a more negative value. The shift is clearly greater than the statistical uncertainty. From the point of view of the detector, it might be that low energy protons are more likely to be lost in the outer channels (leading to a higher percentage for those in the center channels) due to the very low statistics in these channels even at low analyzing plane voltages.

Another possible effect is the different deflection of slow and fast protons in the ExB drift electrodes, which might result in slower protons being more likely to miss the detector at the outer channels. However, this effect should be small in the presented data, since the effect is in the order of 0.5 mm, which corresponds to half a detector channel, for the applied voltages.

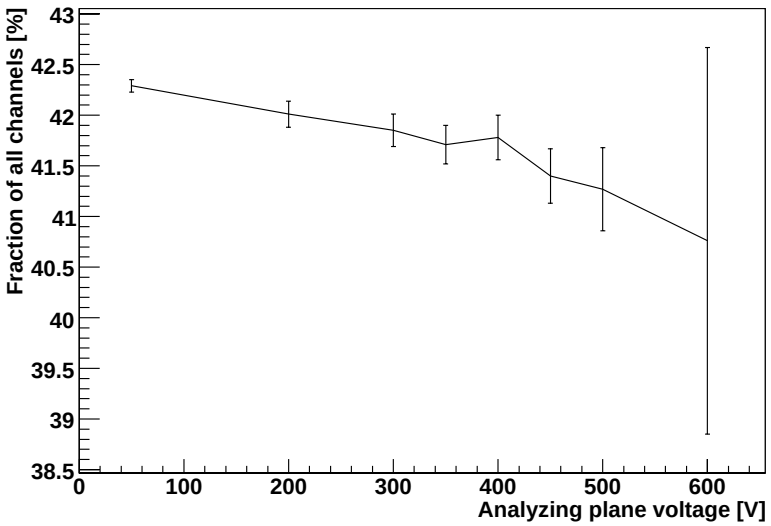

Figure 5.29: Fraction of the full detector's count rate contained in the center channels.

5.4.7 Reliability of the fit procedure for single events when obtaining pulseheight spectra

In section 5.3.2, the methods to extract pulseheight spectra from the raw data were described. Even though the spectra depicted in Fig. 5.5 and 5.9 are very similar, it is possible that events which are protons but have a noise spike in one of their flanks or close to the proton pulse, are fitted in a wrong way and possible discarded later on. Figure 5.30 shows one such event, together with its fit. Even though in this example, the fit converges, it is not guaranteed that this would be always the case.

To investigate a possible effect on a, pulseheight spectra were extracted both with and without fitting the events and then analyzed with the methods described above. In all cases, the obtained values for a are different on a 10^{-4} (absolute) level, which is lower than the statistical uncertainty by one order of magnitude.

AP voltage [V]	Count rate in the center channels	
	Absolute [s^{-1}]	Fraction of full detector [%]
50	201.47 ± 0.22	42.29 ± 0.06
200	148.21 ± 0.38	42.01 ± 0.13
300	105.26 ± 0.33	41.85 ± 0.16
350	83.13 ± 0.31	41.71 ± 0.19
400	61.72 ± 0.27	41.78 ± 0.22
450	42.79 ± 0.23	41.4 ± 0.27
500	24.37 ± 0.2	41.27 ± 0.41
600	3.64 ± 0.14	40.76 ± 1.91

Table 5.7: Count rates obtained using only channels 10-16 (absolute and percentages)

5.4.8 Fluctuations of background with time

When subtracting background spectra, always the closest measurement was chosen to be independent of possible fluctuations in time. To investigate if there actually was any fluctuations which would influence the proton numbers, the analysis was also done with subtracting background spectra that were 5, 10, 15 or a random number between 1 and 20 measurements removed from the initial spectrum[14]. The resulting values of a for methods one and two can be seen in table 5.8.

There are differences between the values on a 10^{-3} level, which is lower than the statistical uncertainty, but could become significant when the latter is improved. This difference also increases with the distance of the background measurement to the original measurement. For this reason, subtracting the next nearest measurement is a good approach.

[14] These values correspond to time differences between about 30 and 75 minutes. For comparison, the time difference between a measurement and the nearest background measurement is usually five minutes.

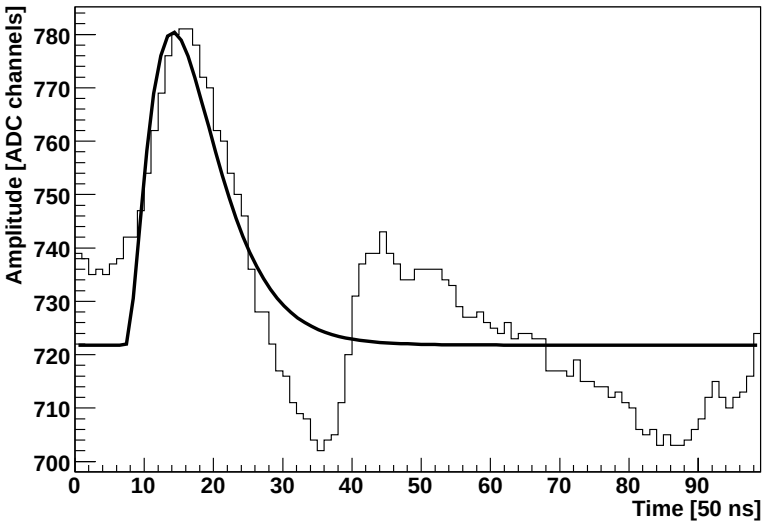

Figure 5.30: An event accompanied by a large noise fluctuation.

5.4.9 Energy dependence of detector efficiency

A change in detector efficiency for protons with different initial energies would result in a systematic effect for a due to the count rates at different analysing plane voltages being affected by that.
Lately, simulations with the program SRIM-2006 [Zie07] have shown that the detection probability for protons with an initial kinetic energy of 30 keV is smaller than the probability for protons with an initial kinetic energy of 30.8 keV by about $3 \cdot 10^{-4}$ [Sim07a]. This simulation did not take into account the electronic noise we observed in the experiment, however.

With the count rates we had in this experiment, this corresponds to an effect in the order of 10^{-2} for the count rate values. The effect would shift the spectrum towards lower energies and as such more negative values of a. A change of 1 s^{-1} in the count rate at 600 V results in a change of the value of a in the order of $5 \cdot 10^{-3}$. As such, the influence of the detector efficiency will be about two orders of magnitude smaller than the effects described above.

Studies and simulations of an energy dependence of the detector are still

Offset to the next nearest background measurement	Value of a
0	-0.1895 ± 0.0081
5	-0.185 ± 0.0081
10	-0.1888 ± 0.0081
random	-0.1872 ± 0.0081

Table 5.8: Dependence of the values for a on the proximity of the subtracted background measurements.

on-going.

5.4.10 Temperature stability of the detector and the electronics

Another possible systematic effect is a slow change of the temperature of the detector itself and the electronics. Both could result in a time-dependent change of the electronic noise and as such the width of the proton peak.

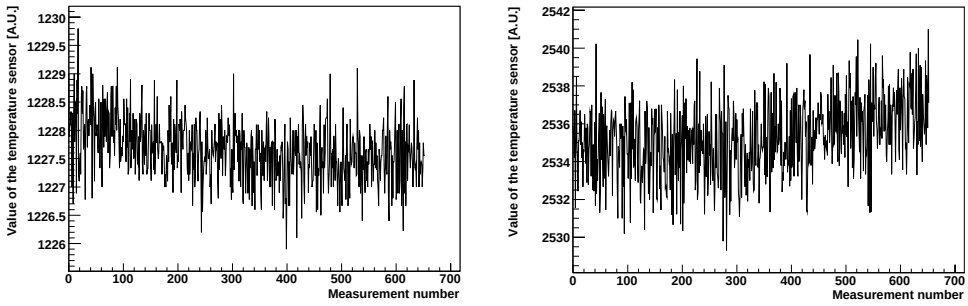

Figure 5.31: The values of the temperature sensors mounted on the detector PCB (left) and the preamplifiier board (right).

Looking at the data set from the 26./27. of April, the mean temperature of each measurement vs. the measurement number is plotted in Fig. 5.4.10, for both the preamplifier and the detector. A slight rise in preamplifier temperature is recognizable, whereas the detector temperature remained

practically constant. From a very rough calibration of the temperature sensors which was done after the beam times, we can say that the change of temperature in both cases is less than 1 K [Sim07a]. The reason for this is likely the fact that after insertion of the detector into the cryostat, both the magnetic field and the high voltage have to be ramped up before a measurement can be started. Since these two processes take considerable time, the detector reaches a temperature equilibrium with the surrounding cryostat. The heat coupling of the electronics to the detector seems to be small enough so that the small heating of the electronics doesn't affect the detector. As such, we can not draw any conclusions about the influence of temperature fluctuations on the data.

While the values of temperature sensor on the preamplifier board showed roughly room temperature, the sensor on the detector board was unfortunately not calibrated for an absolute temperature measurement.

5.5 Discussion of the background

As has been mentioned before, the background in these measurements is comprised of three parts:

- The electronic noise, which is an exponentially decaying noise at low amplitudes.
- The electrons from the neutron decay, which contribute background across the sensitive energy range.
- A peak centered approximately 10 ADC channels below the proton peak.

5.5.1 Correlated electron background

Of the electrons which are generated in neutron decay, 50% will be emitted into the direction of the analyzing plane and the proton detector. Due to the high voltage applied to the detector, all electrons with kinetic energies lower than 30 keV will be reflected by the electrostatic potential. Looking at the spectrum described in 2.3.1, this corresponds to about 2% of the electrons.

In addition, the increasing magnetic field towards the top of the detector acts as magnetic mirror for the electrons. Is we assume adiabaticity, we can use (3.4) to calculate the maximum angle that the electron momentum may have initally in respect to the magnetic fields lines to be able to reach the detector.

For the field ratio $B_{\mathrm{det}}/B_0 \approx 2$, as it is in *a*SPECT, this angle is 45°. Solid angle considerations show that this amounts to about 30% of the electrons emitted into this half space.

Taking all this together, one can estimate that about 14.7% of the electrons generated in neutron decay will be able to reach the detector. According to simulations done with the program PENELOPE [Sal06], the backscattering fraction for electrons from neutron decay on silicon is in the order of 10 - 15%[15]. If we use this to assume a detection efficiency of about 85% - 90%, $12.9 \pm 0.4\%$ of the electrons from neutron decay will actually be detected.

Electrons and protons from one neutron decay event will arrive at the detector within a well defined time window, which is given by the distance of the detector to the decay volume and the momenta of the particles. We can expect a proton hitting the detector roughly 6 μs after the corresponding electron at the earliest. Depending on the applied lower and upper ExB drift voltages, the proton will hit the same detector channel, or an adjacent one.

Figure 5.32 shows a three-dimensional plot of the time- and channel-correlations[16] between and event i and the consecutive event $i+1$ of one measurement, where i runs over all events (AP voltage was 50 V). There is a clearly visible peak (called *correlation peak* from now on) rising at a time distance of roughly 7-8 μs and a positive channel distance of 1-2 detector channels. The width of the peak is about 4 channels in the y-dimension. The main source for this spread is the gyration radius r of the protons in the magnetic field at the detector. It is given by

$$r[\mathrm{m}] = \frac{p_\perp[\mathrm{MeV}/c]}{300\ B[\mathrm{T}]}, \tag{5.10}$$

[15] These simulations were done using the PENSLAB program of the PENELOPE package, which simulates particles impinging on a block of material. As source, electrons with an energy distribution according to (2.33) were used; the angle of incidence was varied between 0° and 12°. Silicon with a thickness of 0.3 mm was used as target.

[16] With the time-difference on the x-axis and the channel difference on the y-axis.

where $p_\perp$ is the momentum component normal to the magnetic field line. $r_{\max} \approx 1.4$ mm for a magnetic field of 3 T at the detector. In addition to this, lower energetic protons will be deflected stronger in both ExB electrodes than higher energetic protons. For the applied voltages, slower protons will be deflected by about 0.5 mm more than faster ones, resulting in an additional widening of the peak by this distance.

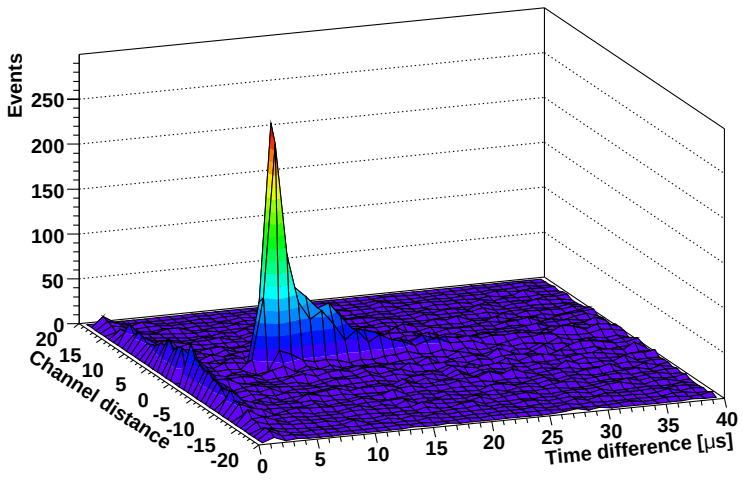

Figure 5.32: The time- and channel-correlation of consecutive events in measurement 141 of the analyzed measurement cycle.

Since the first event after an electron hits the detector isn't necessarily the correlated proton, we can look at the same correlation for event i and event $i + j$, with $j > 1$. The resulting histograms for $j = 2$ and $j = 3$ can be seen in Fig. 5.33 and Fig. 5.34, respectively. There are still some events in the correlation peak for $j = 2$, but none for $j = 3$.

The influence of the ExB voltage on the peak can be seen in Fig. 5.35, which shows the a two-dimensional plot of the time-channel-distance spectra for voltage differences of 0 kV and 4 kV applied to the upper ExB electrode. That the peak is centered at a channel distance of about -7 channels for 0 kV is due to the lower ExB electrode[17]. This plot also shows

[17]These measurements were not done in the same measurement cycle of the 26./27. of

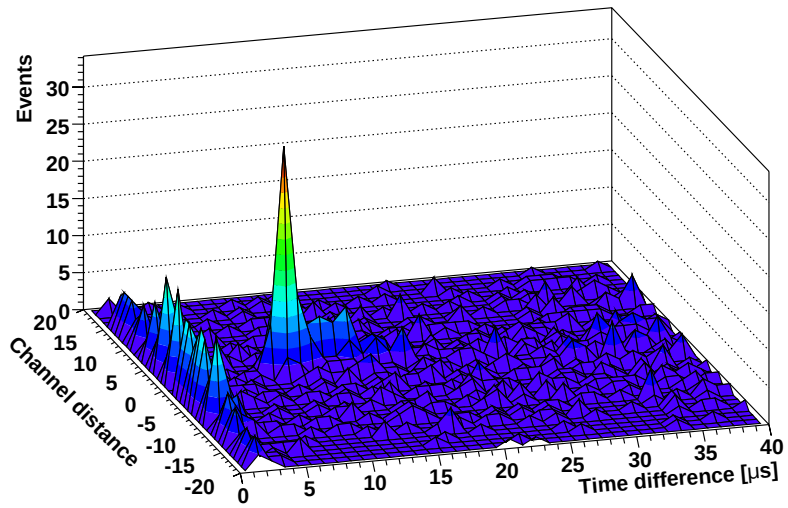

Figure 5.33: The time- and channel-correlation of events i and $i + 2$ in measurement 141 of the analyzed measurement cycle.

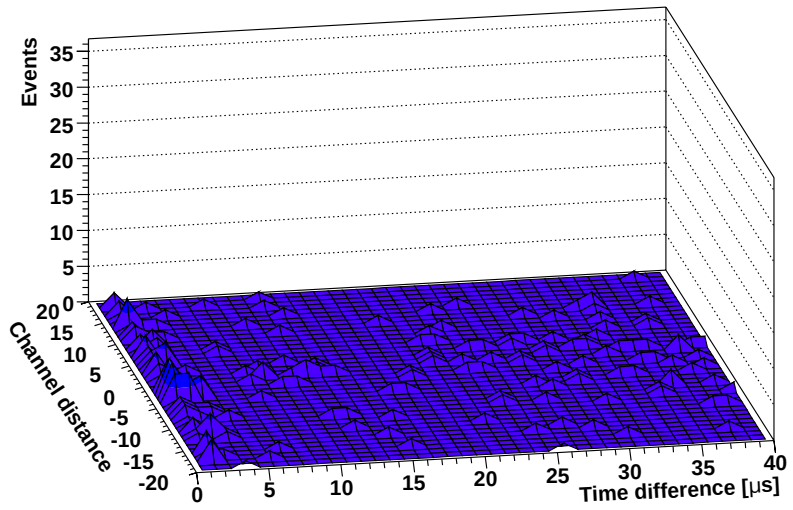

Figure 5.34: The time- and channel-correlation of events i and $i + 3$ in measurement 141 of the analyzed measurement cycle.

nicely that faster protons are deflected less by the lower ExB than slower ones. To see how many protons have correlated electrons reaching the de-

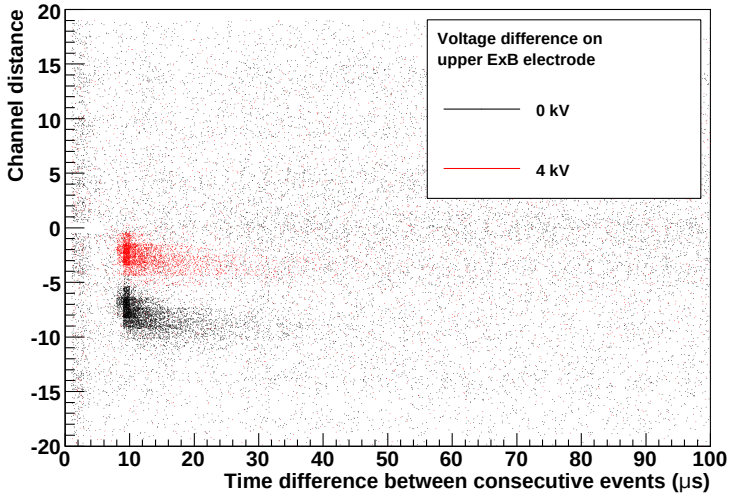

Figure 5.35: The position of the correlation peak for voltage differences on the upper ExB electrode of 0 kV and 4 kV.

tector, we can add the number of events in the correlation peak for $j = 1$ and $j = 2$ and compare those to the number of protons we get for the same measurement by analyzing all channels and extracting the protons by method two. The number of protons is $N_{\mathrm{p}} = 23724 \pm 155$, the number of correlated events is $N_{\mathrm{corr}} = 3717 \pm 61$. However, the latter includes chance correlations[18] as well, which have to be taken into account. Assuming a fraction of about 21% chance correlations (see next section), N_{corr} becomes 2936 ± 48. This results in a fraction of $12.4 \pm 0.2\%$ correlated events, which agrees very well with the estimated amount.

April, but on the 22. of February. The exact value of the voltage on the lower ExB electrode for this day is unfortunately not documented, but from the observed shift, it would have been several hundred V, which was the value that was noted in the lab book on the day before.

[18] I.e. pairs of events which do not correspond to an electron-proton pair from the same neutron decay.

5.5.2 Pulseheight spectra of correlated events

The pulseheight spectra of the events which make up the correlation peak are interesting since they contain information about both the proton and electron spectra. While the former is already well known from the measurements at low analyzing plane voltages, looking at the correlated events is the best way to get a clean[19] electron spectrum and to get an idea about how much the electron background makes up of the total background.

To obtain these spectra, a pulseheight analysis[20] is done for all events i[21] and $i+1$ in the correlation peak, which was defined to be in the time-channeldifference interval[22] [6μs, 40μs, 0, 5]. To obtain good statistics, this analysis was performed for all measurements at analyzing plane voltage 50 V. The results are shown in Fig. 5.36 and Fig. 5.37.

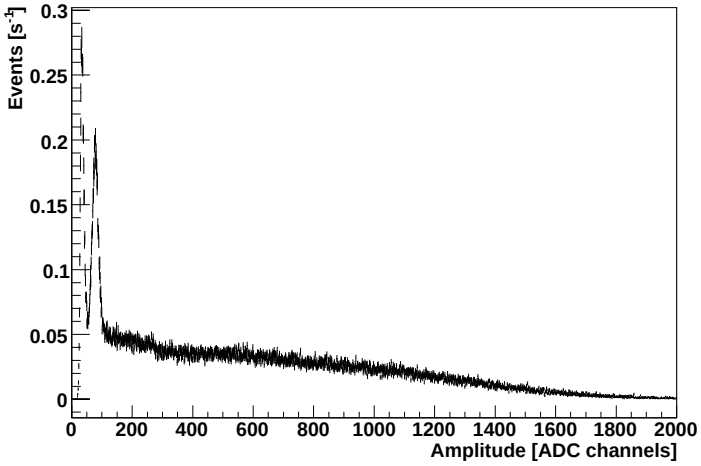

Figure 5.36: The pulseheight spectrum of events i in the correlation peak.

[19] I.e. a spectrum where other background is strongly suppressed.
[20] Due to programming reasons, it was done with averaged baselines, but without fitting of the single events.
[21] Which will be referred to also as *triggers*.
[22] Given in the form [minimum time difference, maximum time difference, minimum channel difference, maximum channel difference].

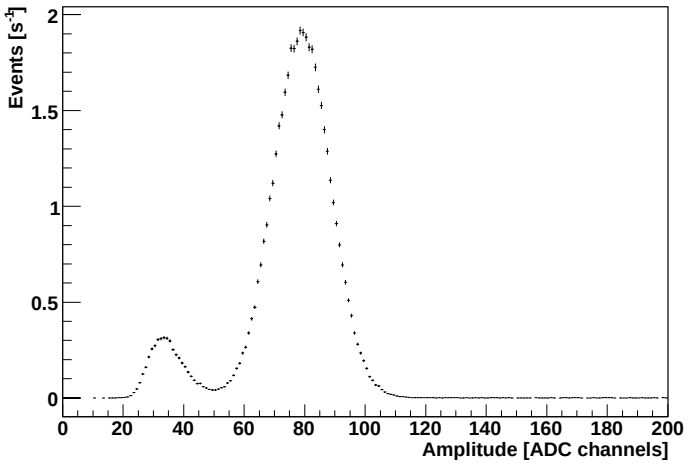

Figure 5.37: The pulseheight spectrum of events $i+1$ in the correlation peak.

There are a few noteworthy features of these spectra. In the spectrum for events $i+1$, there is still some noise in addition to the proton peak (which is very well developed). This noise stems from the chance correlations, which were mentioned above. The same is the reason for the peak at 30 keV in the spectrum of the events i. Doing the same pulseheight analysis for a "control" area defined as the area [6μs, 40μs, -5, 0], in which no proton-electron pairs can be found, one obtains the spectrum shown in Fig. 5.38. The peak at 30 keV is also present and is of the same size as in Fig. 5.36.

A quantitative analysis shows that the 30 keV peak in the correlated trigger spectrum contains 4.82±0.47 events s^{-1}, and the peak in the control spectrum contains 4.02±31 events s^{-1}. Both these values were obtained by fitting the spectra with function 5.7, so the very small difference between them can be explained by the fact that the contribution from the electrons in the correlated spectrum isn't taken fully into account.

The amount of events in the control area also lets us determine how big the fraction of events in the correlation peak is that can be attributed to chance correlations. It is given simply by the ratio of events in the control area to events in the area of the correlation peak, which is $\frac{51726}{245426} \approx 21\%$.

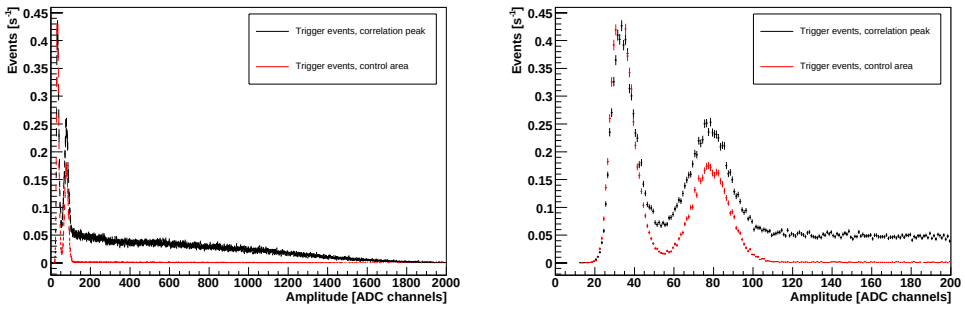

Figure 5.38: The pulseheight spectrum of trigger events in the correlation peak (black) and the control area (red). See text for details about the control area. The right picture is a blow-up of the area of the 30 keV peak.

If one subtracts the red from the black curve in Fig. 5.38, one obtains the spectrum shown in Fig. 5.39. There are some obvious differences to the theoretical electron spectrum shown in the top of Fig. 2.4. The source for these discrepancies is the fact that due to the thinness of the detector, higher energetic electrons do not deposit all of their energy in the detector, but may have substantial energy left when exiting the detector again. The backscattering fraction for electrons is also much higher than for heavier particles, as noted before, which further distorts the spectrum due to partial energy deposition of a backscattered electron. For comparison, a the energy deposition of electrons from neutron decay in a 0.3 mm thick silicon slab as it was obtained in the simulations done with PENELOPE is shown in Fig. 5.40[23]. Qualitatively, the shape of the measured spectrum, especially at higher energies matches the simulated one fairly well. Quantitatively, there seem to be some discrepancies; in particular, the measured spectrum seems to be shifted to lower energies and we do not see the rather prominent peak at about 100 keV. However, this might be explained by the very simple model of the detector in the simulation as well as the fact that the simulation does not include any magnetic or electric fields, which are present in the experiment. Simulations with different angles of incidence showed that the low-energy part of the simulated energy spectrum in particular is very sensitive to changes of that parameter.

[23]The upper limit of 2000 ADC channels in Fig. 5.39 corresponds to about 600 keV.

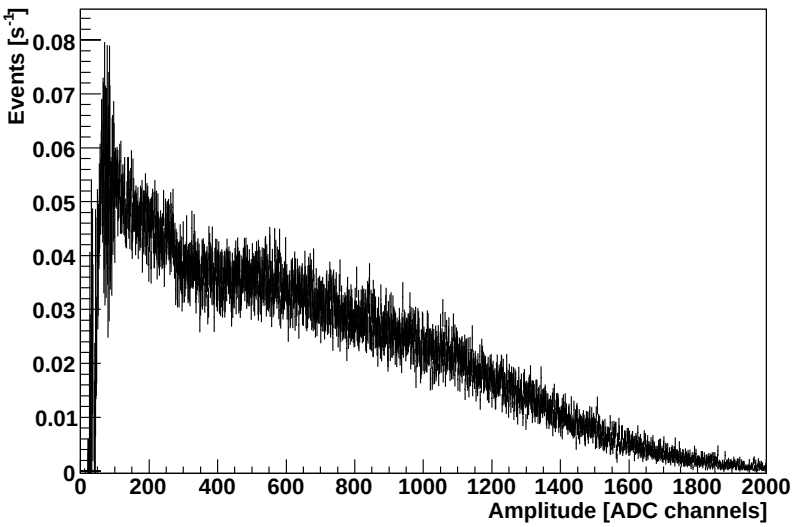

Figure 5.39: The electron pulseheight spectrum obtained by subtracting the red from the black curve in Fig. 5.38.

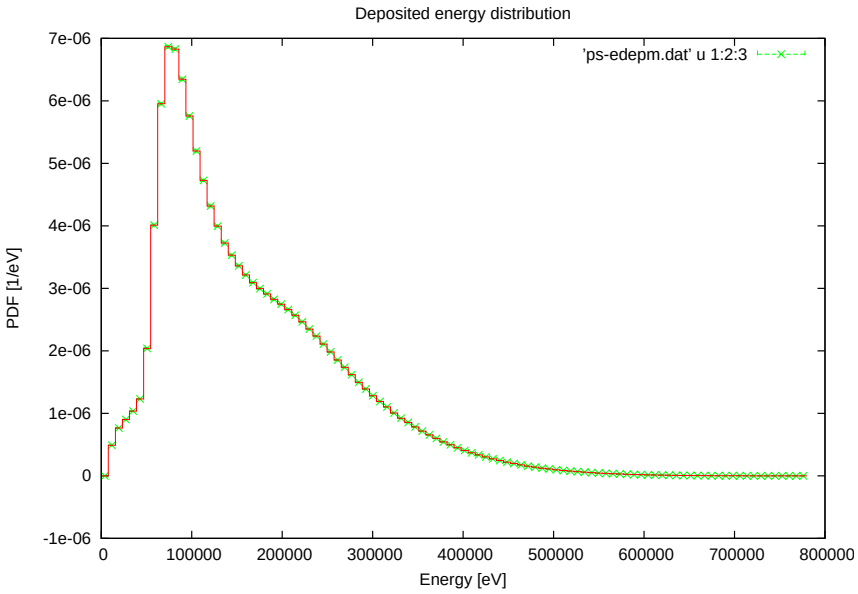

Figure 5.40: The simulated energy deposition of electrons from neutron decay in a 0.3 mm thick silicon slab.

5.5.3 The background peak

The other prominent feature of the background spectrum is the additional peak that appears slightly below the proton peak. Its source is unkown. A likely explanation for it would be that it is caused by ionized particles which are generated and trapped between the upper ExB drift electrode and the detector. These particles would be lower-energetic than the protons, since they would be created already on a positive potential, which would explain why the peak is centered at lower channel numbers than the proton peak.

Since we do not have any exact information on the vacuum near the detector and the upper ExB electrode (the upper vacuum sensor had to be dismantled for measurements, since it contains highly magnetic materials), it is possible that ions could be generated in this area, for example by interaction with decay electrons, which would then be accelerated towards the detector and generate a signal.

It is also possible that particles could become trapped in that region due to the electric and magnetic field configurations there. Since the peak remained constant over the analyzed measurement cycle, studies of different cycles have to be performed to understand it better. This is currently being investigated by our colleagues in Mainz.

6 Summary and conclusion

In the four beam times we performed at the FRM-II, we were able to show that the spectrometer works in principle and that a determination of a with it is possible.

A set of routines has been written for decoding and analyzing the raw data. Due to the fact that we have the full information for each event, a very flexible and detailed analysis is possible. The routines are written in C using the ROOT libraries and can be easily adapted or expanded. After testing several different methods, we have found a reliable way to extract the proton count rates from the data by building pulseheight spectra for each measurement, subtracting background measurements from those and fitting the resulting peak with a Gaussian. This removes the need to find special integration limits (to be sure that there is no overlap with electronic noise), since the area under the Gaussian is included as a fit parameter.

The background of the measurements was studied in detail. A very prominent feature is a peak that is situated slightly below the proton peak, whose source is not fully understood yet. Its shape and position suggest that it is generated by positively charged particles. This peak does not change significantly during one measurement cycle, but preliminary analysis of other cycles by our colleagues in Mainz shows that it can vary greatly between cycles and might be connected to HV breakthroughs at the upper ExB electrode [MH07].

The background caused by electrons from neutron decay is very well understood and conforms quantitatively to our expectation. Due to the spatial resolution of our detector and the time resolution provided by our DAQ electronics, we were able to study correlated electron-proton pairs from one neutron decay event. They form a clearly visible peak in a time- and channel-distance spectrum, which can be shifted in the channel-dimension by varying the voltages applied to the lower and upper ExB electrodes. This is due to the fact that the protons will be deflected more strongly than the electrons because of their different velocity. Performing a pulse-

height analysis for both involved particles allowed us to obtain a fairly clean energy spectrum of the background caused by electrons from neutron decay in our detector. Using these correlations for data analysis may be of interest for future neutron decay experiments which use segmented detectors, such as abBA [Wil05].

There are various systematic effects which have not been discussed in this work because they are only accessible by looking at the data of several different measurement cycles, e.g. the dependence of the proton spectrum on different ExB voltage settings or different trigger settings. These effects are currently being analyzed by our colleagues in Mainz; preliminary results including several different measurement cycles show that the extracted values of a vary drastically between different cycles. One characterstic effect seems to be that the strength of the background peak varies from cycle to cycle, and the fluctuations in a are connected to this [MH07]. For this reason, it does not make sense to give a quantitative value for a in the framework of this thesis.

Outlook

The main problem we encountered concerning the detector was the noise performance, which was about a factor of two worse than expected, leading to a significant overlap of the proton peak and the noise peak. This in turn required a very time-consuming analysis to extract the protons.

For this reason, the detector setup will be changed for future measurements. The detector is being replaced by a Silicon-Drift-Diode (SDD) manufactured by the Halbleiterlabor (HLL) of the Max-Planck-Institute. One of the most important features of this detector is that the first field effect transistor (FET) is located on the backside of the diode itself, resulting in a very stable signal that is much less susceptible to noise.

First measurements done with the detector indicate that we will be able to detect 15 keV protons with a clear separation from the noise [Sim07b]. Pulseheight spectra recorded with the detector at the proton source PAFF can be seen in Fig. 6.1.

Since we'll be able to use a much lower high voltage, this will eliminate the second problem we had during the beam times at the FRM-II, the high voltage breakthroughs. Stability problems began at high voltage values of about 25 keV, below which we'll be able to stay. This in turn eliminates

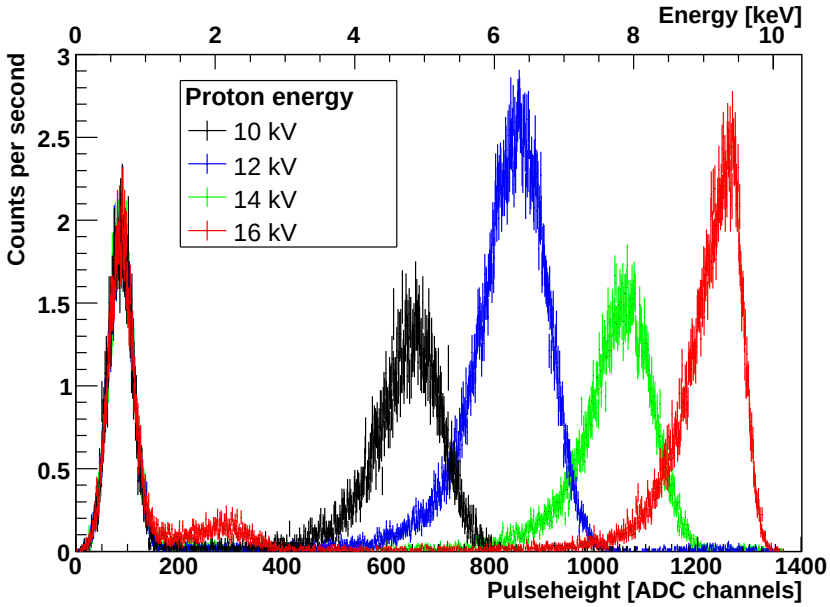

Figure 6.1: Pulseheight spectra recorded with the SDD detector provided by the HLL.

the need for a movable detector mechanics, allowing a more rigid setup in its place.

Another advantage will be that it might be possible to actually resolve the background peak separately from the proton peak; this might make a complete fit of the spectrum possible, and allow a more detailed study of the origin of that peak.

List of Tables

List of Figures

Bibliography

[Abe00] H. Abele. The Standard Model and the neutron β-Decay. *Nuclear Instruments and Methods in Physics Research Section A: Accelerators, Spectrometers, Detectors and Associated Equipment*, 440(3), 499–510, February 2000. 12

[Abe02] H. Abele, M. Astruc Hoffmann, S. Baessler, et al. Is the Unitarity of the Quark-Mixing CKM Matrix Violated in Neutron β-Decay? *Phys. Rev. Lett.*, 88(21), 211801, May 2002. 3

[AG05] F. Ayala Guardia. *First tests of the neutron decay spectrometer aSPECT*. Master's thesis, Johannes Gutenberg Universität Mainz, 2005. 28, 29, 30, 33, 64, 117

[Bau03] G. Baum, R. Birsa, F. Bradamante, et al. The COMPASS RICH-1 read-out system. *Nuclear Instruments and Methods in Physics Research Section A: Accelerators, Spectrometers, Detectors and Associated Equipment*, 502(1), 246–250, April 2003. 49

[Byr94] J. Byrne. *Neutrons, Nuclei and Matter*. IOPP, Bristol, 1994. 13

[Cab63] N. Cabibbo. Unitary Symmetry and Leptonic Decays. *Phys. Rev. Lett.*, 10(12), 531–533, Jun 1963. 17

[dee] Detection Technologies, products. Website. URL http://www.deetee.com/ion_radiation.htm. 42

[Dob75] R. Dobrozemsky, E. Kerschbaum, G. Moraw, et al. Electron-neutrino angular correlation coefficient a measured from free-neutron decay. *Phys. Rev. D*, 11(3), 510–512, February 1975. 14

[Fer34] E. Fermi. Versuch einer Theorie der β-Strahlen. *Zeitschrift für Physik*, 88, 161–177, 1934. 8

[Gam36] G. Gamow and E. Teller. Selection Rules for the β-Disintegration. *Phys. Rev.*, 49(12), 895–899, Jun 1936. 9

[Glü93] F. Glück. Measurable distributions of unpolarized neutron decay. *Phys. Rev. D*, 47(7), 2840–2848, Apr 1993. 23

[Glü95] F. Glück, I. Joó, and J. Last. Measurable parameters of neutron decay. *Nuclear Physics A*, 593(2), 125–150, Oct 1995. 10, 11, 12, 13

[Glü05] F. Glück, S. Baessler, J. Byrne, et al. The neutron decay retardation spectrometer aSPECT: Electromagnetic design and systematic effects. *Eur. Phys. J. A*, 23(1), 135–146, 2005. 25

[GM64] M. Gell-Mann. A schematic model of baryons and mesons. *Physics Letters*, 8(3), 214–215, 1964. 17

[Gro89] K. Grotz and H. V. Klapdor. *Die schwache Wechselwirkung in Kern-, Teilchen- und Astrophysik*. B.G. Teubner, 1. edition, 1989. 7

[Gru06] B. Grube. *A Trigger Control System for COMPASS and a Measurement of the Transverse Polarization of* Λ *and* Ξ *Hyperons from Quasi-Real Photo-Production*. Ph.D. thesis, Technische Univesität München, 2006. URL https://www.e18.physik.tu-muenchen.de/publications/thesis/phd_bgrube.pdf. 53

[Hab97] C. Habeck. *doctoral thesis*. Ph.D. thesis, Univsersity of Sussex, 1997. 21

[Jac57] J. D. Jackson, S. B. Treiman, and H. W. Wyld. Possible Tests of Time Reversal Invariance in Beta Decay. *Phys. Rev.*, 106(3), 517–521, May 1957. 11

[Jac62] J. Jackson. *Classical Electrodynamics*. Wiley, 1962. 27, 31

[Juo02] S. Juottonen. E-Mail communication, 2002. 42, 43, 118

[Kno99] G. F. Knoll. *Radiation Detection and Measurement*. Wiley, New York, third edition, 1999. 39, 40, 76

[Kob73] M. Kobayashi and T. Maskawa. *CP*-Violation in the Renormalizable Theory of Weak Interaction. *Progr. Theor. Phys.*, 49(2), 652–657, 1973. 17

[Lee56] T. D. Lee and C. N. Yang. Question of Parity Conservation in Weak Interactions. *Phys. Rev.*, 104(1), 254–258, Oct 1956. 10

[Lut99] G. Lutz. *Semiconductor Radiation Detectors*. Springer, Berlin, Heidelberg, New York, first edition, 1999. 39

[Man06] A. Mann, B. Grube, I. Konorov, et al. A Sampling ADC Data Acquisition System for Positron Emission Tomography. *IEEE Transactions on Nuclear Science*, 53(1), 297–303, February 2006. 50

[MH07] R. Munoz-Horta and S. Baessler. Private Communication, 2007. 111, 112

[Mül07] A. R. Müller, F. J. Hartmann, S. Paul, et al. PAFF, a low-energy, low-flux proton accelerator for detector tests. Preprint submitted to NIM-A, June 2007. 46

[Nac68] O. Nachtmann. Relativistic corrections to the recoil spectrum in neutron β-decay. *Zeitschrift für Physik*, 215(5), 505–514, 1968. 3, 21

[Pov99] B. Povh, K. Rith, C. Scholz, et al. *Teilchen und Kerne*. Springer, 5. edition, 1999. 16, 21

[roo07] ROOT - An Object Oriented Data Analysis Framework. Software package, 2007. URL http://root.cern.ch. 48

[Sal06] F. Salvat, J. M. Fernandez-Varea, E. Acosta, et al. PENELOPE - A Code System for Monte Carlo Simulation of Electron and Photon Transport. Computer Program, 2006. URL http://www.nea.fr/abs/html/nea-1525.html. 102

[Ser05] A. Serebrov, V. Varlamov, A. Kharitonov, et al. Measurement of the neutron lifetime using a gravitational trap and a low-temperature Fomblin coating. *Physics Letters B*, 605(1), 72–78, 2005. 16

[Sim06] M. Simson. *First measurements with the new neutron decay spectrometer aSPECT at the Munich Research Reactor*. Master's thesis, Technische Univesität München, 2006. 28, 46, 48, 63, 117

[Sim07a] M. Simson. Private Communication, 2007. 48, 99, 101

[Sim07b] M. Simson, P. Holl, A. R. Müller, et al. Detection of low-energy protons using a silicon drift detector. Preprint submitted to NIM-A, 2007. 112

[Str78] C. Stratowa, R. Dobrozemsky, and P. Weinzierl. Ratio $|\frac{g_A}{g_V}|$ derived from the proton spectrum in free-neutron decay. *Phys. Rev. D*, 18(11), 3970 – 3979, Dec 1978. 14

[Wie05] F. Wietfeldt, B. Fisher, C. Trull, et al. A method for an improved measurement of the electron-antineutrino correlation in free neutron beta decay. *Nuclear Instruments and Methods in Physics Research Section A: Accelerators, Spectrometers, Detectors and Associated Equipment*, 545(1-2), 181–193, June 2005. 14

[Wil05] W. Wilburn, J. Bowmann, G. Michell, et al. Measurement of Neutron Decay Parameters - The abBA experiment. *J. Res. Natl. Inst. Stand. Technol.*, 110(4), 389–393, July-August 2005. 112

[Wu57] C. S. Wu, E. Ambler, R. W. Hayward, et al. Experimental Test of Parity Conservation in Beta Decay. *Phys. Rev.*, 105(4), 1413–1415, Feb 1957. 14

[Yao06] W.-M. Yao, C. Amsler, D. Asner, et al. Review of Particle Physics. *Journal of Physics G*, 33, 1+, 2006. URL http://pdg.lbl.gov. 12, 15, 16, 18, 19, 20

[Zie07] J. F. Ziegler. SRIM - The Stopping and Range of Ions in Matter. Computer Program, 2007. URL http://www.srim.org. 46, 99

[Zim00] O. Zimmer, J. Byrne, M. G. D. van der Grinten, et al. "*a*spect" - a new spectrometer for the measurement of the angular

correlation coefficient a in neutron beta decay. *Nuclear Instruments and Methods in Physics Research Section A: Accelerators, Spectrometers, Detectors and Associated Equipment*, 440(3), 548–556, February 2000. 3, 25

Acknowledgements

I would like to thank the following people:

Prof. Dr. Oliver Zimmer for giving me the opportunity to work on *a*SPECT, his guidance and his support.

Dr. Hans-Friedrich Wirth for his invaluable advice and his pragmatism.

Martin Simson for characterizing the *a*SPECT detector, his hard work before, during and after our beam times and the flawless maintenance of the coffee machine.

Dr. Stefan Baessler for the many helpful pointers.

Michael Borg, **Raquel Muñoz**, **Fidel Ayala** and **Gertrud Konrad** for the shared fun, frustrations and successes while running *a*SPECT.

Axel Reimer Müller for setting up PAFF and many, many interesting and entertaining conversations. Also him and **Rüdiger Picker** for being great room mates.

Heinz Angerer, **Igor Konorov** and **Alexander Mann** for the design of the electronics and never losing patience when they had to repair it (again).

Sergei Mironov for his help constructing the detector mechanics.

Boris Grube, **Roland Kuhn** and **Dr. Jan Friedrich** for valuable help with ROOT and C++.

Martin Aigner and the rest of the people in the workshop for always being helpful when things were needed on short notice.

All members of E18 and especially **Karin Frank** for the friendly and familiar atmosphere which hallmarks the chair.

Åsa, **Hakan** and **Åke** for proofreading and catching many small errors that would have gone unnoticed otherwise.

My mother for supporting me throughout my life.

Nicole for her patience, support and encouragement. This thesis is dedicated to her.